AGGREGATE BREAKAGE IN LAMINAR COUETTE FLOW

by

Gustavo Andrés Cifuentes Díaz

A thesis submitted in partial fulfillment of the requirements for the degree of

Master of Science

In
Chemical Engineering

Department of Chemical and Materials Engineering
University of Alberta

Abstract

Micron-size particle suspensions are very common in industrial processes such as mineral extraction and wastewater treatment. These particles are difficult to separate from the fluid media due to their size. The formation of aggregates increases the effective size of these particles, increasing the settling velocity of the particles and facilitating separation. Control of the aggregate characteristics, such as size, and structure, influences the efficiency of these industrial processes. This study investigates the effect of shear on the breakage of aggregates. For this purpose, an experimental setup was designed where aggregates were formed and then broken in a Couette cell with a rotating inner cylinder and a transparent outer cylinder, which permits monitoring the aggregates using in situ image analysis.

The experiments were carried out with 2 μm sulfate latex microspheres in a neutrally buoyant fluid-particle system. The aggregates were grown at a constant shear rate of 17.6 s^{-1} until they reached their steady-state size. Then, breakage was induced by increasing the rotational velocity of the inner cylinder. Different breakage shear rates within the range of 28.9 s^{-1} and 86.8 s^{-1} were tested, which were in the laminar Couette flow regime.

Two different behaviours were observed for the range of shear rate studied. One range of shear rate produced re-aggregation of the fragments; in the other, only breakage takes place. It was observed that by increasing the breakup shear rate, the aggregate size was proportional to γ^{-p} with $p = 0.69$ for all the experiments, and $p = 0.48$ for the region where only breakage takes place. These results are in agreement with previous studies. Measurements of perimeter fractal dimension indicated that aggregate breakup is accompanied by restructuring. The aggregate sizes obtained in the experiments where only breakage was observed were used to estimate the aggregate cohesive

force holding the aggregates together, which was found to be 1.94 ±0.11 nN and independent of the aggregate size. This value is in good agreement with the aggregate strength reported in the literature. The value of the aggregate cohesive force obtained in the present study is similar to the theoretical interaction force between two particles, suggesting that, for this system, the aggregate cohesive force is dictated by the attractive force between two primary particles, i.e., between the 2μm latex microspheres. This result suggests that the force required to break the aggregate is related to the force required to break a single chain of particles within the aggregate. More studies of the cohesive force of aggregates of different primary particles sizes and different aggregation mechanisms are needed.

Acknowledgments

First and foremost, I would like to express my deepest gratitude to my supervisor Dr. Sean Sanders for allowing me to be a part of the Pipeline Transport Processes Research Group. His generous support and guidance during this project were invaluable. Dr. Sanders always inspired me to think more critically, for which I am very thankful.

I am very grateful to Dr. Marcio Bezerra Machado for his continuous advising, for his endless support and feedback. I am also thankful to Ms. Terry Runyon for her administrative support during these years.

I would like to thank the Natural Sciences and Engineering Research Council of Canada (NSERC) support for the Pipeline Transport Processes laboratory.

I would like to thank my colleagues in the Pipeline Transport Processes research group members whom I had the pleasure of working with: Dr. Akash Saxena and Ricardo Andrade Rossi. Also, I want to thank my friends in the Pipeline Transport Process (PTP) Research Group, Aakanksha Bhargava, Omnath Ekambaram, Sahil Sood, Saeid Dehghani, with whom I spent pleasant moments during these years.

I would also like to thank my family. I thank my mother, Doris Díaz, for her unconditional love. This journey would not have been possible without the encouragement of my mother. Also, I thank my partner Laura Manchola-Rojas for being the best company I could have. Her love and support made my life during these hard years much easier.

Table of Contents

List of Figures

List of Tables

List of Symbols

Roman

Symbol	Description	Units
a	Radius of a sphere	m
A	Projected area of the aggregate	μm^2
A_{11}	Hamaker constant	J
C	Aggregate strength coefficient	--
d	Equivalent circle area-based diameter	m
d_{10}	Arithmetic or number mean diameter	µm
d_{32}	Sauter mean diameter	µm
$d10$	Diameter for the 10% number percentile	µm
$d50$	Diameter for the 50% number percentile	µm
$d90$	Diameter for the 90% number percentile	µm
d_{agg}	Aggregate diameter	m
d_f	Mass fractal dimension	--
d_{gap}	Length of Couette cell gap	m
d_p	Primary particle diameter	m
d_{pf}	Perimeter fractal dimension	--
F	Force	N
H	Distance	m
L	Size	m
M	Mass	Kg
n_o	Bulk electrolyte concentration	M
p	Aggregate size exponent	--
Pe	Peclet Number	--
R	Radius	m
R_1	Radii of the inner cylinder	m
R_2	Radii of the outer cylinder	m
T	Temperature	K

Symbol	Description	Units
Ta	Taylor Number	--
V	Interaction energy	J
z	Valency of the electrolyte	--

Greek

Symbol	Description	Units
ε	Electric permittivity of the medium	$C^2\ J^{-1}\ m^{-1}$
γ	Shear rate	s^{-1}
κ	The inverse of the Debye length	m^{-1}
μ	Dynamic Viscosity	Pa s
ρ	Density	$Kg\ m^{-3}$
σ	Shear Stress	Pa
σ_d	Standard deviation of the diameter	μm
ω	Angular velocity	$Rad\ s^{-1}$
ψ	Surface potential	V

Constants

Symbol	Description
e	Elementary charge = 1.602×10^{-19} C
k_b	Boltzmann constant = 1.381×10^{-23} J K^{-1}
N_a	Avogadro number = 6.022×10^{-23} mol^{-1}
ε_o	Electric permittivity of free space = 8.854×10^{-12} $C^2\ J^{-1}\ m^{-1}$

Chapter 1 Introduction

1.1 Background

In many industrial operations, particles are removed from suspensions through methods such as filtration, settling, and flotation. Gravity settling is the most common technique for the separation of particles from a fluid. The physical characteristics of the fluid and particles play a significant role in the efficiency of a gravity separation process. For example, particles with higher density and larger size have a higher settling velocity; thus, the separation via settling is easier to achieve with larger and denser particles and in systems where the difference between the particle and fluid density is greater. Fine particles, in contrast, are difficult to separate as they remain dispersed in the fluid. These fine particles are usually in the colloidal size range, which is between 1 nm and 1μm [1]. Colloidal particles exhibit short-range interactions, such as the attractive van der Waals and the repulsive electric double-layer forces [2]. When the attractive forces are stronger than the repulsive ones, the particles agglomerate to produce a larger structure of particles known as aggregates; this process is known as aggregation (also referred as flocculation or coagulation). With the increase in effective particle size, the particles settle more readily, making the separation of the fine particles from the fluid possible.

To produce aggregates, the particles need to be carried to the proximity of other particles and collide to be subjected to the short-range attractive van der Waals forces. This is achieved in industrial operations through fluid motion, which exerts hydrodynamic forces on the particles and aggregates. An increase in the hydrodynamic forces can affect the aggregate; the particles comprising the aggregate can reorganize and are kept together in a way such that the internal cohesive forces withstand the hydrodynamic forces, and the breakage does not occur, as is shown

in Figure 1-1 a. In the case where the hydrodynamic forces are too strong, the aggregate cannot withstand the hydrodynamic forces even with restructuring and the aggregate will break (Figure 1-1 b).

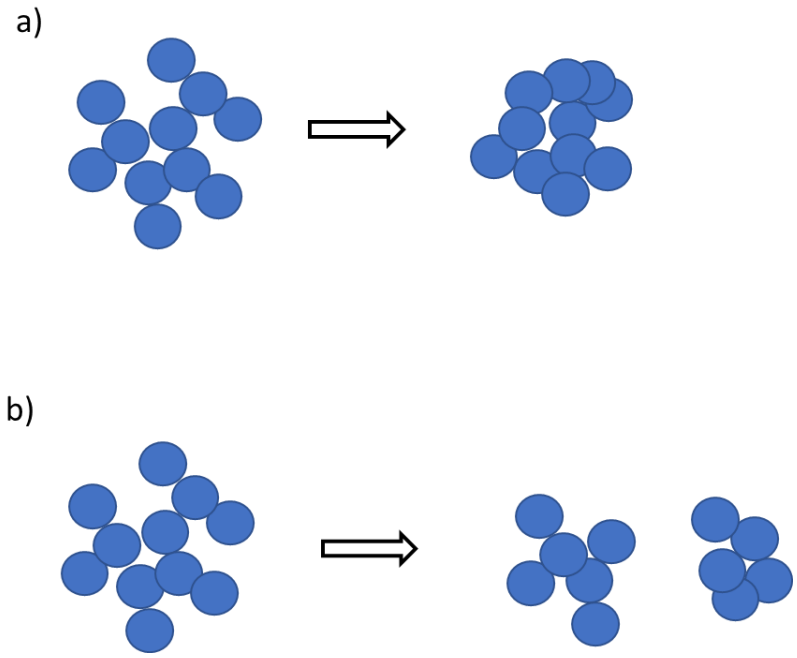

Figure 1-1 Schematic of the process of restructuring (a) and breakage (b).

Many industrial processes involve aggregation, breakage, and restructuring. Controlling the aggregate properties such as size and structure is important in managing the efficiency of the process. Some industrial applications are discussed below.

Oil sands tailings:

The oil sands extraction process produces large volumes of waste material with a high solid content (sand, silt, and clay) and residual bitumen [3]. This waste stream is known as tailings. The sand in the tailings is easily separated, while fine particles (silt and clay with size < 44 μm [4]) can remain suspended in the tailings for decades [4]. Two problems arise as a result of the slow

separation of solids: first, tailings must be stored in massive ponds or dams, which are environmentally problematic [5]. Second, the water recycled from these ponds cools down and needs to be reheated before it can be used in the extraction process [6–8].

To allow the settling of the fine solids, a successful strategy is to increase the effective particle size through aggregation. The formation of aggregates starts by mixing the fluid tailings with charge neutralizing coagulants and polymer flocculants. This process can be carried out in a thickener. The thickener provides the hydrodynamic conditions that allow the particles to aggregate and settle, separating the fine solids from the water. The overflow is composed of hot water that is recycled to the extraction process. The underflow forms a concentrated slurry, composed of the flocculated solids [4,8]. The thickened tailings are then transported through pipelines to a deposition area. During the transportation, the flocculated tailings are sheared, causing the restructuring and breakup of the aggregates [9], which decreases the efficiency of the thickening process.

Civic water treatment:

Natural organic matter (NOM) is a complex mixture of organic substances present in surface and ground waters [10]. The common components of NOM are zooplankton, phytoplankton, bacteria, humic acids, and clay-humic acid complexes [11], which result from the degradation of organic life. Organic matter is not necessarily toxic, but it can be a carrier for toxic substances like pesticides [12]. The humic substances (a NOM component) are high colour materials, and need to be removed because they alter water properties such as taste, odour, and colour. The pre-treatment of drinking water includes the separation of the suspended impurities via aggregation [10], which is carried out by the addition of metallic salts and polyelectrolyte flocculants.

The selection and dosage of the polymer are important and must be tailored according to the composition and quantity of the impurities, which depends on the water sources and season of the year [10]. In addition, the mixing conditions affect the formation of flocs [10,11], and the overall efficiency of the flocculation process.

Solvent deasphalting.

Bitumen froth is an intermediate material produced during the oil sand processing, which contains about 60% bitumen, 30% water and 10% solids (by mass) [13]. The bitumen contains asphaltenes, which are defined as the fraction of the crude oil that is not soluble in single chain alkanes (e.g., pentane or heptane) but is soluble in toluene [4]. Before upgrading the bitumen, the water and the suspended solids must be removed.

In the paraffinic froth treatment process, the bitumen froth is mixed with a paraffinic solvent. The addition of solvent reduces the viscosity of the oil phase and to induces a density difference between the water and oil phases, consequently enhancing the separation. The addition of solvent also results in the formation of aggregates comprised of water droplets, solids and asphaltenes [14]. Asphaltene aggregates are separated using conventional settlers [4]. The settling velocity inside the settler is influenced by the size and structure of the aggregates [14]. It is known that the mixing condition affects the composition and the settling velocity of the aggregates [13]. Therefore, the efficiency of the settlers could be optimized by changing the mixing conditions.

1.2 Problem statement

The aggregate characteristics, such as size and structure, dictate the efficiency of separation processes such as settling or centrifugation. Therefore, it is beneficial to control the characteristics

of aggregates before the suspensions reach these process units. In the process units or during transport the aggregates can experience a higher shear that can change their size. The change in aggregate size under variable shear conditions is related to the strength of the aggregate [15–18]. When an aggregate is in a flow field, its size is dictated by the interplay of the aggregate internal forces and the hydrodynamic forces acting on it [19]. The aggregate breaks when the hydrodynamic forces overcome the internal cohesive forces. In other words, the change in aggregate size depends on its ability to resist external forces.

Many studies have tried to capture the phenomenon of aggregate breakage and restructuring. Different flow conditions have been used to experimentally investigate the breakage, e.g., turbulent flow [19–24] and extensional flow [16,25–28]. Because of the different local shear rates, it is difficult to quantify the shear rate acting on the aggregate. Therefore, it is necessary to use approximations to assess the hydrodynamics forces acting on the aggregate. For this reason, laminar flow is more appropriate for studying aggregate breakage since its velocity field can be characterized easily.

To the author's knowledge, very few researchers have studied aggregate breakage in the laminar regime [29,30], and even then, most of the breakage experiments are performed at high shear conditions (shear rate > 100 s^{-1}). Information about aggregate breakage at low shear rates is scarce. This information is valuable since it can be used in the design of equipment that operates under low shear conditions, e.g., gravity settlers.

Numerical modelling is also commonly used to evaluate the evolution of the aggregate size and structure under different shear conditions [25,31]. Numerical modelling is confined to very low Reynolds numbers due to the high computational cost and limited numerical methods [31]. There is also a scarcity of comparison of these numerical models with experimental data as the

majority of experiments were performed at higher Reynold numbers. Furthermore, there is a lack of appropriate experimental data that accurately characterizes the hydrodynamics acting on the aggregates which makes the comparisons more difficult.

1.3 Research Objectives

This project aims to study the effect of hydrodynamics on aggregate breakage in laminar shear flow. The main objectives of this study are:

- To experimentally investigate the effect of shear rate on size and structure of aggregates after breakage.
- To calculate the cohesive strength of aggregates.

To fulfill these objectives, the principal activities of this research project are:

- To design a lab-scale shearing device capable of applying shear in laminar conditions, in which the aggregates can be exposed to a controlled specific shear rate.
- To develop a method to obtain the size and structure of the aggregates without affecting the aggregate, i.e., as in situ image analysis instead of collecting samples and conducting off-line analysis.

1.4 Thesis outline

This thesis comprises five chapters. This chapter presents the background and motivation for the project. The literature review (Chapter 2) summarizes the previous research in this field and

identifies some of the knowledge gaps that this study aims to close. The third chapter provides the experimental method. A detailed explanation of the materials, equipment, and procedures used in this research is presented. The algorithm used for image analysis is described. Chapter 4 contains the results and discussion of this study. The size and structure of aggregates at different shear conditions are discussed. The evolution of the size after the aggregates are exposed to shear is discussed. The aggregate cohesive force is quantified using the experimental data collected during this study. Chapter 5 provides the summary of key findings, conclusions and recommendations for future research based on the analysis performed during this project.

1.5 Significance of Contributions

In this project, the breakage and restructuring of aggregates in laminar flow at low shear rates is investigated. The contributions of this thesis can be summarized as follows:

- The relation between the aggregate size and the shear rate after breakage provides information regarding the aggregate cohesive force. This information is quite valuable as it allows for the improvement in equipment design to reduce aggregate breakup.
- The experimental data obtained under controlled conditions is valuable for comparison with results from simulations, as the breakage and restructuring of aggregates are mostly studied through computational models.
- The experimental setup designed in this thesis can be used to study the behaviours of aggregates formed using different particles and flocculants.
- The script developed for image analysis can be used to study similar systems in the future.

- The findings obtained in this research project can contribute to the understanding of aggregate formation and breakage in any fluid-particle system where aggregates are present in similar flow conditions.

1.6 Authors' contributions

In this study, the equipment and the materials were provided by Dr. Sean Sanders' Pipeline Transport Processes Research Group. The design of the concentric cylinder was made by the author, approved by Dr. Sean Sanders and the engineering machine shop of the University of Alberta was in charge of its construction.

The idea of this project came from Dr. Sean Sanders. The specific concepts covered in this thesis were developed by the author under the guidance of Dr. Sean Sanders. The method and the safe work procedures were developed by the author. The author performed all experiments and measurements in this thesis. The Python code for image analysis was written by the author. Dr. Sean Sanders, Dr. Marcio Machado and Dr. Akash Saxena contributed to the review of the results and this thesis.

Chapter 2 Literature Review

2.1 Introduction

This chapter reviews the relevant literature regarding particle aggregation and the experimental approaches used to investigate the behaviour of aggregates in fluid flow. The scientific literature on aggregation is extensive because aggregation is a critical process in many industries. Separation processes, such as sedimentation and filtration, are more effective when fine particles are first induced to form aggregates [32,33]. Such particles typically fall within the colloidal size range, which is often taken to be between 1 nm to 1 μm [1], and so they are subject to Brownian motion: a random particle movement caused by the fluid thermal energy. This motion along with the interparticle surface forces, dominates over the gravity force and this movement prevents them from settling [1]. A colloidal system is stable if it does not aggregate or settle over time or unstable if it aggregates over the time scale of interest.

The first step in the aggregation process is the destabilization of the fine particles. This can be achieved by the addition of chemicals, seeking to minimize interparticle repulsion due to surface electrical charges [34]. Once the colloidal system is unstable, the particles need to be transported into close proximity with other particles to collide where short-range attractive forces cause aggregates to form. The two primary transport mechanisms are Brownian motion and fluid motion [1].

Perikinetic aggregation is caused by Brownian motion [35], and it is typically a slow process. The aggregation rate can be increased by adding another transport mechanism, for instance, by mixing the suspension. When collisions between primary particles are caused by fluid flow, the mechanism is called orthokinetic aggregation, which increases the number of collisions, reducing

the time required for the aggregation process [1]. The dominant transport mechanism in a fluid-particle system can be found using the Peclet Number, which is the ratio between the convective transport rate and the Brownian diffusive transport rate. For a sphere, the Peclet number is defined as [36]

$$\mathrm{Pe} = \frac{3\pi\mu\gamma d_p^3}{4k_bT} \quad (1)$$

where μ is the viscosity, γ is the shear rate, d_p is the diameter of the primary particle, k_b is the Boltzmann constant, and T is the absolute temperature. Values of $Pe>>1$ indicate that orthokinetic aggregation is the dominant mechanism. Since orthokinetic aggregation is governed by the local shear rate, the properties of the aggregates are highly dependent on the value of this important parameter.

Aggregates produced in stagnant conditions (perikinetic aggregation) are also classified according to the collision efficiency [37], which is the probability that particles remain together after a collision [35]. When the collision efficiency has a value of 1, the aggregation process is called diffusion-limited colloid aggregation (DLCA) [38–40]. In DLCA, the repulsive interparticle forces are negligible and the aggregation rate depends only on the Brownian motion. The aggregates formed in DLCA are large, weak, and porous (low in effective density) [37]. When only a fraction of the collisions results in a persisting aggregate (sometimes referred as a "bond"), it is called reaction-limited colloid aggregation (RLCA) [38,39]. In RLCA, the presence of repulsive interactions between particles plays an important role and aggregates are generally small, moderately dense, and stronger than those formed through DLCA [37].

When the aggregate is transported, the hydrodynamic force (F_{hyd}) exerted on it competes with the aggregate cohesive force (F_{coh}) that holds the particles together. Two phenomena can be

observed: (i) restructuring ($F_{hyd} \approx F_{coh}$), when some connections within the aggregate break and some new connections are formed [18]; and (ii) ($F_{hyd} > F_{coh}$), where the interparticle cohesive forces cannot balance the external hydrodynamic forces [17].

The focus of this project is to study the breakage of aggregates formed under shear flow conditions similar to those encountered in industry i.e., under conditions where $Pe >> 1$.

2.2 Fractal nature of aggregates

Once an aggregate is formed, its two most important characteristics are size and density, as both influence the effectiveness of solid-liquid separations. Many studies have described the relation between effective density and aggregate size using the mass fractal dimension d_f [41–44]:

$$\rho_{eff} = (\rho_a - \rho_l) \propto L^{d_f - 3} \quad (2)$$

where ρ_{eff} is the effective density of the aggregate, ρ_a is the aggregate density, ρ_l is the liquid density, L is the aggregate size.

A fractal is an object that shows similarity to itself on different scales of observation; in other words, in fractal objects, the same geometrical shape pattern is seen on any scale [37]. It is accepted that large aggregates made of identical particles can be seen as fractal objects and follow a power-law relation between the aggregate mass M and size L, i.e.:

$$\mathrm{M} \propto \mathrm{L}^{d_f} \quad (3)$$

The aggregate size in Equation (3) can be the maximum length or the average diameter (depending on the experimental technique). Gregory suggests that the precise definition of size does not affect Equation 3 if the choice of L is consistent [44].

The mass fractal dimension d_f can vary from 1 to 3. Larger values of d_f are related to a more compact structure; lower values imply loose or open aggregates. As d_f decreases, the structure of the aggregate is more open until it reaches a d_f value of 1, which describes a hypothetical aggregate where its particles form a line [1,37].

2.3 Particle interactions

The interaction force between particles affects the aggregation process through the collision efficiency. The probability of aggregate formation is very low in the case of high repulsion between particles, and the aggregation will occur very slowly [1] i.e., RLCA aggregation occurs. In addition, the force between particles has been linked to the aggregate strength [16,24], a parameter that represents the aggregate's ability to resist breakage. Interaction between particles is often described using the DLVO theory [2]. The DLVO theory was named because of the work by Derjaguin and Landau in 1941 and Verwey and Overbeek in 1948.

The force between two particles depends on the separation distance from surface to surface and the potential energy at that distance [2]

$$F = -\frac{dV}{dH} \tag{4}$$

where F is the force between particles, V is the potential energy, and H is the separation distance. When identical colloidal particles are near enough to each other, they are subjected to attractive van der Waals forces. Interparticle repulsive forces can also be present in a colloidal system, especially in fluids with a low concentration of ions. The DLVO theory assumes that the energy of the colloidal system is the sum of the Van der Waals energy and the repulsive electrostatic double-layer energy [4,45]

$$V_{DLVO} = V_{VDW} + V_{EDL} \quad (5)$$

Van der Waals interactions

Van der Waals (vdW) interactions result from the electrostatic interactions between permanent charges distribution in the molecules (dipole-dipole forces), permanent charge distribution and induced charges distribution (dipole-induced dipole forces), and the force caused by oscillation of the orbital electrons and the interaction with the induced dipoles in the neighbourhood (London or dispersion forces) [2]. The interaction energy between two macroscopic bodies takes the form:

$$V = A_{11}\, f(geometry) \quad (6)$$

where A_{11} is the Hamaker constant, which quantifies the strength of the vdW interaction between two particles of material 1in a vacuum [2].

The attractive force depends on the particle properties, the medium and the particle separation distance [45]. For two spheres of equal radius 'a' in a vacuum, with H << a, the attractive potential energy is described as:

$$V = -\frac{A_{11}a}{12H} \quad (7)$$

and thus

$$F = -\frac{A_{11}a}{12H^2} \quad (8)$$

The Hamaker constant shown in Equation (6) is independent of the body's geometry and only depends on the material. It often has values between 10^{-19} J and 10^{-21} J [46]. When the particles are suspended in a medium, the effective Hatmaker is A_{121}, with subscript 1 indicating that two

particles of material 1 are separated by medium 2. In this case, the effective Hamaker constant can be estimated using [45]

$$A_{121} = A_{11} + A_{22} - 2A_{12} \tag{9}$$

Electrostatic repulsive forces

Surface charges appear on solid bodies that are immersed in a solution because of the ionization of the groups present on their surface [2]. This occurs due to processes such as adsorption of ions, isomorphic substitution, and ionization or dissociation of surface groups [45]. In an electrolyte solution, the electrical charges on the particle surface are balanced by an equivalent number of oppositely charged ions (or counterions), forming the so-called electrical double layer on the particle surface [45].

The resulting electrical potential is described by the Poisson-Boltzmann equation. For two spherical particles, the potential is calculated as [2,4]:

$$V = \frac{64\ n_o kTa}{\kappa^2}\ tanh^2\left(\frac{ze\psi}{4kT}\right)\ e^{-\kappa H} \tag{10}$$

where n_o is the bulk electrolyte concentration, k is the Boltzmann constant, T is the absolute temperature, ψ is the surface potential of the sphere in isolation, z is the valency of the electrolyte and e is the elementary charge.

The value κ is an important parameter. It is the inverse of the Debye length, and it is also called the Electric Double-layer thickness and provides a typical range of interaction between particles. In other words, it provides an estimation of the distance where the repulsive forces become important. The constant κ depends on the electrolyte composition and the temperature and is calculated using:

$$\kappa = \sqrt{\frac{e^2}{\varepsilon k_b T} \sum_i z_i^2 c_i N_a} \qquad (11)$$

where *c* represents the molar concentration of the i-type ion and *Na* is the Avogadro number.

When the repulsive and attractive potentials are added, the DLVO interaction energy results in:

$$V_{DLVO} = V_{NET} = \frac{64\ n_o K\ Ta}{\kappa^2}\ tanh^2\left(\frac{ze\varphi}{4k_b T}\right) e^{-\kappa H} - \frac{Aa}{12H} \qquad (12)$$

A graph of electric potential acting on the particles as a function of particle separation distance presents some important characteristics. As shown in Figure 2-1, for surfaces with high surface charge or for suspensions with a low electrolyte concentration, the curve displays a maximum in the interaction energy. This maximum is the energy barrier for aggregation. Below a certain value of surface potential or above a certain salt concentration the energy barrier falls below zero, and the interaction curve approaches the van der Waals curve. This suspension is unstable, and the particles attract each other at all separation distances.

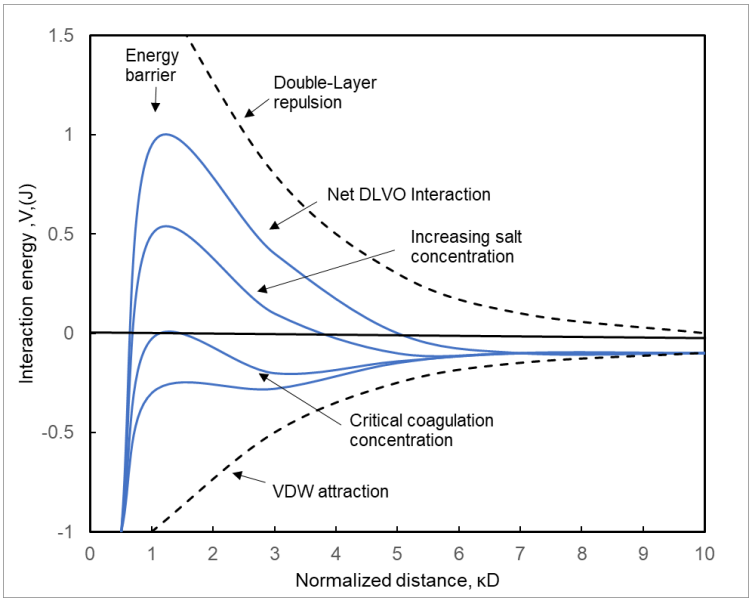

Figure 2-1 Potential energy as a function of the distance for DLVO interactions. Modified from Israelachvili [2].

The net interaction potential shown in Equation (12) can be used to calculate the minimum concentration of electrolyte that can destabilize a suspension. This concentration is called the critical coagulation concentration and is graphically represented in Figure 2-1 corresponding to the concentration in which the maximum in the interaction energy (the energy barrier) is equal to zero. The critical coagulation concentration can be calculated applying two conditions for solving Equation (12); specifically, the maximum in the curve with $dV_{DLVO}/dH = 0$ and with the condition for no energy barrier $V_{DLVO} = 0$.

2.4 Aggregate cohesive strength and breakage

Despite the large body of literature on aggregation, e.g., [1,47–52], there are only a few studies regarding aggregate breakage. This topic has been studied mainly through numerical simulations [25,31,53–55], and only a few experimental studies are found, probably because the delicate and fragile nature of most aggregates makes the experiments complicated and challenging [16,17,19,23,25–28].

The aggregate cohesive force is an important parameter, as it represents the capacity to resist breakage. Initially, Parker et al. [24] described the aggregate cohesive force (also called the aggregate strength) as dependent on the number and the strength of interparticle contacts within the aggregate. Tambo and Hozumi [56] tried to relate the aggregate strength with its structure: they assumed that the aggregate strength was a function of aggregate density. Kobayashi et al. [19] proposed a model for the aggregate strength as the product of the cohesive force between primary particles and the number of contacts between disintegrating fragments in the aggregate, i.e., the aggregate cohesive force is a function of the structure.

The strength of an aggregate is evaluated through the force required to break it. In the literature, two approaches to obtain the values for aggregate strength can be found: through direct or indirect measurements. Direct measurements of aggregate strength were performed by Yeung and Pelton [57], who measured the force needed to pull apart single polymeric aggregates using a micropipette technique. They found that the aggregate strength is independent of the aggregate size; they argued that aggregate breakup occurs at the weakest point along the direction of the rupture, i.e., in the point with the narrowest cross-section. The location of the minimum cross-section and its magnitude may be random.

The aggregate strength can also be examined through indirect measurements. Different authors relate the aggregate strength, at the point where breakage is observed, from the relation between the aggregate size at a steady-state and the average shear rate in the aggregation vessel [24,58,59]. The relation is normally expressed in the following form:

$$d = C\gamma^{-p} \tag{13}$$

where C is the aggregate strength coefficient, γ is the average shear rate, p is the aggregate size exponent. This expression, initially proposed by Parker et al. [24] is used by many researchers [15,19,23,25–27,29,60]. The exponent p has been related to the cohesive strength, reported values vary in the range from 0.29 to 0.81 [61]. This concept is explained in Figure 2-2, which shows 3 types of theoretical aggregates: type (a) has a slope of zero and represents a strong aggregate in which the size is independent of the shear applied; type (b) shows a moderate slope, and thus is a stronger aggregate than the type (c) [61].

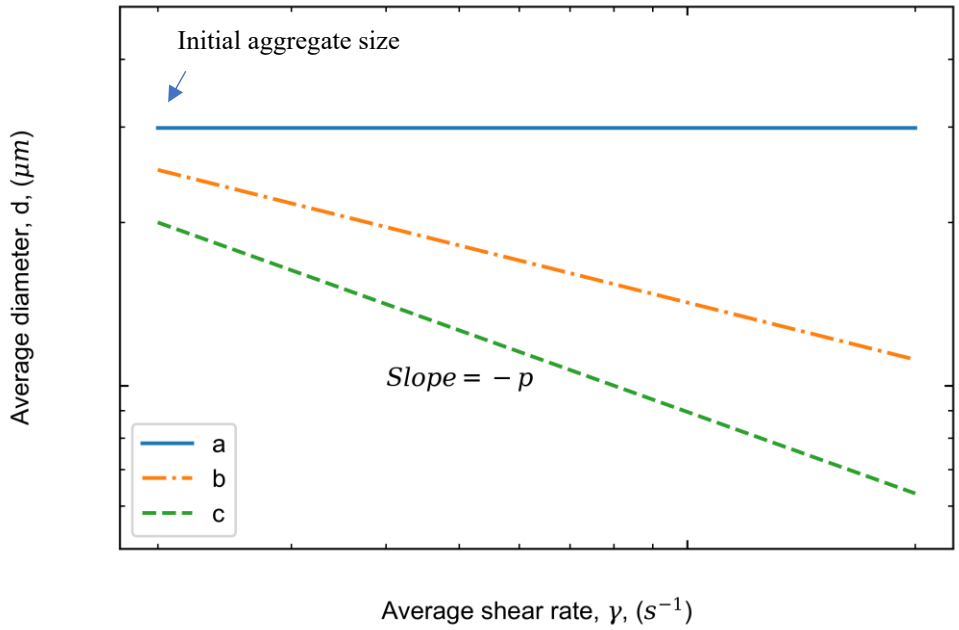

Figure 2-2 Relation between aggregate size and velocity gradient for 3 types of flocs. Modified from Jarvis 2005 [61].

Sonntag and Russel (1986) [29] conducted breakage experiments with latex particles in the laminar regime. They found that experiments with high salt concentrations produced stronger aggregates; in other words, aggregates produced in suspensions with high salt concentrations experience less breakage compared with aggregates produced in low salt concentrations. These results correlate the cohesive strength with the DLVO theory, highlighting the significance of cohesive forces on the aggregate. In addition, they found that there was an increase in the fractal dimension from 1.6 to 2.48 after shearing, showing that the breakup of aggregates is accompanied by restructuring.

Zaccone et al. 2010 [62] developed a mechanistic model to relate the hydrodynamic stress to the change in aggregate size caused by breakage at steady state. The model proposes that the

scaling exponent p depends directly on the fractal dimension. For dense aggregates with a mass fractal dimension greater than 2.4, in laminar conditions, the authors propose the relation:

$$d = C\gamma^{-p} \qquad p = -2(3 - d_f)[2(3.8 + 1) - \upsilon] \tag{14}$$

where the value of υ=-1/ (3-d_f) for aggregates with a fractal dimension d_f between 2.4 and 2.6 and for aggregates with fractal dimension close to 3, $\upsilon \approx$ - 0.4.

More recently, Harshe et al. 2011 [25] investigated the breakage of loose (d_f = 1.7) and compact (d_f = 2.7) aggregates of latex microspheres using two different primary particle sizes, through experiments and simulations. The results show that the exponent p depends on the initial d_f and is independent of the primary particle size. Only the loose aggregates saw restructuring.

The cohesive force is also estimated from the stable aggregate size at a certain hydrodynamic force, which is commonly estimated as:

$$F_{HYD} \approx \sigma d_{agg}^2 \tag{15}$$

where: d_{agg} is the aggregate diameter, σ is an averaged hydrodynamic stress exerted on the aggregate, which for Newtonian fluids in laminar flow is estimated as

$$\sigma \approx \mu\gamma \tag{16}$$

where γ is the velocity gradient or shear rate, μ is the dynamic viscosity. Very dilute suspensions of aggregates must be studied, so that aggregation or re-aggregation can be neglected [21,26]. The hydrodynamic force acting on the aggregate is quite difficult to calculate because of particle rotation [63]; however, the calculation can be simplified, assuming that the aggregate behaves as a sphere. The maximum hydrodynamic force for a rotating sphere in simple shear flow was described by Boller and Blaser [64] as:

$$F_{HYD} = \frac{5}{8}\pi\mu d^2\gamma \quad (17)$$

This relation was later confirmed by Coufort et al. [65], with the maximum force being exerted at a 45^o angle to the flow axis.

Kobayashi [16,17] performed breakage experiments using laminar converging flow and calculated the cohesive force of aggregates of latex and soil particles. The experimental results showed that the cohesive force is constant and independent of the aggregate size. A scaling exponent of -0.5 was obtained, which is in agreement with the results of other authors [21,23,26,53].

Frappier et al. 2010 [50] also calculated the cohesive force of latex aggregates but used aggregation experiments. It was found that the cohesive force scales with $d_{agg}^{1.5}$, which is in disagreement with the results obtained by Yeung and Pelton [57], and Kobayashi [16,17] who found that the aggregate cohesive force was constant. An explanation for this disagreement was not provided.

In addition to experiments, numerical investigations have been used to understand the phenomenon of breakage and restructuring [25,66], and especially to understand the impact of hydrodynamics on the aggregates [31,67,68]. However, numerical simulations are restricted to aggregates with very small values of Reynolds number (Re_{agg}), which is a function of the shear rate:

$$Re_{agg} = \frac{4\gamma\rho d_{agg}^2}{\mu} \quad (18)$$

Novel numerical approaches have been developed to evaluate aggregate breakage and restructuring at finite values of Re_{agg} [31]. These approaches take into account the effect of flow inertia [69]. Despite the number of experimental investigations found in the literature, very few experimental results are at conditions that allow comparison with simulations. i.e., finite values of

Re_{agg}. Performing breakage experiments at low shear rates with a low Reynolds number can help to validate results from simulations.

2.5 Shearing devices

In the literature, different types of shearing equipment are used in the study of aggregates. Stirred tanks are used widely as they provide turbulent conditions similar to industrial operations [21,23,36,50,58,70–75]. However, the heterogeneous shear field complicates the analysis, as the aggregates are exposed to different values of shear rate during the duration of the experiment [76]. For example, Spicer et al. [58] studied latex particle aggregation using three different impellers and found differences in the characteristics of the aggregates formed. This was caused by the differences in flow patterns created by the three different impellers.

Experiments with laminar pipe flow were reported by different authors [49,77–79]. The use of pipes or tubes in aggregation studies has some advantages: for example, it provides a more uniform shear field than a mixing tank. Also, sampling is easier since the samples can be extracted at the end of the pipe. However, the shear rate in laminar pipe flow varies from the wall shear rate to zero in the center of the pipe.

In the experimental study of Serra et al. [47] different shearing apparatuses were compared: an oscillating grid, a stirred tank with a paddle mixer and a Couette cell device, over a shear rate range of 4 to 102 s^{-1}. They found no differences in the aggregate size for the stirred tank and the oscillating grid, but they observed larger aggregates in the Couette cell. They concluded that Couette cell provides a nearly constant shear rate in laminar conditions, unlike the stirred tank and the oscillating grid, which have regions of high shear rates where aggregates break.

Previous studies clearly show that most of the flow devices are less appropriate for aggregate studies because of the heterogeneous velocity field, which makes it difficult to quantify the hydrodynamic force acting on the aggregates. Recalling that the simplest profile is produced by simple shear flow, it is advantageous to consider which shearing devices best mimic this type of flow. Although not practical, simple shear is the steady flow between two parallel plates, with one static plate and a moving plate with velocity V, as shown in Figure 2-3. is characterized by a linear velocity profile, which produces a constant shear rate.

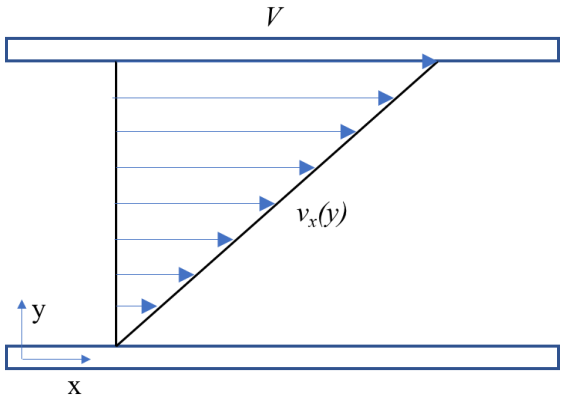

Figure 2-3 Representation of simple shear flow.

The device that best reproduces simple shear flow is the Couette cell [29,30,36,52]. The Couette cell comprises two concentric cylinders, with the fluid confined in the gap between the cylinders. Commonly, only the inner cylinder rotates. The shear rate in this device can be easily controlled by varying the speed of the rotating inner cylinder. An illustration of a Couette cell is shown in Figure 2-4. Ives [80] considers that the Couette cell with a very narrow gap ($R_1/R_2 > 0.95$) is equivalent to simple shear since the curvature in the velocity profile is quite small and thus can be neglected.

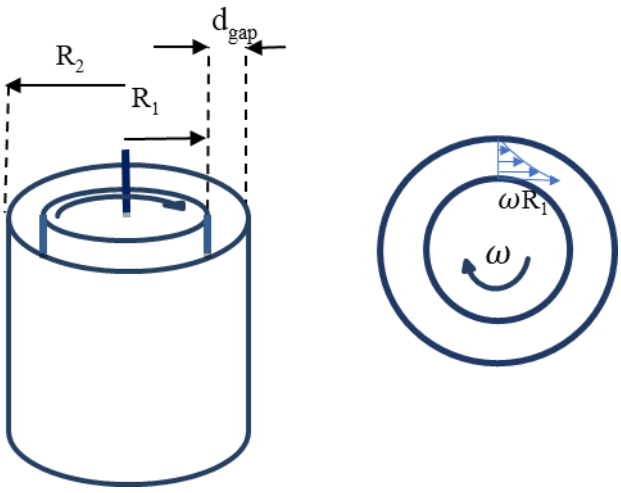

Figure 2-4 Schematic illustration of a Couette cell.

The flow regime inside the Couette Cell is characterized by the Taylor number (*Ta)*, which is the dimensionless number that relates the centrifugal forces and the viscous forces [81]:

$$Ta = \frac{\omega \rho R_1^{0.5}(R_2 - R_1)^{1.5}}{\mu} \tag{19}$$

where $\omega = 2\pi N/60$ is the angular velocity of the inner cylinder in rad/s, ρ is the fluid density, R_2 and R_1 are the radii of the outer and inner cylinders and μ is the fluid viscosity. At low values of *Ta,* the Couette cell produces a laminar azimuthal flow regime called laminar Couette flow [82]. As ω increases, a series of instabilities in the fluid appears. In the first instability, the fluid travels in helical paths around cylinders in layers of counter-rotating toroidal vortices [83,84]. This pattern is known as Taylor vortex flow. The point at which the fluid regime changes is characterized by the critical Taylor number (Ta_{cri}). The value of Ta_{cri} is approximately 41; however, Taylor [85] published a better approximation of the critical Ta_{cri} as a function of concentric cylinder geometry:

$$Ta_{cri} = \frac{\pi^4 (1 + \frac{d_{gap}}{2R_1})}{0.0571\left(1 - 0.652\frac{d_{gap}}{R_1}\right) + 0.00056\left(1 - 0.652\frac{d_{gap}}{R_1}\right)^{-1}} \tag{20}$$

With a further increase in the rotation rate, the vortices oscillate. This fluid pattern is called wavy vortex flow. At higher values of *Ta*, the fluid regime become turbulent. Table 2.1 shows the flow stability criteria for Newtonian fluids in an inner rotating cylinder Couette cell [86,87].

Table 2-1 Flow regimes in a Couette cell [86,87].

Regime	Taylor number
Laminar Couette flow	$Ta < Ta_{cri}$
Taylor vortex flow & Wavy Vortex Flow	$Ta_{cri} < Ta < 400$
Turbulent Regime	$Ta > 400$

In this project, the investigation is restricted to laminar Couette flow. Due to the uniform distribution of shear, the laminar Couette flow is ideal for controlling the shear rate acting on the aggregates. In the laminar Couette flow regime, the average shear rate can be calculated as [36,81]:

$$\gamma = \frac{1}{R_2 - R_1} \int_{R2}^{R1} \frac{2\omega R_1^2 R_2^2}{(R_{1-}^2 R_2^2) r^2} dr \qquad (21)$$

and thus

$$\gamma = \frac{2\omega R_1 R_2}{R_2^2 - R_1^2} \qquad (22)$$

Additionally, this fluid flow can be easily modelled. It is convenient to carry out experiments in this flow regime because the results produced can be compared with simulations.

2.6 Aggregate characterization

The most commonly used methods to determine aggregate size are image analysis and light scattering [88]. The selection of a particular technique depends on the chosen experimental

conditions. Light scattering devices, such as the Malvern-Mastersizer have been used widely for aggregate characterization because the measurements are fast and reproducible. However, this technique presents some drawbacks for the study of aggregates. The equipment uses an ultrasonic pre-treatment of the sample, which must be avoided to prevent aggregate breakage. Also, the sample needs to be homogenized with a stirrer that may break the aggregates, then the sample is transported using narrow tubes in which the aggregates are subjected to more shear. Problems with altering the aggregate size distribution using this technique have been reported in the literature [89,90].

The use of image analysis has improved in the last decade because of advances in electronics, such as fast frame cameras and the use of digital cameras [27,49]. With these advancements, the aggregate size can be obtained directly from the visualization of the sample. First, it is necessary to obtain high-quality pictures of the aggregates, i.e., images in which the particles are in focus and clearly distinguishable from the background. Then the digital images are analyzed using software, where aggregate properties can be obtained, such as the area, perimeter, and lengths.

One of the major benefits of image analysis is that the pictures can be obtained directly without sampling (in situ). In situ image analysis is preferred due to the danger of modifying the aggregate during sampling [91]. Sample extraction and preparation can change the aggregate size and structure, resulting in samples that may be not representative of the aggregates inside the vessel. For example, Spicer et al. [58] showed that three different sampling techniques produced different aggregate sizes. In this thesis, an in situ image analysis system was designed to avoid sampling. The major goal of this approach is to remove any additional source of shear that can cause changes in the aggregate size and structure.

From 2D images, the most commonly used descriptor of size is the area-based diameter [92], which is defined as the diameter of a circle with the same projected area as the particle or aggregate:

$$d = \sqrt{\frac{4A}{\pi}} \tag{23}$$

where d is the circle of equivalent diameter and A is the projected area of the aggregate [88].

Fractal dimensions can be extracted from aggregate images. Since the images only show the projection of the aggregate and not all the particles are visible, there is no simple way to obtain the mass fractal dimension [44]. However, one can characterize the structure of aggregates in 2D images through the perimeter fractal dimension d_{pf} [21,23,26,51,71,93], which is described as:

$$A \propto P^{2/d_{pf}} \tag{24}$$

The description of d_{pf} implies that its value is in a range between 1 (corresponding to a perfectly spherical aggregate) and 2 (corresponding to a linear aggregate). The value for d_{pf} is obtained from the slope of the linear regression of the logarithm of area versus the logarithm of the perimeter from a population of aggregates, as is shown in Figure 2-5.

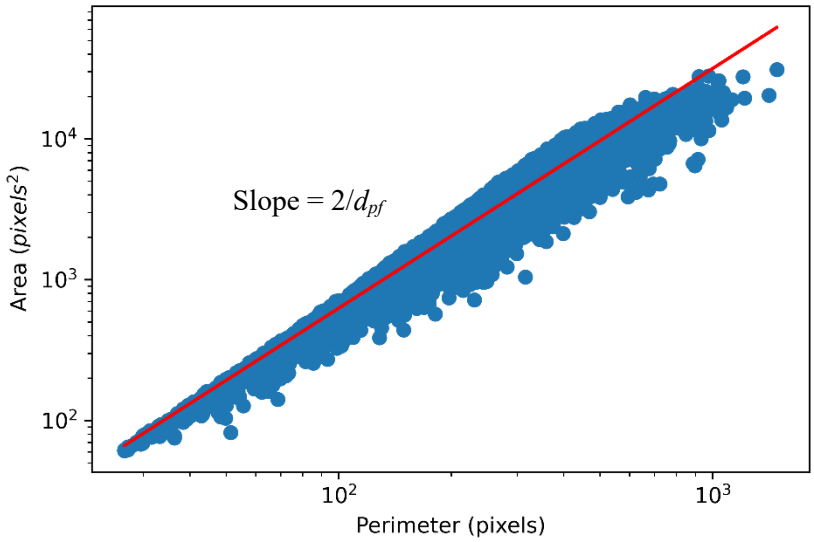

Figure 2-5 Relationship between area and perimeter of aggregates.

The value of d_{pf} does not provide a direct relation to the mass fractal dimension d_f; however, its measurement is simple and offers a good understanding of aggregate morphology. To formulate a relation between d_f and d_{pf}, Lee and Kramer [94] analyzed computational fractal aggregates with a chosen d_f ($1.8 < d_f < 2.4$) and d_{pf} was then extracted. The authors found that the perimeter fractal dimension is inversely proportional to the mass fractal dimension. Ehrl et al. [93] presented a new relation that extended the value of d_f in the range from 2.2 to 3. They included the "blur effect", having taken into account the uncertainties related to the limitation of the optical system.

2.7 Summary and scope of the current study

Based on the literature review presented here, the following points can be extracted:

- The aggregate properties are the results of a dynamic equilibrium between aggregation and breakage [43,52]. The two principal aggregate characteristics are size and density, which

are related through the fractal dimension [37]. The fractal dimension is widely used to describe the aggregate structure.

- The extent of aggregate breakage due to shear is governed by the aggregate strength, which is commonly related to (a) the interparticle force occurring between individual particles and (b) the aggregate structure [16,29,61].
- The aggregate cohesive force (F_{coh}) is difficult to measure, and instead has been related to the exponent of the power-law relation between the aggregate size and the average shear rate [59,61]. However, F_{coh} can be evaluated indirectly by performing breakage experiments in well-defined hydrodynamics. Very dilute conditions are needed to avoid aggregation or re-aggregation [72].
- The Couette cell has been shown to be uniquely useful in controlling the hydrodynamics [15,84]. The shear rate can be easily controlled by changing the rotational velocity of the inner cylinder.

This review also exposes some deficiencies that require further exploration:

- The available information about aggregate breakage at relatively low shear rates is quite limited. This information is needed because it can be used in the design and optimization of flocculators and settlers in industrial operations, like tailings treatment and wastewater treatment. In addition, it is necessary to obtain breakage data at finite values of Re_{agg}, which can then be used to validate computational models.
- The determination of aggregate size and structure using in situ image analysis is preferred. It has been applied successfully in previous aggregation experiments [18,55,84]. This method allows one to monitor the aggregates without extracting them from the vessel,

thereby eliminating any external source of shear. To the author's knowledge, there has not been an attempt to study aggregate breakage using an in situ and non-invasive method, the breakage studies reported in the literature used light scattering as a measurement technique or microscopy [25,26,72].

Therefore, the objectives of this research project:

- To investigate the aggregate size and structure of the fragments, after breakage of latex aggregates in laminar Couette flow.
- To obtain undisturbed measurements of the aggregate size using in situ image analysis.
- To evaluate the aggregate cohesive strength of aggregates using laminar shear flow.
- To minimize the effect of the gravity force in the system by selecting particles that have a density similar to that of water, to obtain a neutrally buoyant fluid-particle system.

Chapter 3 Experimental Method

3.1 Introduction

Aggregate breakage experiments were carried out in laminar Couette flow, to obtain the aggregate size and structure as a function of shear rate. The Couette cell geometry was chosen because of its velocity profile and nearly constant shear rate across the gap. Consequently, the hydrodynamic force acting on the aggregates could be calculated easily. The Couette cell device is described later in this chapter.

To study only the effect of the hydrodynamic forces, without the complication of settling, a neutrally buoyant fluid-particle system is used. Section 3.2 describes the materials used in the experiments. A suspension using latex microspheres and sodium chloride solution was prepared. The latex suspension was then sheared in the Couette cell to produce the aggregates. Section 3.3 provides the details of the equipment used in the experiments. After aggregates are produced from the primary particles at a low shear rate, the rotating speed (the shear rate) of the Couette cell was increased to induce aggregate breakage. Section 3.4 lists the procedures followed to form and break the aggregates.

An in situ image technique was used to determine the size and structure of the aggregates. A detailed description of the image acquisition system is found in Section 3.3.2. Also, the algorithm for image analysis is described in Section 3.5.

3.2 Materials

3.2.1 Latex microspheres

Sulphate latex microspheres, with lot number 1855064, were purchased from Thermo Fisher Scientific. The particles as received were in suspension at a concentration of 8% w/v. The supplier reports an average diameter of 2.0 ± 0.1 μm obtained from transmission electron microscopy; the density of the latex microspheres at 20 ºC is 1.055 g/cm^3 as reported in its certificate of analysis. This type of particle was chosen because they are neutrally buoyant when a salt solution is used as the suspending liquid. By matching the density of the solution with the density of the particles, the effect of gravity and centrifugal forces can be neglected, enabling one to focus on the effect of the hydrodynamic force.

3.2.2 Sodium chloride solution

The fluid needs to be Newtonian, have a density of 1.055 g/cm^3, be transparent, and have sufficient salt concentration to be above the critical coagulation concentration of the latex particles. To match the density of the particles and to provide the ions necessary to promote aggregation, a solution of 1.4 M of sodium chloride was used for all the experiments. The dry NaCl was purchased from Thermo Fisher Scientific (lot number 193463). The concentration of NaCl solution is greater than the critical coagulation concentration reported by Guerin et al. [95] which is 1.1M and ensures that the particles are fully destabilized.

The pH of the NaCl solution was measured with a Mettler Toledo Seven Multi system pH-meter. The pH probe was placed inside the NaCl solution to check the pH, which was adjusted with 0.1 N sodium hydroxide solution until it reached a pH of 7 (more details in Section 3.4.1).

The pH meter was calibrated daily. Then the solution was filtered twice using a Whatman™ Filter Paper - Grade 5 to ensure the solution was free of solids.

3.2.3 Milli-Q water and NaOH

De-ionized water was obtained from an in-lab Milli-Q system. All the solutions used in this study were made using de-ionized water. All the beakers, the Couette cell and instruments used throughout the study were washed with detergent and tap water and rinsed thoroughly before every experiment to remove any ions that can affect the aggregates. The sodium hydroxide used to neutralize the NaCl solution was prepared in the lab. The solid NaOH was obtained from Thermo Fisher Scientific (lot number 161309).

3.2.4 Calibration particles

Two different white polyethylene microspheres, "WPMS 106-125um" (lot number 1039-282-16-3) and "WPMS-250-300um" (Lot number 955-280-2-1) were purchased from Cospheric LLC and used to calibrate and validate the image analysis procedure. The particles were received in dry powder form.

3.3 Equipment

The main experimental setup comprised the Couette cell attached to an overhead stirrer, and the optical equipment to capture the images of the aggregates, which is shown in Figure 3-1. The optical equipment included a translation stage with a high-speed camera equipped with a magnification lens and a halogen lamp.

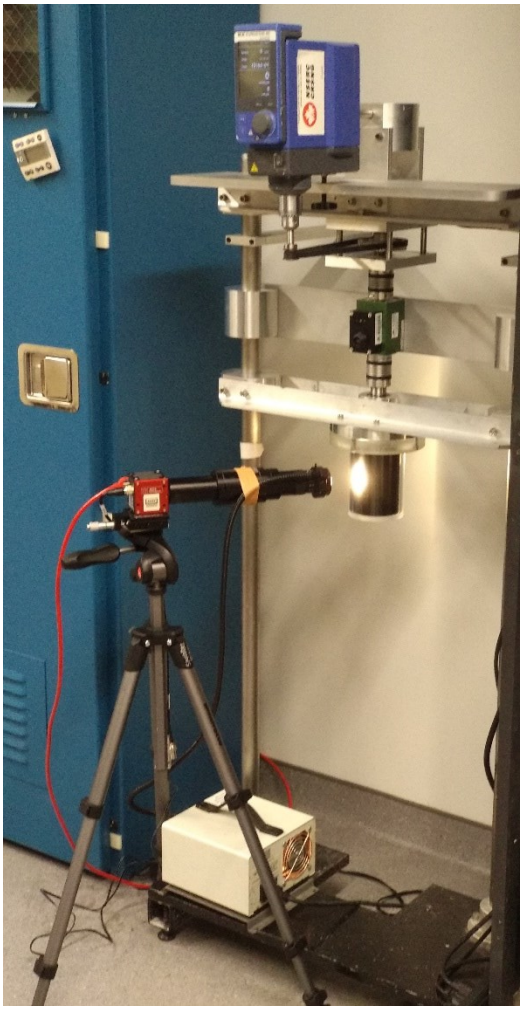

Figure 3-1 Experimental setup showing the optical equipment (left) and the Couette cell (right).

3.3.1 Couette cell

The Couette cell constructed for this project had a rotating inner cylinder with a diameter of 73.5 mm and a height of 110 mm. The stationary outer cylinder (i.d.= 76.5 mm) was made of plexiglass to allow the observation of the interior of the Couette cell. The inner cylinder was black in colour to increase the contrast between the white aggregates and the background. The gap between the inner and the outer cylinder is 1.5 mm.

Inner cylinder rotation was driven using an IKA Eurostar 60 digital mixer. The mixer was attached to a 17.26 mm diameter gear and the Couette cell inner cylinder was attached to a 78 mm diameter gear, and both gears were connected through a belt. For the aforementioned geometry, the maximum angular velocity in laminar Couette flow is 3.54 rad /s or 33.85 RPM, which is obtained when the Taylor number from Equation (19) equals the critical Taylor number from Equation (20) (Ta_{cri} = 42.07). The shear rate for the maximum angular velocity in laminar flow is 88.5 s^{-1}, which is calculated using Equation (22). The minimum shear rate is 17.6 s^{-1}, which corresponds to the minimum angular velocity that can be obtained. The minimum angular velocity of the inner cylinder is 0.69 rad/s or 6.63 RPM.

3.3.2 Image acquisition system

Aggregate size was determined using two-dimensional image analysis. Images were taken in situ using an AOS PROMON 501 CMOS high-speed camera attached to a translation stage, which allows focusing on any desired point in the gap between the concentric cylinders. The pixel size of the camera is 5.5 µm x 5.5 µm in a 2/3" sensor. The resolution of the photos is 1920×1080 pixels. The camera can capture images in full resolution at a rate of 85 frames per second. However, the image capture frequency was set at 10 fps to avoid capturing the same aggregate in two consecutive photos.

The camera was connected via gigabit ethernet to a PC. The camera exposure time, balance, contrast, and gain were adjusted via software according to the light conditions. To eliminate motion blur, the exposure time was set to 200µs. The camera was attached to a VZM™ 1000 Zoom Imaging Lens from Edmund Optics. The magnification used during this study was set to 2.5X which provides a theoretical pixel size of 2.2 µm. However, the resolution was checked using a 2

mm micrometre calibration slide, giving a pixel size of 2.25 µm. The nominal field of view at 2.5X is 4.224 mm × 2.376 mm.

The field of view was illuminated using a ring light attached to the lens. The light source was a Schott ACE 1 Fibre Optic Light using a 150w halogen lamp. The lamp was turned on only during the measurement to avoid excessive exposure to the intense light that may increase the temperature of the suspension.

Figure 3-2 VZM™ 1000 Zoom Imaging Lens from Edmund Optics and AOS PROMON 501 high-speed camera used in the present study.

3.3.3 Microscope

The particle size distribution (PSD) of commercially available white polyethylene particles obtained from the image experimental equipment was compared with the PSD from microscopy in static conditions to validate the image analysis method. Particle images were collected using a Carl Zeiss Axioscope 5 microscope equipped with an Axiocam 208 colour camera and a Zeiss N-Achroplan 10x/0.25 objective lens. These images had a resolution of 1920 × 1080 pixels with a ratio of 0.37 µm/pixel.

3.4 Procedures

This Section describes all the experimental procedures and additionally, all the relevant Safe Work Procedures (SWPs) are provided in Appendix B.

3.4.1 Sodium chloride solution preparation

The sodium chloride solution was prepared using a 1000 mL volumetric flask and was neutralized in a 2000 mL beaker using a 0.1 N sodium hydroxide. The NaCl solution was mixed using an IKA RW-20 overhead stirrer. After neutralization, the solution was filtered to reduce any remaining solid. The solution was stored in 500 mL brand new plastic bottles. A more detailed procedure is given below:

Preparation of NaCl 1.055 g/cm^3 solutions

Batches of 1L NaCl solution were prepared using the following procedure:

- Weigh 82 g of NaCl using an analytical balance.
- Carefully add the weighted NaCl to a 1000 mL volumetric flask and fill it to the mark with deionized water.
- Mix thoroughly until the NaCl is fully dissolved.
- Transfer the solution to a 2000 mL beaker.
- Attach a 3-blade marine propeller impeller (3cm diameter) to the IKA RW 20 digital overhead stirrer.
- Place the beaker with the overhead stirrer and ensure to place the impeller 5 cm above the bottom of the beaker.

- Measure pH, if the pH of the solution is below 7 add a drop of 0.1 M NaOH.
- Start the stirrer at a low to avoid spills and slowly increase the impeller speed to 200 RPM.
- Stop the overhead stirrer and measure the pH
- In case the pH is not 7.0, repeat the last 4 steps until the solution reaches pH 7.0.
- Using a pycnometer, check the density, which must be 1.055 g/cm^3.

$$\rho_{Brine} = \rho_{water} * weight_{brine}/weight_{water} \quad (25)$$

- In case of the brine density is higher than 1.055 g /cm^3 (particles will float), add the required amount of deionized water to reach the required density and repeat the procedure to adjust pH and density.
- If the density is lower than required (particles will settle during the experiment), add the calculated amount of NaCl and repeat the procedure to dissolve the NaCl. Adjust pH and density.
- Once the desired density and pH are obtained, filter the brine using a funnel and a 0.2 µm Whatman™ Filter Paper - Grade 5.
- Store the solution in a 500 mL plastic bottle and label.

3.4.2 Aggregation and breakage procedure

The aggregates were formed in the Couette cell at a particle concentration of 10^{-4} v/v to ensure a diluted system, so that overlapping of particles in the images was eliminated. The conditions required to form the aggregates were kept constant in all the experiments and are shown in Table 3-1. A volume of 50 mL of NaCl solution (density =1.055 g/cm^3 pH=7.0) was measured and poured into the Couette cell outer cylinder. Then, 66 µL of the stock (as received) latex particle

suspension was added to the NaCl solution to obtain a particle concentration of 10^{-4} v/v. The outer cylinder was attached to the Couette cell structure, and the suspension was mixed at the maximum RPM possible (which is 2000 RPM for the overhead mixer and 442.5 RPM at the inner cylinder) for 5 minutes to break any aggregates already formed. After that, the shear rate was changed to 17.6 s^{-1} to start the aggregation process. The optical equipment was placed in front of the Couette cell and images were taken and analyzed to measure the aggregate size distribution while shearing. The suspension was sheared steadily for 3 hours, producing randomly shaped aggregates, as seen in Figure 3-3. Aggregate size and structure were measured at t =2.5h and t = 3h after starting the aggregation process to confirm that the aggregate size distribution does not change, and a steady state is reached.

Table 3-1 Detailed conditions for aggregates formation

Parameter	Value
Solid Concentration (v %)	0.01
Primary particle diameter	2 µm
Primary particle density	1.055 g/cm^3
pH	7
Salt concentration	1.25 M
Fluid density	1.055 g/cm^3

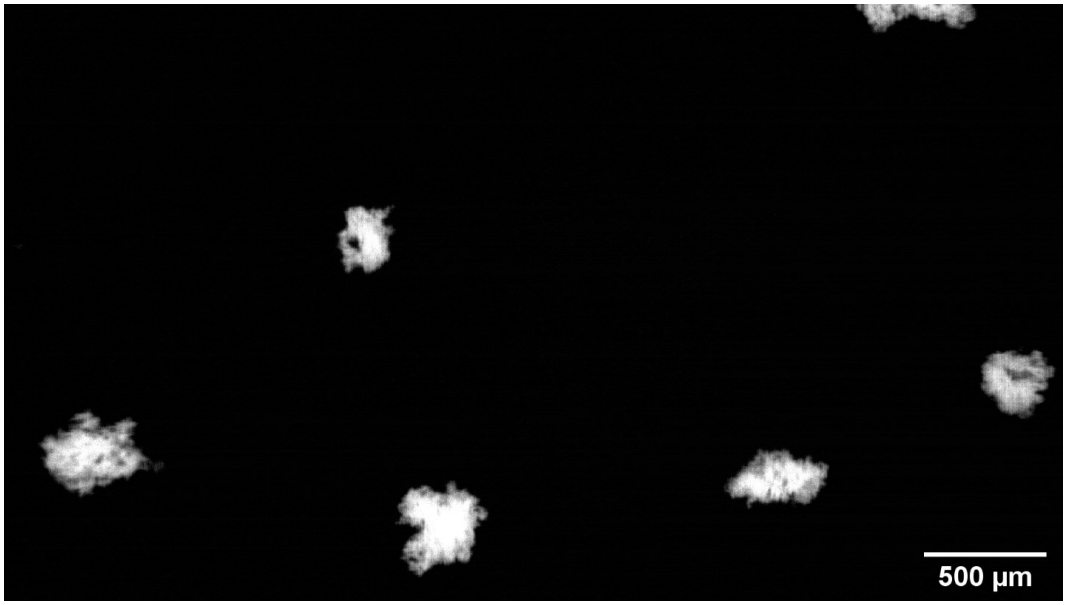

Figure 3-3 Sample of an image of aggregates formed at 17.6s^{-1} in the Couette cell.

Once the aggregates reach a constant aggregate size distribution, the rotational speed (and shear rate) was increased. Different breakage experiments were conducted at the conditions described in Table 3-2. After increasing the shear rate, the aggregate size and structure were measured until a new steady state was confirmed. All the experiments were at room temperature (20°C). A more detailed step-by-step procedure of the aggregation and breakage experiment is provided below.

Table 3-2 Range of shear rates used for aggregate breakage experiments. The aggregation step was performed at an overhead stirrer speed of 30 RPM (inner cylinder 6.6 RPM), which corresponds to a shear rate of 17.6 s^{-1}

Experiment	Overhead Stirrer (RPM)	Inner Cylinder (RPM)	Shear Rate (s^{-1})
1	50	11.0	28.9
2	60	13.3	34.7
3	100	22.1	57.9
4	130	28.8	75.3
5	150	33.2	86.8

Aggregation and breakage procedure.

- Measure 50 mL of NaCl solution using a 50 mL graduate cylinder and place the solution in the Couette cell.
- Measure 66 μL of the concentrated sulphate latex beads using a 100 μL micropipette; add the latex solution to the Couette cell chamber.
- Attach the outer cylinder with the initial suspension to the Couette cell structure, tighten the screws until the Couette cell is sealed.
- Start the Couette cell overhead stirrer at 2000 RPM for 5 min, which is the maximum impeller speed of the stirrer.
- After 5 minutes of mixing, change the rotational velocity of the Couette cell overhead stirrer to 30 RPM (shear rate of 17.6 s^{-1}).
- Place the camera in front of the Couette cell and use the translation stage to adjust the distance until the aggregates are in focus.
- After 2.5 h of shearing at 17.6 s^{-1}, measure the aggregate size distribution taking 2000 pictures at 10 fps and save them on the PC, then run the image analysis script to obtain the aggregate size distribution.
- Quantify the aggregate size distribution every 15 minutes until the aggregate size distribution is constant.
- Once the aggregate size distribution is constant, increase the shear rate to the desired value to initiate the aggregate breakage phase (see Table 3-2 for the range of shear rates studied).

- Measure the aggregate size distribution every 15 minutes until the aggregate size distribution is constant.

3.5 Image analysis

To obtain the aggregate morphology, 2000 photos were taken at a frequency of 10 fps and saved in the PC controlling the camera. Around 3000 - 10000 aggregates were considered for plotting the distribution. Images were then processed using an image process script that was written as part of this project. The code was written in Python 3.8.5 using the image processing and analysis functions from the OpenCV 4.4.0 and Scikit-image 0.17.2 packages. The image processing code is provided in Appendix A.

The workflow for the image analysis is shown in Figure 3-4, and as shown, had six steps: reduce the image noise, identify particles from the background, remove particles that are touching the border, closing the image (morphological transformations), measurement of the properties of the particles as area, perimeter, bounding box, and identification and removal of out-of-focus particles.

To begin, it was necessary to reduce the noise associated with the images by reducing the small random changes in pixel values. The Gaussian filter function was found to be effective at reducing the noise, by attenuating the variation of greyscale intensity. The noise reduction is quite important because it reduces the errors in the thresholding process and avoids the detection of false small aggregates around a larger one. The effect of the Gaussian filter can be observed by comparing Figure 3-5 and Figure 3-6.

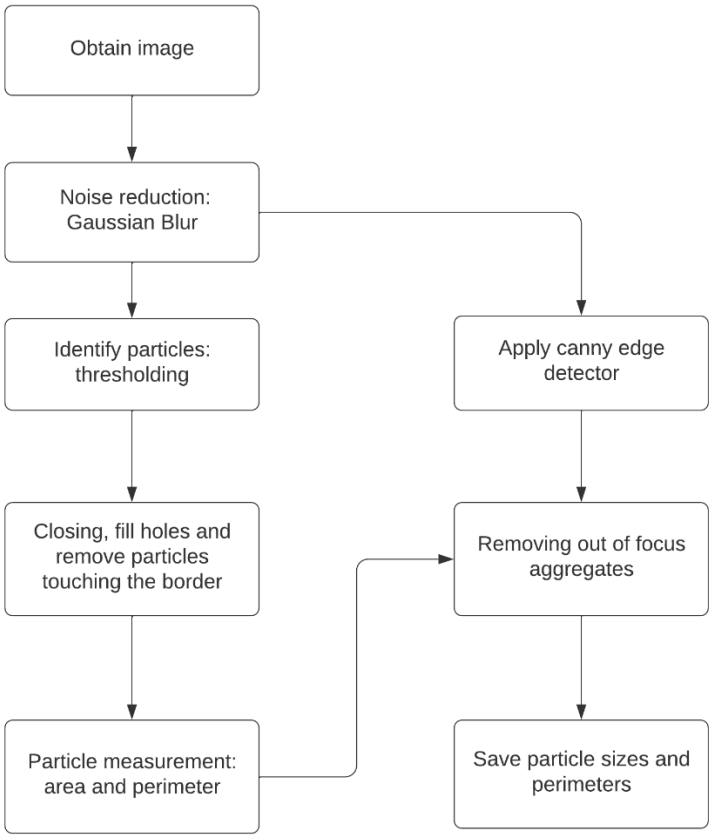

Figure 3-4 Flowchart describing the image analysis process.

After filtering, the next operation is thresholding. This method distinguishes the particles from the background based on pixel values. In a greyscale image, the colours are represented by numbers in a range between 0 to 255. Black is represented by a pixel value of 0 and white has a pixel value of 255. The thresholding value recognizes the white aggregate from the dark background, and it produces a binary image with a pixel value of zero for the pixels below the thresholding value and a pixel value of 1 for the pixels containing values above the thresholding value. The result of the thresholding operation is shown in Figure 3-7.

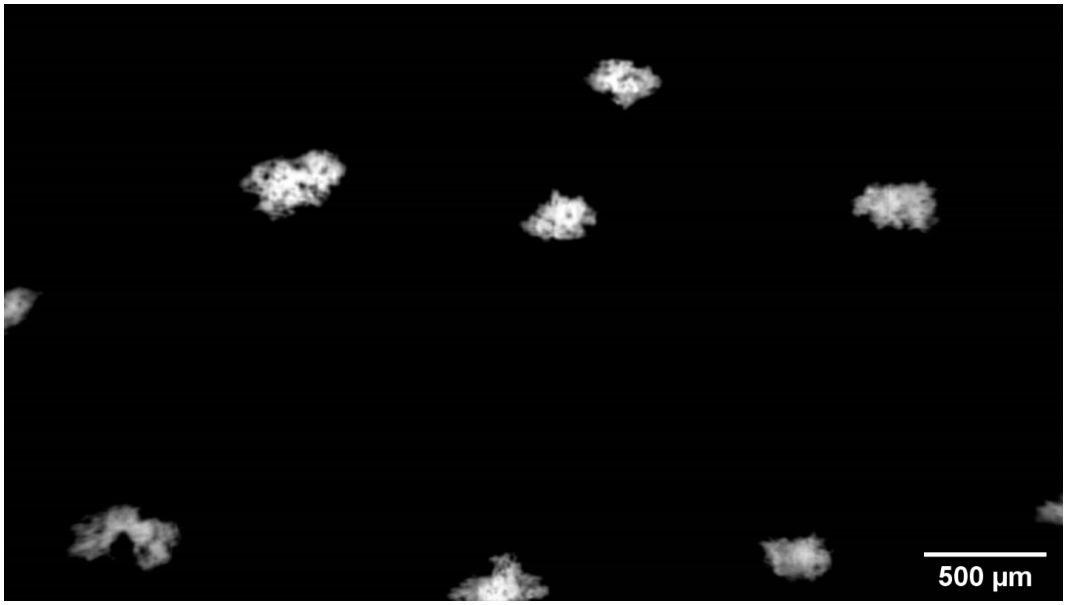

Figure 3-5 Original image without processing.

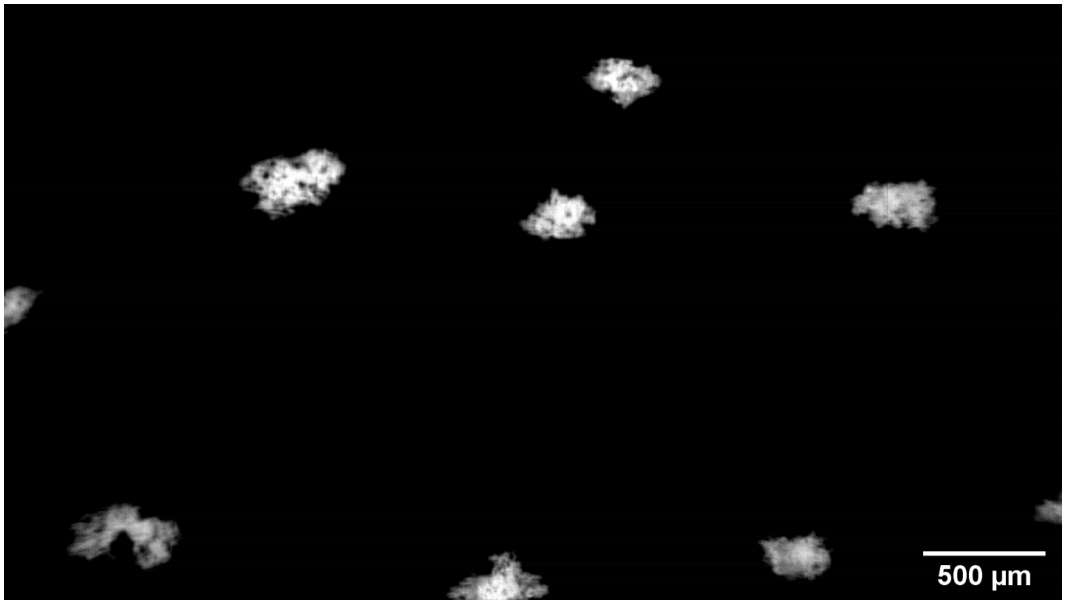

Figure 3-6 Example of an image after Gaussian blur was applied.

Figure 3-7 Binary image obtained from thresholding operation.

Once the thresholding operation is performed, holes and gaps can appear within an aggregate because of its complex structure. These gaps must be eliminated before the extraction of the area and perimeter. The function “Closing” allows one to bridge some gaps in the particles and smooth the perimeter of the aggregates. The closing operation results from two morphological operations: erosion and dilation. Erosion discards the pixels near the object boundary depending upon the size of a given kernel. Dilation, which is the opposite of erosion, increases the area of the white object depending on the size of the specified kernel. Closing the object alters the area and shape of the objects, therefore, the closing kernel was chosen as small as possible to minimize changes in the aggregate shape while cleaning and eliminating small objects surrounding the aggregate. To measure total the area of the aggregates, the fill holes operation needs to be performed before the calculation of the aggregate area. One more operation is removing the particles touching the border of the image. Since the area of these aggregates cannot be measured because they are not totally exposed, they must be removed from the image. An image result of all the operations (closing,

filling holes and removal of particles touching the border) is shown in Figure 3-8, this image is used to extract the aggregates information: area and perimeter.

Figure 3-8 Binarized image after closing, holes filled and particles touching the border were removed.

The image processes such as the Gaussian filter and the Closing function are necessary for the extraction of the aggregate's information. However, these functions can alter the shape of the aggregates and modify the perimeter. Therefore, the value of the perimeter extracted after processing (Figure 3-8) is associated with but and does not represent the actual aggregate perimeter from the aggregates in Figure 3-5. The perimeter, along with the area, allow the description of the aggregate structure in terms of perimeter fractal dimension. In this study, comparison of aggregate structure should be considered to be qualitative.

To detect out-of-focus particles, the Canny edge detector algorithm was used. In an object that is out of focus, the edges cannot be detected, while objects that are in focus show clearly defined edges. The canny edge detector returns an image with the detected edges (Figure 3-9). In

the case where no edges are found in the aggregate location, the aggregate is considered out of focus and is removed from the database.

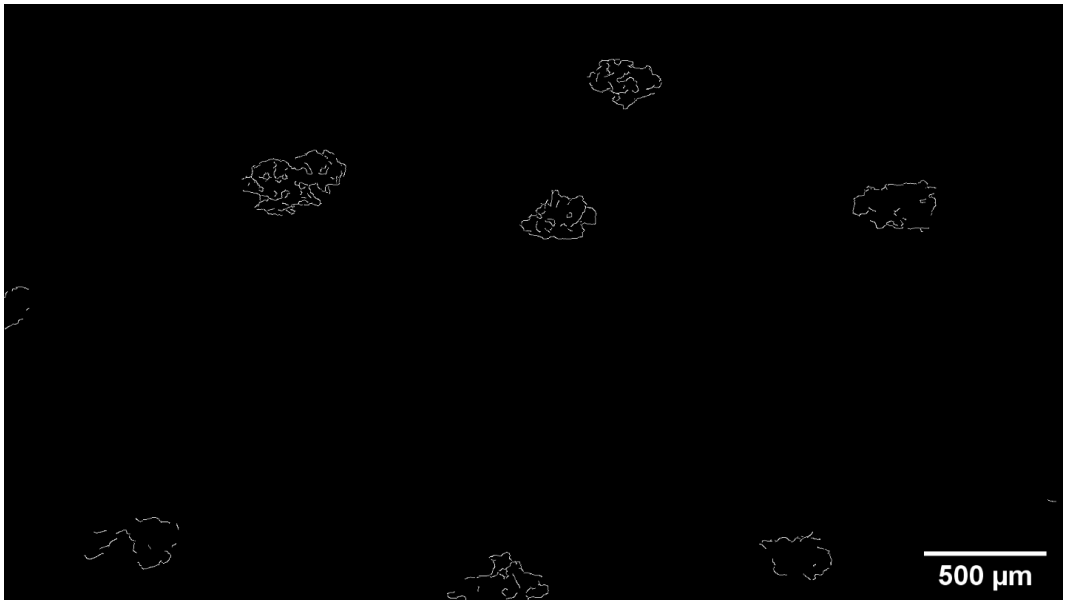

Figure 3-9 Outcome of the Canny edge detector algorithm.

The image analysis method was validated by comparing the particle size distribution (PSD) of white microspheres obtained in the rotating Couette cell with the PSD of the microspheres observed by microscopy. Further, to verify that the PSD does not change with shear rate, the benchmarking experiment was repeated at different shear rates and the PSDs were compared. These results are discussed in Section 4.1. The detailed procedures followed to obtain the validation results using the white microspheres was provided below.

Procedure to obtain the white microsphere PSD in the Couette cell using the camera for validation of the image analysis method.

- Measure 50 mL of millQ water using a 50mL graduate cylinder and place the solution in the Couette cell chamber.

- Measure 0.1 grams of white polyethylene microspheres ("WPMS 106-125um" or "WPMS-250-300um") using an analytical balance and add it to the Couette cell chamber.
- Gently mix the suspension.
- Attach the outer cylinder containing the suspension to the Couette cell structure and tighten the screws until the Couette cell is sealed.
- Start the Couette cell overhead stirrer at 2000 RPM (shear rate of 1158 s^{-1}), which is the maximum velocity given by the stirrer to disperse the particles and break any aggregate that might be present. Mix for 5 min.
- Reduce the Couette cell overhead stirrer velocity to 30 RPM (shear rate of 17.6 s^{-1})
- Place the camera in front of the Couette cell, use the translation stage to adjust the distance until the particles are in focus.
- Measure the aggregate size distribution by taking 1000 pictures at 10 fps and saving the pictures on PC, then run the image analysis script to obtain the aggregate size distribution.
- Repeat the procedure from the mixing at 2000 RPM, taking the pictures of the particles at the rotational speed according to Table 3-3.

Table 3-3 Range of RPM to obtain the particle size distribution of white microspheres

Overhead Stirrer (RPM)	Inner cylinder (RPM)	Shear Rate (s^{-1})
30	6.6	17.6
50	11.0	28.9
60	13.3	34.7
100	22.1	57.9
130	28.8	75.3
150	33.2	86.8

Procedure to obtain the white microsphere PSD through microscopy for validation of the image analysis method.

- Turn on the microscope, the lamp and the camera and the computer.
- Start the microscope software.
- Place a sample of white microspheres ("WPMS 106-125um" or "WPMS-250-300um") on the microscope slide using a micro spatula.
- Place the prepared microscope slide on the microscope bench.
- Select the 10X objective lens by rotating the nosepiece, a click sound indicate that is in place.
- Rise the mechanical stage height carefully to prevent touching the lens with the slide/sample. Stop when the focus is achieved, sharpen the image by using the fine focus knob.
- Capture the images by sweeping the microscope over the slide. Capture a minimum of 650 particles.
- Process the images to obtain the PSD.

Chapter 4 Results and Discussion

This chapter presents the results obtained in this study, showing the effect of shear rate on aggregate breakage. This chapter is divided into 3 sections: first, validation results of the image analysis technique using the white microsphere suspension are presented. This validation step was also used to adjust the image analysis algorithm. The second section of this chapter discusses the results for the aggregation stage of the experiments. Here, the aggregates were formed under specific conditions and were then characterized in situ to verify that the distribution of size and structure were relatively constant before breakage experiments were conducted. The third section discusses the results of the breakage tests conducted at different shear rates. The effect of shear rate on the aggregate size and structure is discussed. The aggregate cohesive force is calculated with the results obtained from the breakage experiments.

4.1 Validation of the image analysis method

The dynamic optical technique described in Chapter 3 was validated by comparing the in situ measurements of particle size distribution (PSD) of white microspheres (in the Couette cell) with the PSD of the same microspheres obtained through microscopy. Further, to verify that the PSD does not change with shear rate, the experiments were repeated at different shear rates and the PSDs were compared.

Two different white polyethylene microspheres, “WPMS 106-125um” (lot number 1039-282-16-3) and “WPMS-250-300um” (Lot number 955-280-2-1) were purchased from Cospheric LLC and used to validate the image analysis procedure. The particles were received in dry powder form.

In order to obtain in-focus images with sufficient contrast between the particles and the background, images were captured using a Carl Zeiss Axioscope 5 microscope, at 10X magnification. A particle sample was placed on a microscope glass slide as received . Then images were obtained and processed to obtain the PSD. More than 650 particles were captured in order to have sufficient data to produce a reliable PSD.

A suspension of 0.1 g white latex microspheres dispersed in 50 mL of deionized water was used to validate the PSD measurements. The suspension was placed in the Couette cell and mixed at the maximum speed of the overhead mixer (shear rate of 1158 s^{-1}) for 5 minutes to disperse and break any aggregates that might be present. After the mixing, the motor speed was reduced to obtain a shear rate of 17.6 s^{-1}; then 1000 images were taken (around 4000 particles were captured) and analyzed using the script described in the previous chapter and presented in Appendix A.

The comparison of the particle size distribution (PSD) for the first set of microspheres (" WPMS 106-125um") is shown in Figure 4-1 and Table 4-1. The description of particle size distribution and descriptors used is presented in Appendix C. The in situ PSD shows particles slightly larger than the ones captured by the microscope. However, the mean diameter using the microscope is 128.2 µm and is 126.5 µm from the in situ measurements. The particle Sauter mean diameter obtained using microscopy is 134.3 µm and is 133.3 µm from the in situ measurement. For quantitative comparison, Table 4-1 presents the statistical descriptors of the PSD including the Sauter mean diameter, $d_{3,2}$, the standard deviation of the diameter, σ_d, mean diameter, $d_{1,0}$, the 10th number percentile of the diameter, *d10*, 50th number percentile of the diameter, *d50*, and the 90th number percentile of the diameter, *d90*. Table 4-1 shows that the statistical descriptors for the data obtained using the microscope and the camera are similar. The parameter that shows more variation is the *d90*, which differs by approximately 10%. This is because there was a fraction of

particles that had an elongated form since not all the particles were consistently spherical. Microphotographs of the particles "WPMS 106-125um" are presented in Appendix D. These elongated particles laid down on the microscope slide, exposing a larger area, while in the Couette cell the particles were rotating.

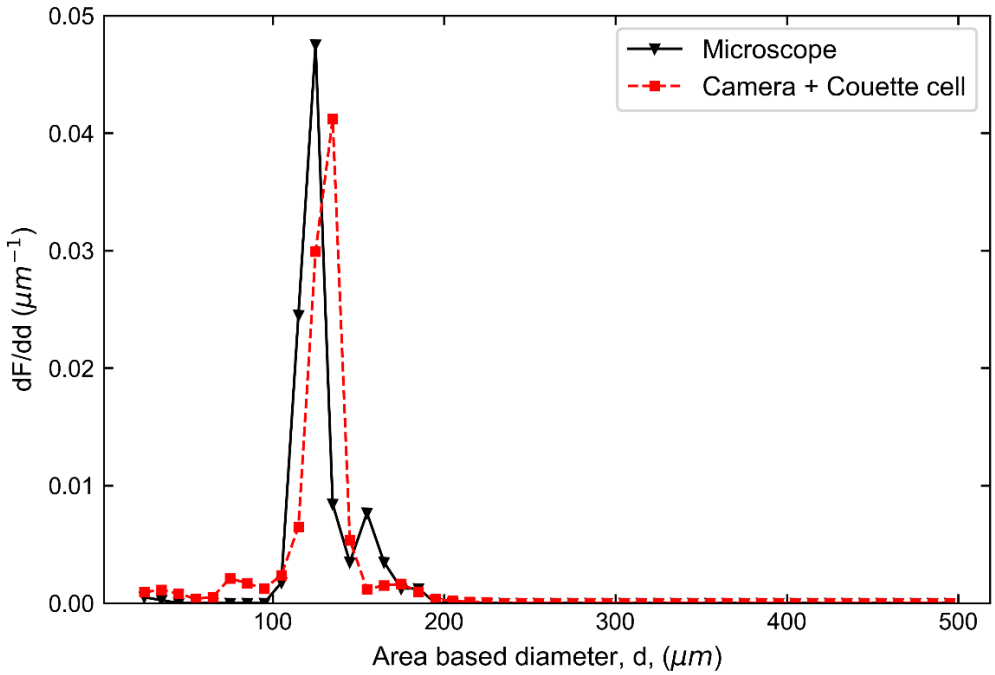

Figure 4-1 Comparison of the number based differential frequency distributions of white polyethylene spheres "WPMS 106-125um" from images taken using the microscope and using Couette cell imaging equipment with γ=17.6 s^{-1}.

Table 4-1 Statistical parameters of the particle size distribution of white polyethylene spheres "WPMS 106-125um" taken using the microscope and using Couette cell imaging equipment, with γ=17.6 s^{-1}

	Microscope-static	Couette cell imaging equipment	Difference
$d_{3,2}$, µm	134.3	133.2	0.8 %
σ_d, µm	20.7	23.5	13.4 %
$d_{1,0}$, µm	128.2	126.5	1.4 %
d10, µm	113.6	116.5	2.6 %
d50, µm	125.7	131.1	4.3%
d90, µm	155.4	139.9	10.0%

Regarding the test done using the second set of microspheres ("WPMS-250-300um"), Figure 4-2 shows two monomodal distributions that overlap each other, with a mean of 285.2 µm for the

PSD obtained using microscopy and a mean of 284.6 µm for the PSD obtained with a camera in the Couette cell imaging setup. The statistical parameters of the PSD are shown in Table 4-2. In this case, the values are quite similar between the camera and the microscope; the only parameter that is different between the two PSDs is the standard deviation because the PSD obtained by the camera includes the small particles. Small particles are likely to be covered by larger particles on the microscope slide.

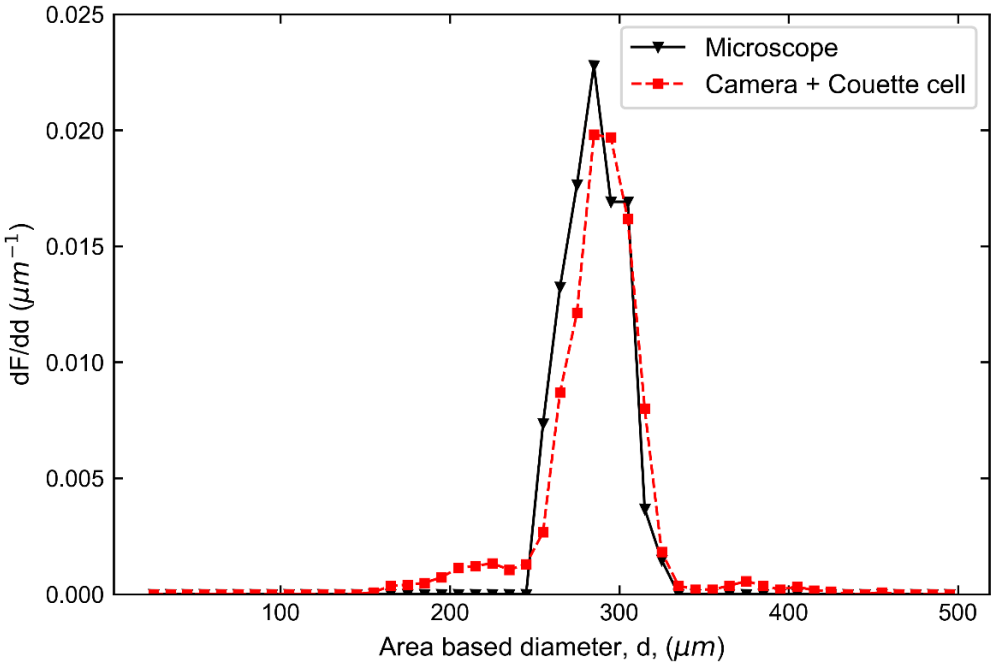

Figure 4-2 Comparison of the number based differential frequency distributions of white polyethylene spheres WPMS-250-300um from images taken using the microscope and using Couette cell imaging equipment, with $\gamma=17.6s^{-1}$.

Table 4-2 Statistical parameters of the particle size distribution of white polyethylene spheres "WPMS 250-300um" taken using the microscope and using Couette cell imaging equipment, with $\gamma=17.6\ s^{-1}$

	Microscope	Couette cell imaging equipment	Difference
$d_{3,2}$, µm	287.1	290.5	1.2 %
σ_d, µm	16.3	29.6	81.5 %
$d_{1,0}$, µm	285.2	284.6	0.2 %
d10, µm	263.7	259.1	1.4 %
d50, µm	285.5	287.7	0.8 %
d90, µm	306.5	309.4	0.9 %

Effect of rotational speed in particle size measurements

The process of measuring the PSD in the Couette cell was repeated for the different shear rates used in this study (17.6 s^{-1}, 28.9 s^{-1}, 43.7 s^{-1},57.9 s^{-1},75.3 s^{-1} and 86.8 s^{-1}), to check the effect of the shear rate on the particle size measurements. The results for microspheres "WPMS 106-125um" are presented in Figure 4-3 and for "WPMS-250-300um" in Figure 4-4. For both suspensions, the six curves obtained for the different shear rates are overlapping, showing almost identical particle size distributions.

To compare quantitatively the measurement, the statistical parameters of the PSD for both sets of particles are shown in Table 4-3 and Table 4-4. The values presented are almost constant for each type of microsphere. It can be concluded that for the range of shear rates studied, the particle velocity did not cause any effect in the images that could produce inaccuracy in the particle size measurement.

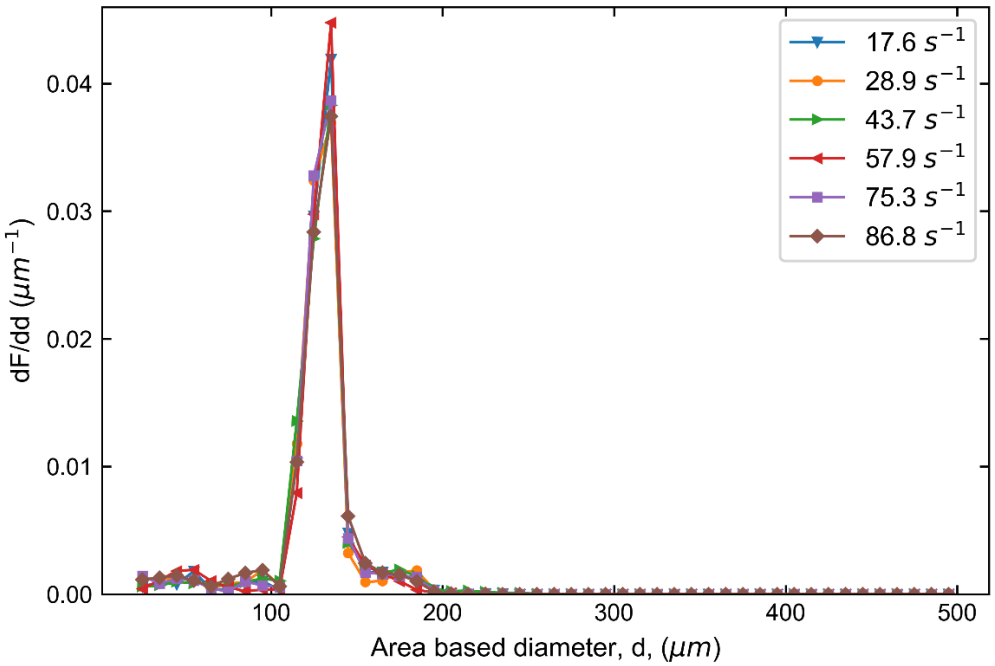

Figure 4-3 Number-based particle size distribution of particles WPMS-106-125 um at different Couette cell shear rates.

Table 4-3 Statistical parameters of the particle size distribution of particles WPMS-106-125um at different Couette cell shear rates

Shear rate, s^{-1}	$d_{3,2}$, µm	σ_d, µm	$d10$, µm	$d50$, µm	$d90$, µm	$d_{1,0}$, µm
17.6	134.50	22.90	116.16	130.79	140.93	127.76
28.9	133.72	25.55	113.91	128.96	139.50	125.31
43.7	136.43	24.41	114.74	130.23	144.97	128.13
57.9	133.19	23.51	116.51	131.06	139.89	126.46
75.3	133.91	24.28	116.17	129.83	140.51	126.58
86.8	133.76	25.86	97.54	130.13	142.50	125.36

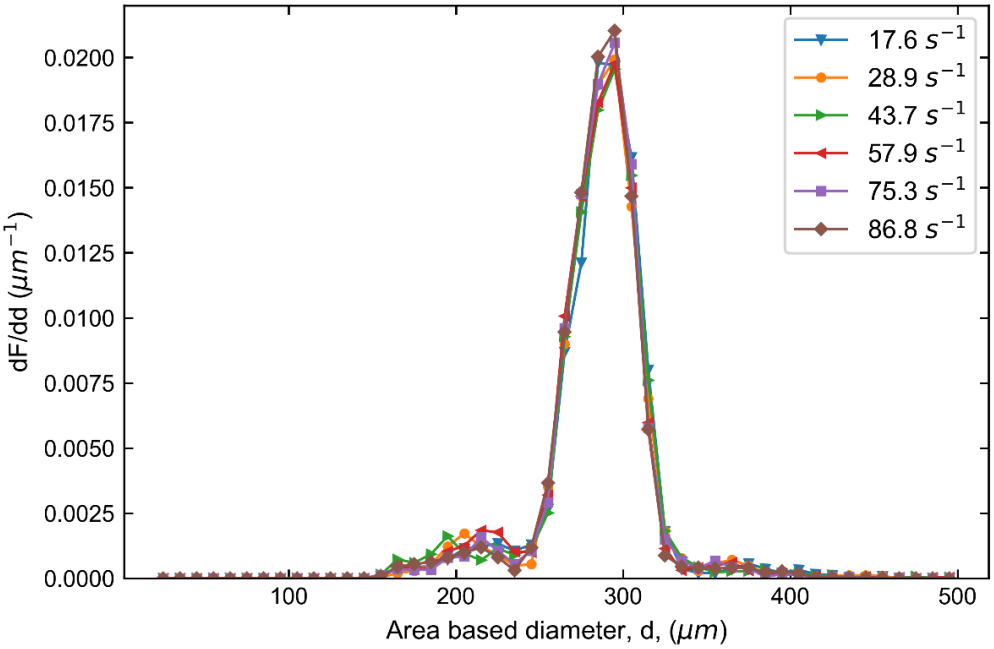

Figure 4-4 Number-based particle size distributions of particles WPMS-250-300um at different Couette cell shear rates.

Table 4-4 Statistical parameters of the particle size distribution of particles WPMS-250-300um at different Couette cell shear rates

Shear rate, s^{-1}	$d_{3,2}$, µm	σ_d, µm	*d10*, µm	*d50*, µm	*d90*, µm	$d_{1,0}$, µm
17.6	293.21	31.16	257.27	289.32	312.49	286.63
28.9	292.97	31.68	258.91	288.41	312.42	286.08
43.7	292.03	33.17	256.99	288.53	312.29	284.65
57.9	292.09	32.00	259.74	287.51	311.15	285.10
75.3	292.09	30.18	260.16	288.43	310.29	285.71
86.8	290.50	29.62	259.07	287.68	309.38	284.61

4.2 Particle aggregation

In this study, aggregates were produced in the Couette cell at a shear rate of 17.6 s^{-1}, with 2 µm microspheres as the primary particles. The Peclet number for the system calculated using Equation (1) is 82. This value is high enough to ensure that perikinetic aggregation will not happen and only orthokinetic is considered as the primary transport mechanism. These conditions were selected to produce aggregates large enough for optical visualization, as shown in Figure 4-5. In each of the experiments, the Couette cell was loaded with a homogeneous and dispersed suspension at a particle volume fraction of $\phi = 10^{-4}$ $^{v}/_{v}$. The aggregation time was set to 3 hours, which is long enough to allow for the aggregates to reach their steady-state size. The aggregate size distribution (ASD) was measured at 2.5 hrs and 3 hrs to confirm that steady-state size had been achieved. The simple shear produced by the Couette cell makes the aggregates rotate and move horizontally across the field of view, allowing one to take pictures of different aggregates.

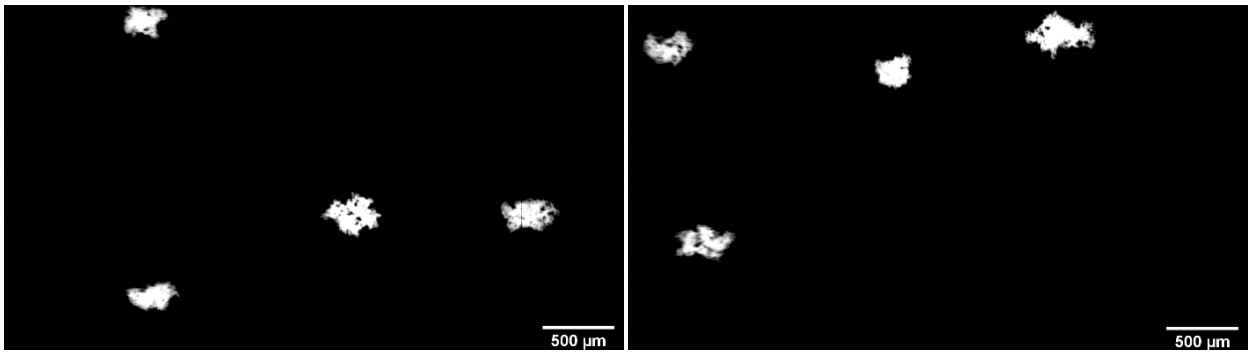

Figure 4-5 Snapshots of the aggregates prepared at 17.6 s^{-1} after 2.5 hrs.

Figure 4-6 presents the ASDs of the aggregates formed at 17.6 s^{-1}. Figure 4-6 a) shows the differential frequency distributions, in which the ASDs follow a log-normal distribution with a mode of about 250µm. Although some curves show some differences at the extremes, the ASDs clearly overlap each other. Figure 4-6 b) shows the cumulative frequency distribution. In this case, the curves match almost perfectly. Table 4-5 shows the statistical parameters describing the ASDs including the perimeter fractal dimension d_{pf} and the estimated mass fractal dimension d_f. The values provided in Table 4-5 are quite similar, indicating that the aggregates produced in the experiments have a reproducible size and size distribution.

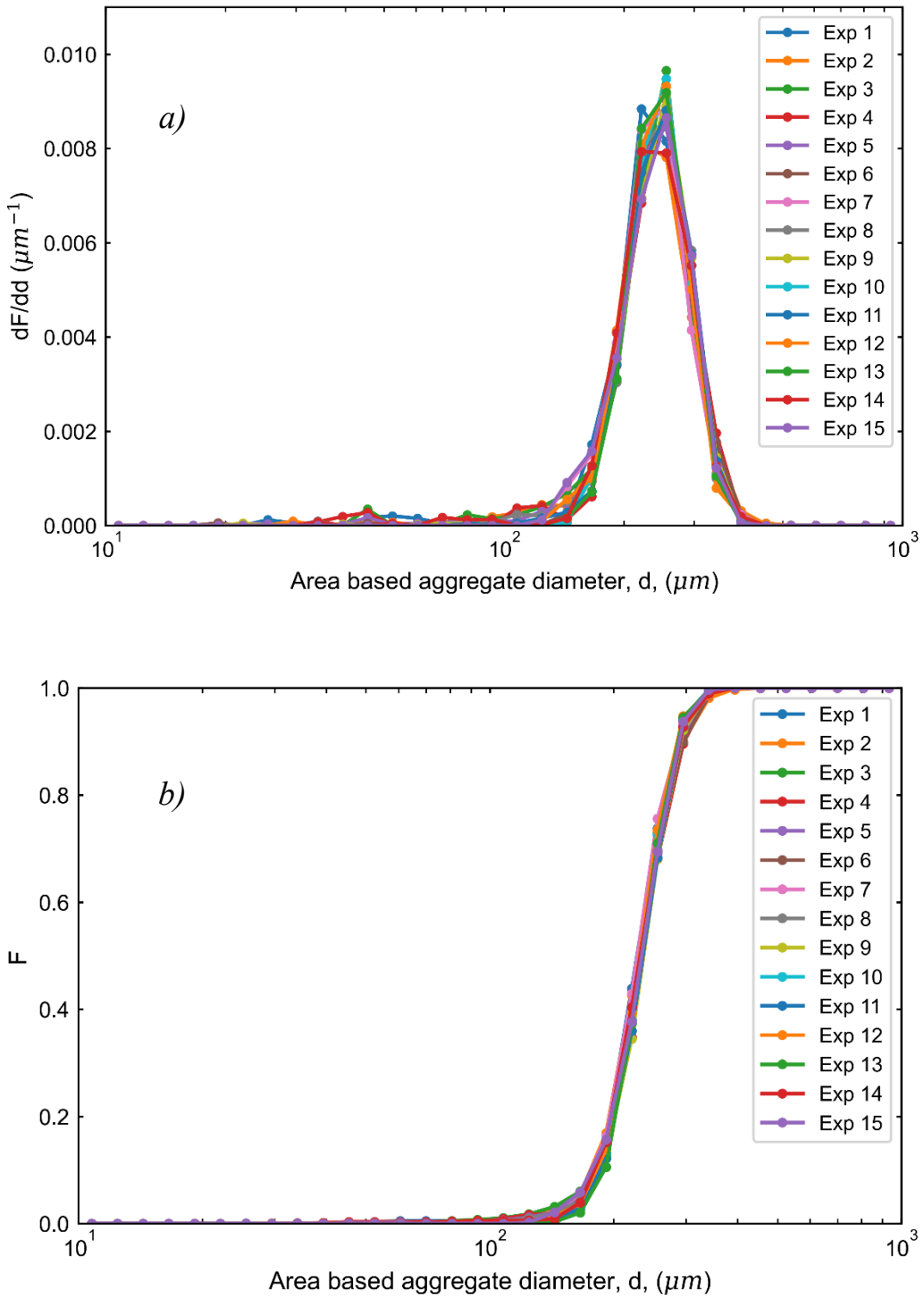

Figure 4-6 Aggregate (a) differential frequency size distribution (b) Cumulative frequency size distribution for 15 aggregation experiments at 17.6 s^{-1}. All data collected at t = 3h.

Table 4-5 Statistical parameters of the aggregates size distributions obtained in the aggregate experiments

Experiment	Number of Particles	d_{32}, µm	σ_d, µm	$d_{1,0}$, µm	$d10$, µm	$d50$, µm	$d90$, µm	d_{pf}	d_f
1	4585	261.8	45.1	245.9	194.2	243.9	301.9	1.26	2.51
2	10208	270.1	51.2	249.6	193.2	245.7	316.2	1.25	2.53
3	2667	264.7	46.6	248.5	194.7	250.3	305.1	1.25	2.53
4	2795	272.5	48.3	255.2	198.6	253.1	317.9	1.27	2.50
5	7384	269.9	48.0	252.4	197.8	250.3	314.1	1.26	2.50
6	6910	270.7	45.6	254.4	200.4	250.1	316.4	1.30	2.45
7	3998	263.0	45.2	246.5	192.4	242.0	302.8	1.37	2.35
8	6853	265.3	43.4	250.8	200.3	250.4	302.4	1.36	2.36
9	6715	269.3	43.4	254.8	200.7	253.4	310.5	1.40	2.30
10	5800	263.4	39.9	250.8	200.6	249.0	302.2	1.45	2.22
11	6436	267.3	42.2	253.6	201.1	251.9	308.4	1.35	2.38
12	2538	264.2	43.0	249.4	196.6	247.7	301.9	1.41	2.28
13	6247	264.5	39.2	252.3	204.5	248.8	305.2	1.47	2.20
14	2906	267.4	46.1	251.0	193.1	248.8	307.4	1.22	2.57
15	3879	264.8	44.0	249.9	191.4	250.5	305.2	1.24	2.54

The rearrangement of aggregates to more compact fractal structures is commonly observed when aggregates are exposed to shear. To assess the change in the structure it is necessary to measure the perimeter fractal dimension d_{pf}, which is extracted from the slope of the scatter graph showing the logarithm of perimeter vs logarithmic of the area using Equation (24). As shown in Figure 4-7, the data scatter around the regression line indicates that aggregates with the same area can have a different perimeter, suggesting they can have a slightly different structure and density for the same size. Small aggregates with areas below 10^3 pixels show a larger slope, thus a smaller perimeter fractal dimension. In other words, small aggregates could be more rounded and compacted than the larger ones within the same population. Although it is accepted that smaller flocs are more compact, the perimeter calculated for small aggregates is not as accurate as for large aggregates because of the limitation related to image resolution. Therefore, the inaccuracy of the

perimeter measurement also influences the perimeter fractal dimension when aggregates with a perimeter smaller than 10^2 pixels are assessed.

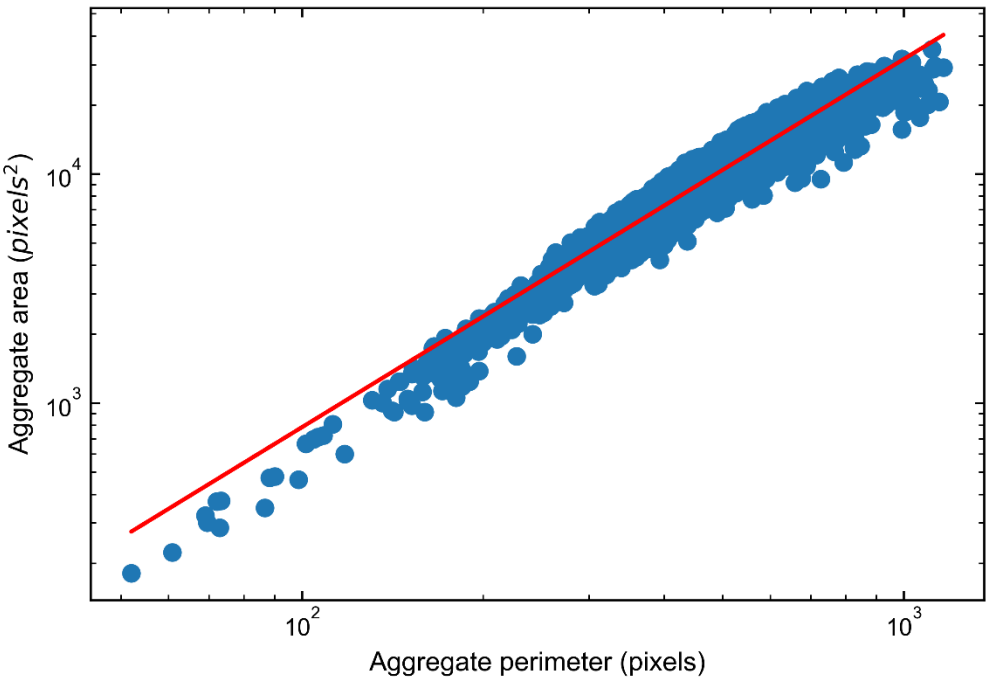

Figure 4-7 Relationship between the area and the perimeter for aggregates made at a shear rate of 17.6 s^{-1} obtained from image analysis of pictures of samples taken at steady state.

For the aggregation experiments, the average perimeter fractal dimension is 1.32. The average mass fractal dimension estimated using Ehrl's [93] correlation gives a value of 2.41, indicating that the aggregates are moderately compacted. The value of the mass fractal dimension is quite similar to the values found by other studying in orthokinetic aggregation [21,49,51,70,95,96].

4.3 Aggregate breakage

The aggregates were subjected to breakage by increasing the shear rate (from 17.6 s^{-1} to a specific higher value between 28.9 s^{-1} to 86.8 s^{-1}). The shear rate was kept constant until a new steady-state size was reached. Three repetitions per shear rate were done. Two image sequences of an aggregate break-up are shown in Figure 4-8, which were taken in the first minute of increasing the rotational velocity. The increase in shear rate deforms the aggregate until the breakage occurs.

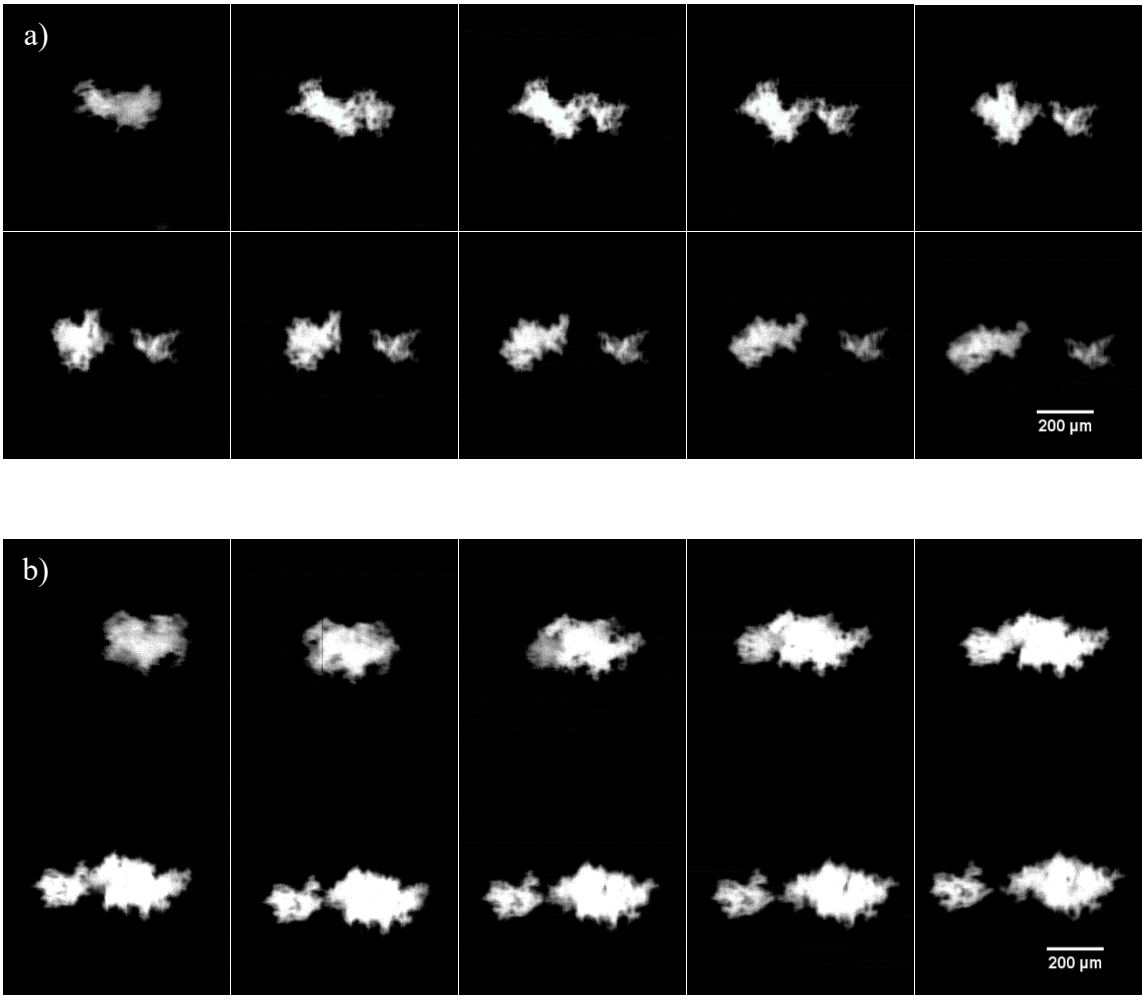

Figure 4-8 Sequences of images exhibiting an aggregate breaking into two fragments at 34.7s^{-1}. Both sequences were taken in the same experiment and show two different aggregates breaking.

Figure 4-9 shows the steady-state, number-based differential frequency distribution of the aggregate area-based diameter after breakage at different shear rates. It can be observed that, when the aggregate suspension is subjected to a higher shear rate, the aggregate size distribution shifts toward smaller aggregate sizes. The magnitude of this change increases as the shear rate increases, which agrees with previous studies regarding breakage [21,26,29,97].

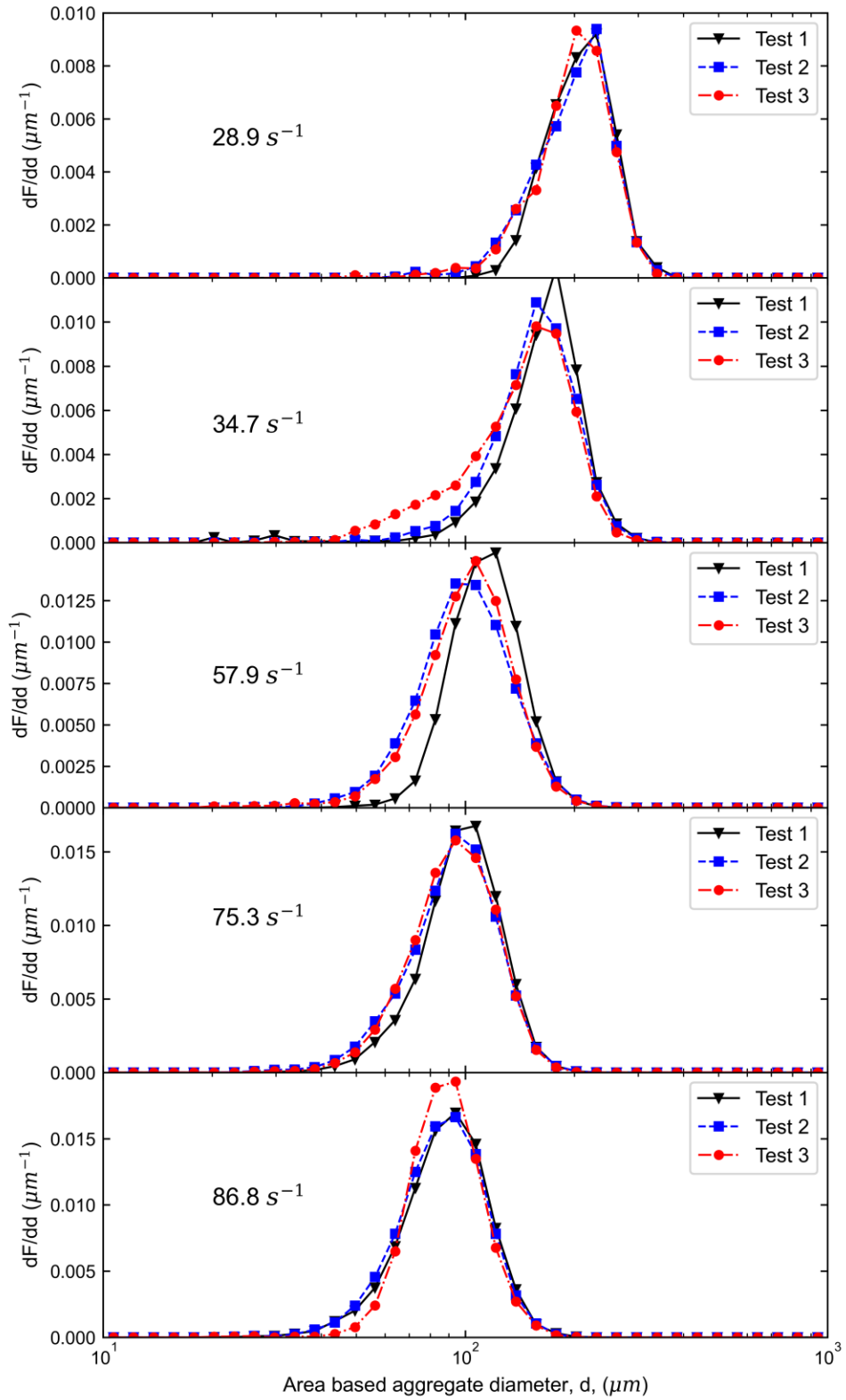

Figure 4-9 Steady state aggregate size distribution after breakup, at 5 different shear rates.

In the subsequent figures (Figure 4-10 to Figure 4-15) the breakage and reaggregation behaviour for different shear rates are shown. Three cases (28.9 s^{-1}, 34.7 s^{-1} and 57.9 s^{-1}) are chosen to illustrate the behaviour of the fragments after breakage. Number-based differential ASDs for the experiment performed at 28.9 s^{-1} at various time intervals are shown in Figure 4-10. It can be observed that the ASD has a rapid change to the left, i.e., smaller aggregates are observed as the breakage process proceeds. After 3 minutes at the increased shear rate, large aggregates were broken, and the presence of small aggregates was noticeable. Steady state is reached after 60 minutes, shown by the fact that the 90 minutes curve overlaps the 60 minutes curve. Reaggregation of the small fragments is noticeable in the 60 minutes curve. The small fragments with a size around 120 μm were present in the 30 minutes curve but were no longer visible in the 60 min curve; instead, there was an increment in the number of aggregates of size 180 μm.

Additional detailed information about the breakage at 28.9 s^{-1} is presented in Figure 4-11, where the changes in ASD at different time frames are shown. Positive values indicate the appearance of aggregates in the specific size bin, and negative values indicate the disappearance of aggregates. The major change in aggregate size was observed in the initial 3 minutes, where the aggregates between 250-300 μm were broken into fragments of around 180 μm. In the subsequent time frames, from 15 minutes to 30 minutes, the appearance of aggregates with a size around 200 μm was observed. In the time frame of 30 minutes to 60 minutes, it is noticeable that 120 μm aggregates disappear and the aggregates around 200 μm appear. This indicates the re-aggregation of small clusters into larger structures.

Steady-state was achieved after 60 minutes from the beginning of the breakage experiment and at that time the size distribution returns to a log-normal form. This was confirmed by measuring the size distribution after 90 minutes of the breakage.

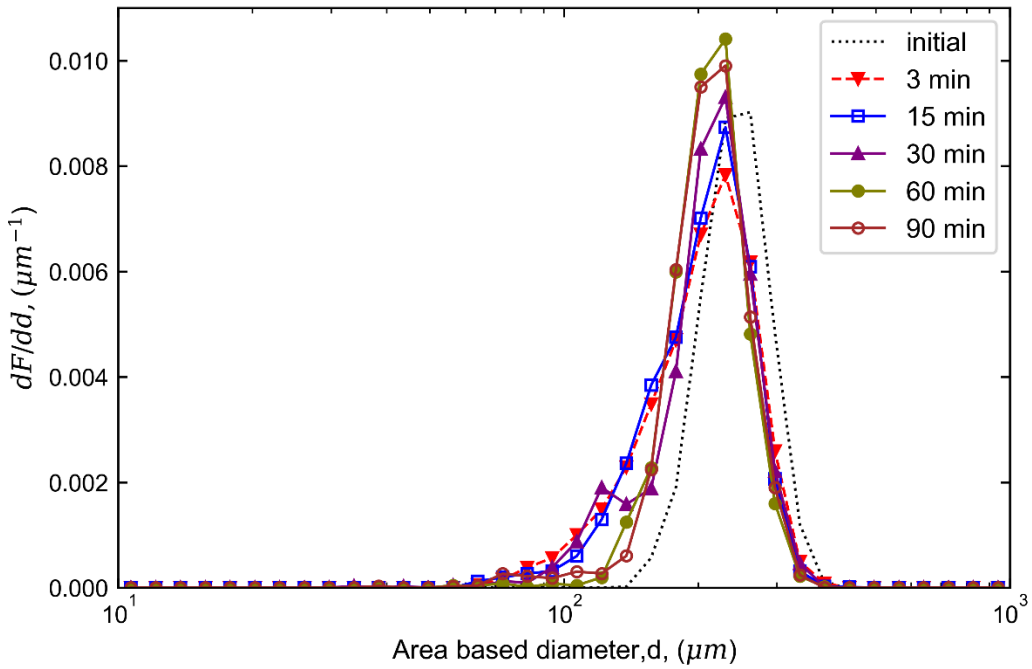

Figure 4-10 Number based differential frequency distribution for the experiment at 28.9s^{-1} at various times.

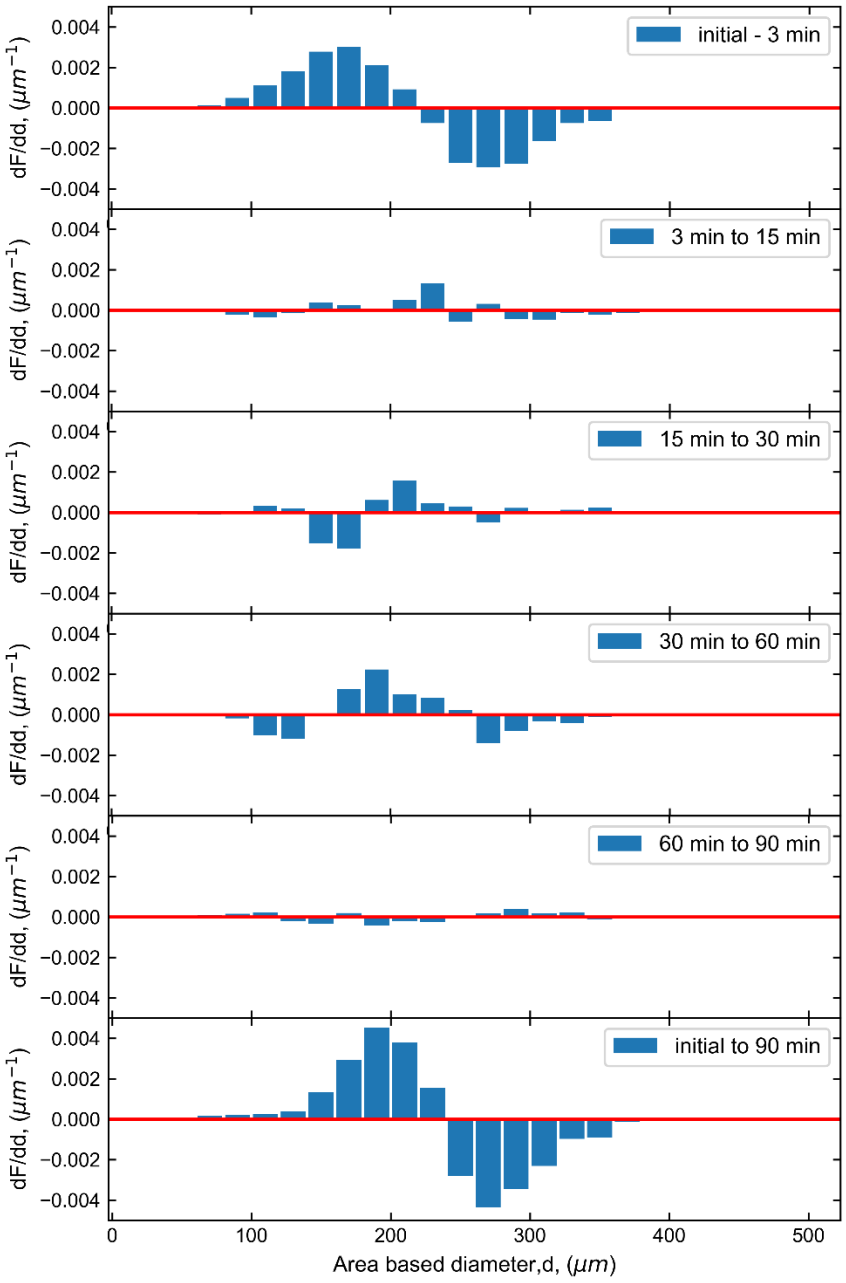

Figure 4-11 Change in the aggregate size distribution during breakage experiment at 28.9s^{-1}.

For the shearing test done at 34.7 s^{-1}, the ASD is shown in Figure 4-12. As was observed of shearing at 28.9 s^{-1}, the ASD shifts to the left, but shows a larger number of small fragments compared to the breakage experiment at 28.9 s^{-1}. After 3 minutes, the curve is skewed to the right, indicating the presence of small clusters.

Reaggregation of the small fragments is visible in the 30 minutes curve. The small fragments of around 90 µm were present in the 15 minutes curve, however these were no longer visible in the 30 minutes curve; instead, there was an increase in the number of aggregates of size around 200 µm. Steady state is reached after 120 minutes, demonstrated by the fact that the 150-minute curve crosses the 120-minute curve.

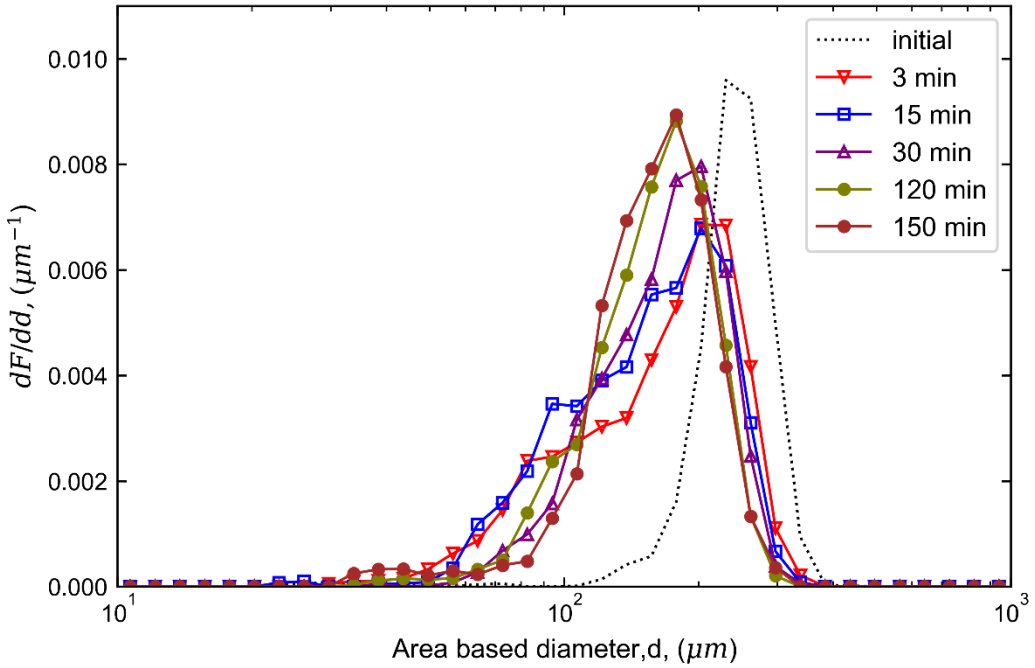

Figure 4-12 Number-based differential frequency distribution for the experiment at 34.7 s^{-1} at various times.

Figure 4-13 shows the comparison between the initial aggregate size distribution and that measured at different times. It can be clearly seen that most of the breakage occurs within the first 3 minutes, as the number of aggregates with sizes around 250 µm is reduced, and smaller fragments (between 90-190 µm) appear. As the breakage experiment progresses, it can be observed that aggregates smaller than 100 µm in diameter disappear and aggregates around 180 µm appear, indicating that re-aggregation of small clusters has occurred. After 2 hours, the ASD does not

change, suggesting the steady state was reached. Comparing the ASD from steady-state to the initial condition, it is observed that most of the broken aggregates are in the size range 240-300 µm and the new aggregates are in the size range of 160-200µm.

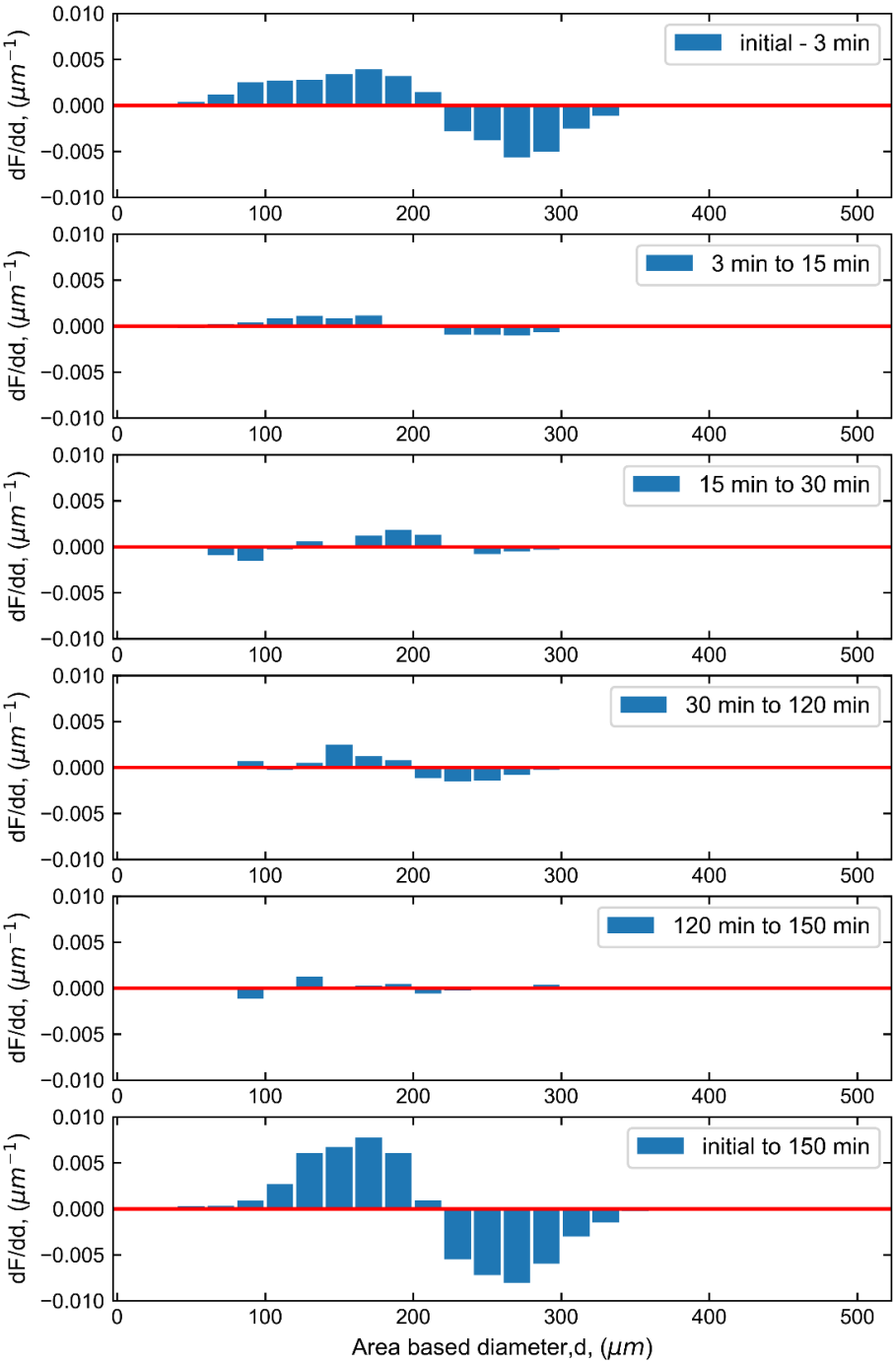

Figure 4-13 Change in the aggregate size distribution during breakage experiment at 34.7s^{-1}.

The ASDs for the breakage experiment conducted at 57.9 s^{-1}, collected at various times, are shown in Figure 4-14. After 3 minutes a rapid reduction in aggregate sizes is observable. After 10 minutes of shearing, the ASD does not show any change, i.e., the steady state has been reached.

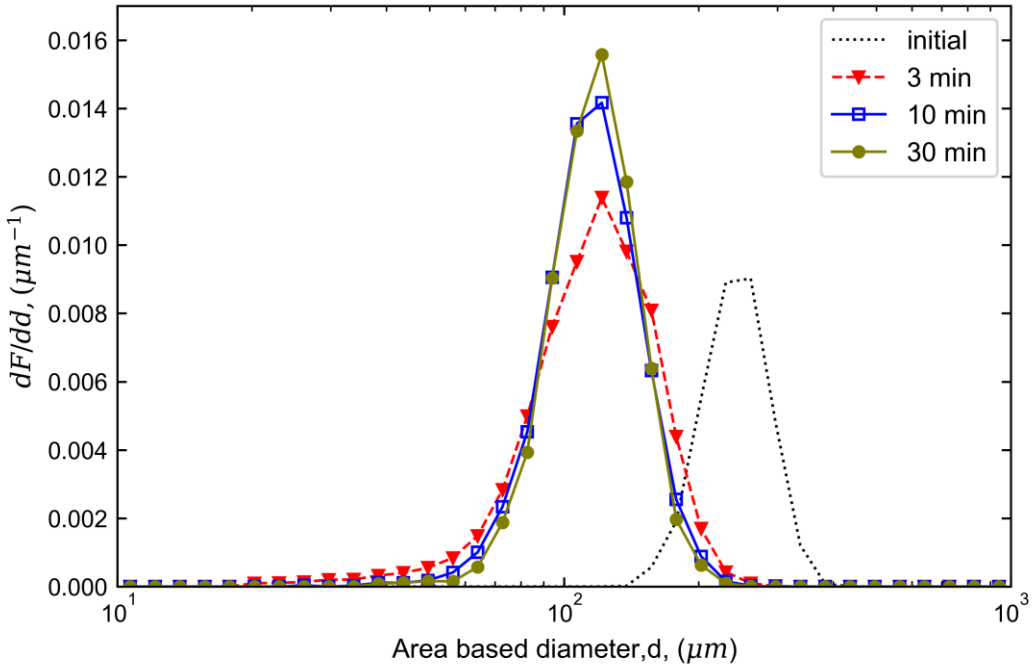

Figure 4-14 Number based differential frequency distribution for the experiment at 57.9s^{-1} at various times.

Figure 4-15 shows the comparison between the initial aggregate size distribution and that measured at different times for the breakage experiment conducted at 57.9 s^{-1}. As in the previous experiment, the breakage occurs rapidly, with the principal reduction in size observed within the first 3 minutes. In the comparison between 3 minutes and 10 minutes, only a small fraction of aggregates disappeared. After 10 minutes there is no change in the ASD, thus the steady state is reached. The same breakage behaviour was observed for the breakage at 75.3 s^{-1} and 86.8 s^{-1}, i.e., a rapid breakage mainly occurring within the first 3 minutes, with no reaggregation observable.

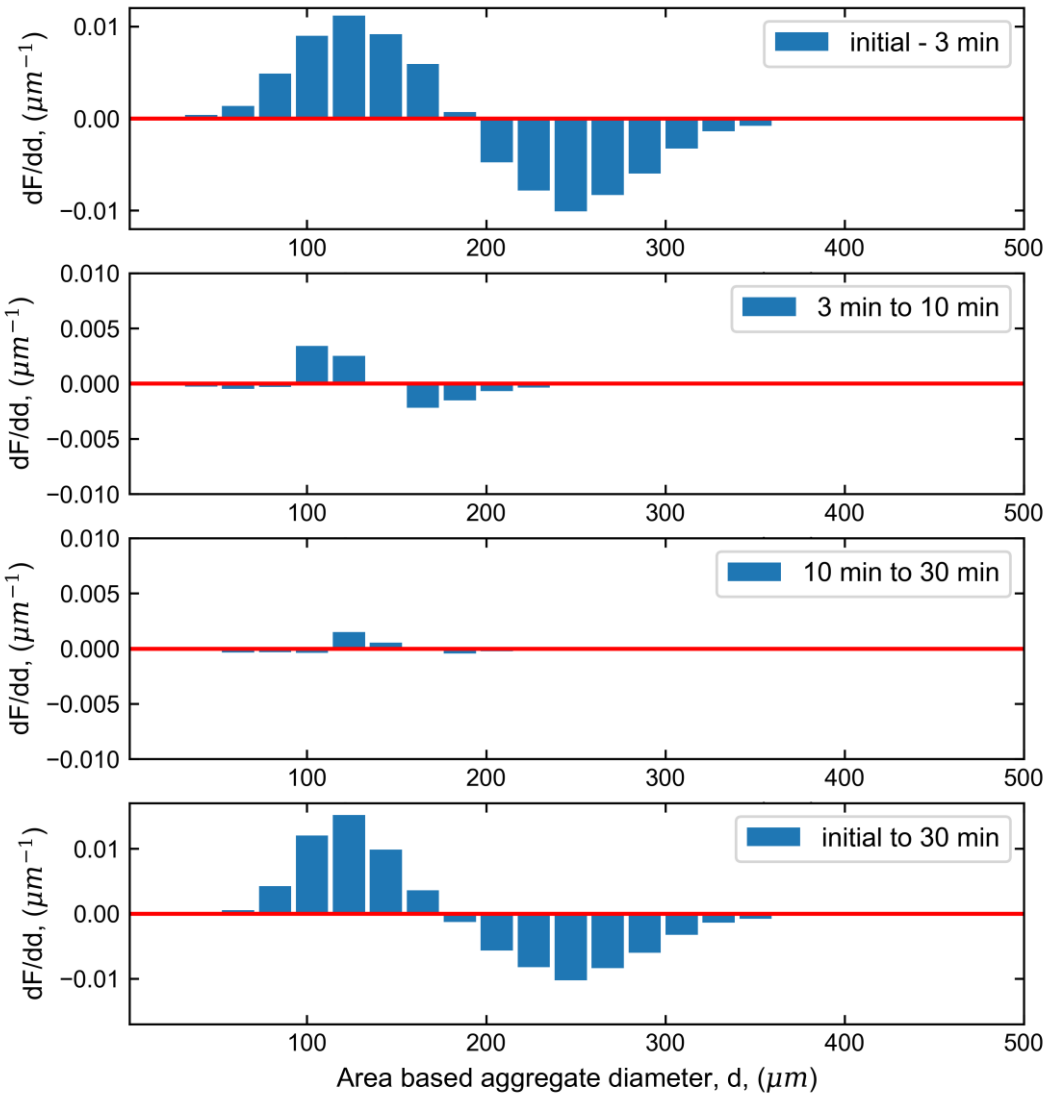

Figure 4-15 Change in the aggregate size distribution during breakage experiment at 57.9s^{-1}.

Two different aggregate behaviours were observed after increasing the shear rate. In the breakage experiment at 28.9 s^{-1} and 34.7 s^{-1}, which are the lower values of shear rate in these experiments, we can observe the re-aggregation of the fragments generated by rupture. For the higher shear rates studied, which are 57.9 s^{-1}, 75.3 s^{-1} and 86.8 s^{-1}, the aggregates reach the steady-state quickly with little re-aggregation of the small clusters.

Aggregate structure

The perimeter fractal dimension d_{pf} at steady state (after breakage) is shown in Figure 4-16. In all the breakage experiments conducted here, a decrease in the d_{pf} was observed. In other words, the aggregates were more compact after breakage. However, at the lowest value of shear rate (28.9 s^{-1}), the reduction in perimeter fractal dimension is minor, from an initial average d_{pf} of 1.32 to a value around 1.28. For the other shear rates, the perimeter fractal dimension is approximately constant, and its value is around 1.2. Using Ehrl's [93] relation for a d_{pf} of 1.2, the estimated mass fractal dimension is 2.6. Similar results were found by Harshe et al. [25] and Sonntag et al. [29], who observed an increase in the mass fractal dimension after breakage, indicating a re-arrangement of the particles in the aggregates after breakage.

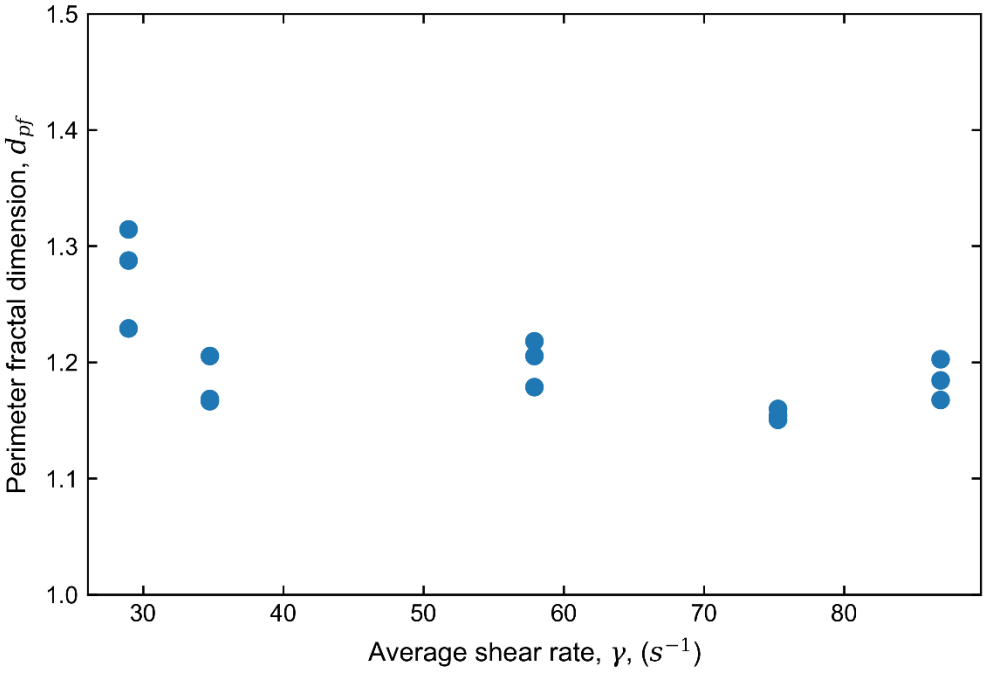

Figure 4-16 Perimeter fractal dimension of broken aggregates reaching steady state.

Scaling of aggregate size with shear rate

The dependency of the steady state aggregate size after breakage on the shear rate is compiled in Figure 4-17, in which the Sauter mean diameter, d_{32}, is plotted against the rupture shear rate. The Sauter mean diameter is defined as:

$$d_{32} = \frac{\sum n_i d_i^3}{\sum n_i d_i^2} \tag{26}$$

where n_i is the number of aggregates with a diameter of d_i. It is observed that the data follow a power-law relation with a scaling exponent of -0.69. This value agrees with studies for moderately concentrated systems in which breakage is not the dominant phenomenon. For example, Kroupa et al. [54] reported a scaling exponent of -0.65 with ϕ= 0.05 $^{v}/_{v}$ and Lachin et al. [81] obtained a scaling exponent of -0.66 with ϕ= 0.0045 $^{v}/_{v}$. The system studied here is not concentrated with ϕ= 0.0001 $^{v}/_{v}$; however, the breakage experiments at the low values of shear rate (28.9 s^{-1} and 34.7 s^{-1}) showed that the fragments re-aggregate until the system reached a new steady-state. The re-aggregation suggests that at the low values of shear rate the breakage is not the dominant phenomenon and aggregation takes a major place in the equilibrium between aggregation and breakage.

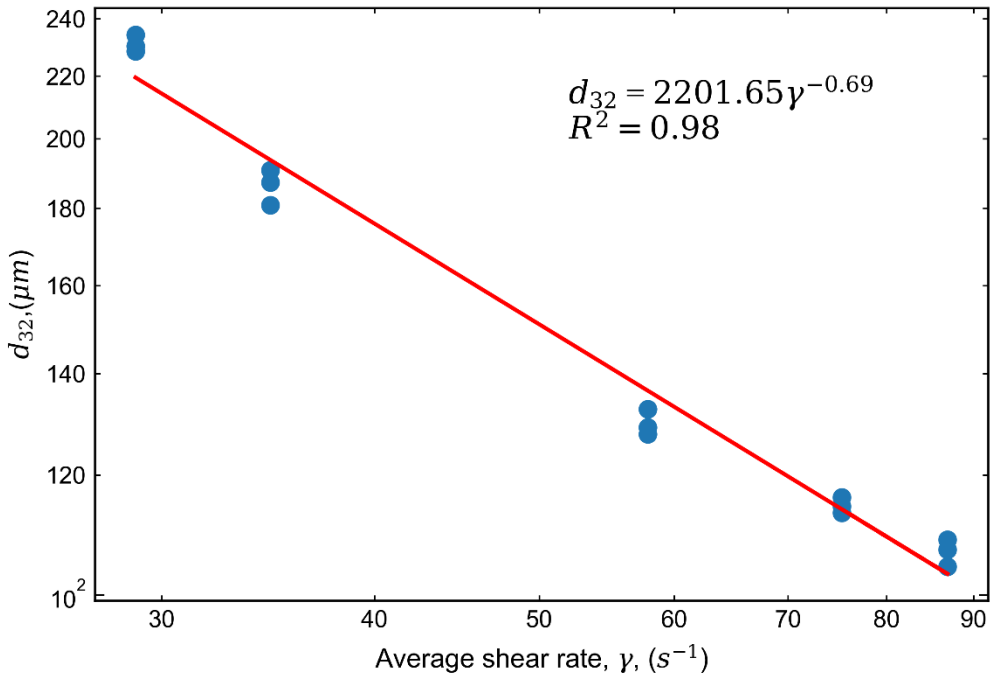

Figure 4-17 Scaling of the aggregate size with the average shear rate after aggregate breakage.

Figure 4-18 shows the scaling of the Sauter mean diameter at steady state with the average shear rate for the experiments in which no re-aggregation was observed, in other words, where breakage was the dominant phenomenon. The scaling exponent of the power-law relation gives a value of -0.48. This value is in good agreement with the literature for breakage in very dilute conditions ($\phi < 2.5 \times 10^{-5}$ $^{v}/_{v}$) where aggregation phenomena could be neglected [21,25,26,98].

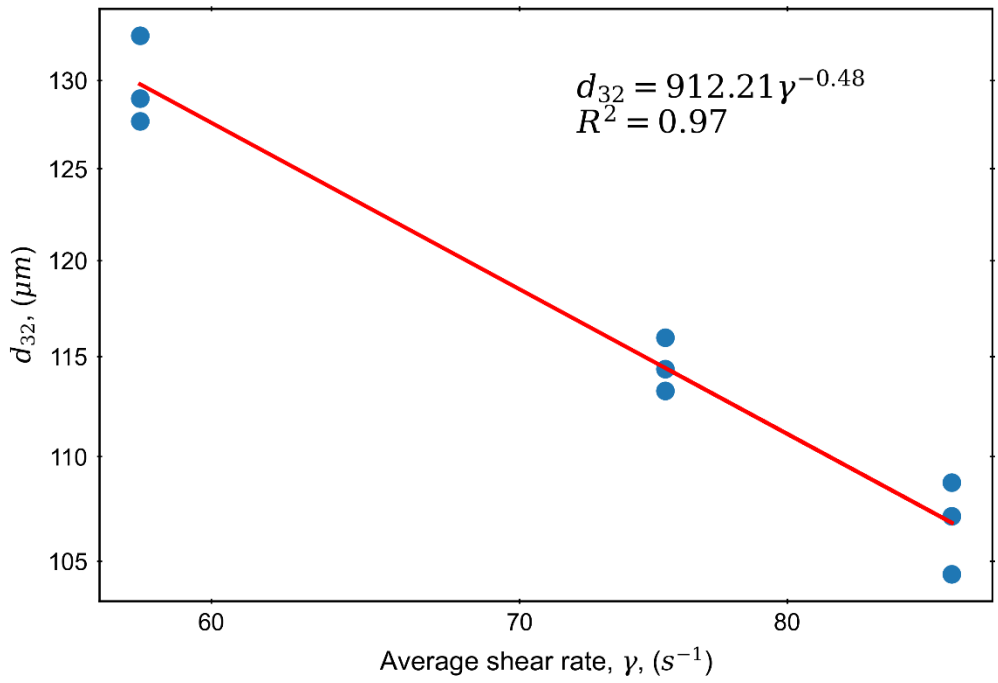

Figure 4-18 Scaling of the aggregate size with the average shear rate after breakage for the high shear rate experiments where breakage was the dominant phenomenon.

Aggregate cohesive force

The aggregate cohesive force can be calculated from the experiments where aggregation was not a dominating phenomenon, i.e., excluding the experiments at 28.9 s^{-1} and 34.7 s^{-1}, because in these experiments the final size results from breakage and re-aggregation and does not represent the size that the aggregate can maintain through its internal cohesive force.

The size of the aggregates is controlled by the maximum shear rate exerted on them. Since the shear rate in the Couette cell is nearly constant and the aggregates rotate in a position near the middle of the gap [99], we can assume that the shear rate exerted on the aggregates is the average shear rate. Using the Sauter mean of the area-based diameter, the aggregate cohesive force calculated with Equation (17) (assuming the aggregate is a sphere), is equal to 1.94 ± 0.11 nN and is independent of the aggregate size. This value is comparable with forces previously reported for breakage experiments of latex particles under conditions where aggregation is neglected, for

example, Kobayashi 2004 [16] reported an aggregate strength value of 2 nN, and Soos et al. 2008 [21] reported a value of 6.2 ±1.0 nN. The aggregate cohesive force is shown as a function of size in Figure 4-19. Experimental results from previous studies are also presented. Values of aggregate cohesive strength reported by other authors under similar conditions are between 0.1-10 nN [16,17,26]. The cohesive strength value found in this study is significantly lower than the rupture force for polymeric flocculants reported by Yeung and Pelton [57] and the rupture force for aggregation caused by precipitated salt as reported by Blaser [30]. The difference is mainly because their cohesive force values include the action of solid bridges.

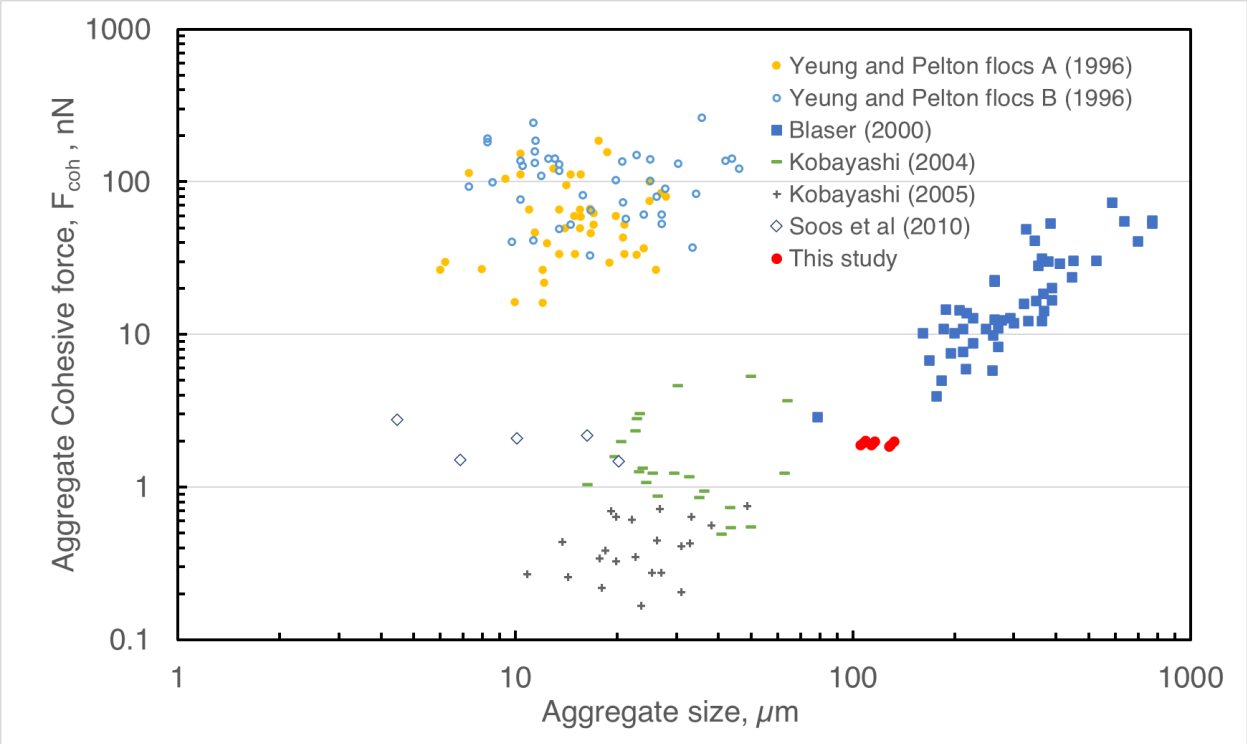

Figure 4-19 Aggregate cohesive strength as a function of size.

In the investigated system, the NaCl concentration (1.4M) is beyond the critical coagulation concentration, which is 1.1M. Therefore, the repulsive electrostatic force (double layer repulsion) is completely suppressed, and it can be assumed that the van der Waals force is the only attractive

force to be accounted for. Attractive van der Waals force between two latex microspheres can be calculated using Equation (7), with values for the Hamaker constant and separation distance obtained from the literature. A representative value of the Hamaker constant for latex particles in water, i.e., 1.37×10^{-20} J, was taken from Prieve and Russel [100]. A separation distance between particles is considered equivalent to three water layers: H = 0.75 nm, as proposed by Frappier et al. [15]. For this study, a particle diameter equal to 2 μm was provided by the particle supplier. Using these values, the resulting vdW force is calculated and is equal to 2 nN.

The theoretical vdW force between two primary particles is quite similar to the value for F_{coh} found in this study, suggesting that the aggregate cohesive strength is dictated by the attractive forces between two primary particles. A similar idea was proposed by Kobayashi [16], who observed the similarity between the values of F_{coh} and the pull-off force between two particles. Moreover, Potanin [53] suggested that the force required to break the aggregate is proportional to the force required to break a single chain of particles.

The scaling exponent given by $d_{32} \propto \gamma^{-0.48}$ and the nearly constant aggregate cohesive force obtained in this study agree with the results obtained by Potanin [53] for "soft aggregates". These aggregates are characterized by the fact that their primary particles interact mainly through central forces and the effect of tangential forces is minimal. Thus, according to Potanin's model [53], the particles can be easily aligned to form a straight chain since there is no sliding friction or resistance to slide between particles. Under stress, only one chain of particles is in maximum tension and resists stretching at the same time. When the hydrodynamic force is large enough to break the chain, another chain of particles will be straightened, stretched, and broken. Under a constant value of F_{hyd}, this process will continue until eventually all the chains holding the aggregate fragments together are broken.

Chapter 5 Conclusions and Recommendations

5.1 Conclusions

The present research investigated experimentally the breakup of aggregates in laminar Couette flow using a non-invasive image analysis technique. The aggregate area-based diameter and perimeter were extracted from images to analyze the changes in size and structure of aggregates after exposure to a controlled shear rate.

The main conclusions of this project can be summarized as:

1. The breakage experiments of aggregates of latex particles were carried out in laminar Couette flow. Aggregates were produced at a shear rate of 17.6 s^{-1}, then the shear rate was increased within the laminar Couette flow regime to induce the breakage. Two situations were observed in the breakage experiments. At low values of shear rate, both breakage and re-aggregation mechanisms play significant roles in the steady state aggregate size distribution. At high values of shear rate, breakage is the dominant mechanism and aggregation can be neglected.
2. An image analysis script was developed to capture the aggregate size and perimeter from in situ imaging. Image analysis of the in situ images taken from the Couette cell device was a useful tool to study the breakup of aggregates without extracting the samples and analyzing them off-line (e.g., through microscopy).
3. From the latter experiments, where re-aggregation was not observed, we can estimate the aggregate cohesive force. which was calculated assuming the aggregate to be a sphere. The cohesive force was found to be independent of the aggregate size, with a value equal to 1.94 ±0.11 nN. This value is similar to the theoretical interaction force between two

particles, which is about 2.0 nN. These numbers suggest that, for this system, the aggregate cohesive force is dictated by the attractive force between two primary particles.

The key findings of this project are:

1. Under shear flow, the aggregates are subjected to rotation and deformation. The deformation causes the breakage and restructuring observed here. As the shear rate was increased, the aggregates became smaller and more compact. The aggregate area-based diameter and perimeter fractal dimension decrease in all the cases, meaning that the phenomenon of breakage and restructuring were present in all the experiments.
2. The results showed two different situations; at lower shear rates, aggregates reduced their size slightly and released small fragments. The fragments re-aggregate and a new steady-state size distribution is reached. In other words, after breakage, the small fragments were not in equilibrium and aggregation was dominant; consequently, fragments tended to re-aggregate until a new balance between aggregation and rupture was reached. For the higher shear rates, breakage occurs rapidly, and the fragments originated by the breakup did not re-aggregate.
3. It was found that the values of the aggregate Sauter mean diameter at steady state after breakage follow a power-law scaling with the average shear rate: $d_{32} \propto \gamma^{-p}$. The scaling exponent of the aggregate size with the shear rate showed good agreement with the data published in the literature for systems where both aggregation and breakage mechanisms play a significant role. The scaling exponent also was calculated for the experiments in which only breakage was observed and was found to be -0.48. This value is in good agreement with the scaling exponents found in the literature for breakage experiments in very dilute conditions where aggregation or reaggregation can be neglected.

4. The aggregate structure was characterized using the perimeter fractal dimension (d_{pf}), which was obtained from image analysis. The d_{pf} resulting from a breakage experiment is smaller than the initial average d_{pf} before the breakup. For breakage experiments at shear rates greater than 34.7 s^{-1}, d_{pf} also decreases compared with the initial value but remains almost stable at around 1.2. In these cases, the estimated mass fractal dimension is equal to 2.6, indicating that the breakage is accompanied by restructuring.
5. Regarding the experimental method, in situ image analysis showed to be a highly effective option for measuring morphological parameters of aggregates. The validation of the image analysis method shows good agreement with microscopy (in static conditions), despite the motion of the aggregates in the Couette cell.

5.2 Recommendations for future work

One finding in this study is the comparison between the aggregate cohesive strength and the inter-particle attractive force between two primary particles, which theoretically depends on the particle size. In order to confirm this relation, breakage experiments should be done using latex microspheres of different diameters. The cohesive aggregate strength should be evaluated in conditions where the impact of re-aggregation could be neglected.

There are just a few studies regarding the cohesive strength of aggregates made with polymers, which are quite common in industrial aggregation. The understanding of the cohesive force produced by polymers is limited. Breakage experiments with polymers should be performed using the setup developed here. The results will help to improve the understanding of the rupture of industrial wastewater aggregates.

The aggregate mean size was found to have a direct relation to the shear rate. This relationship may not apply in different flow regimes. Additional experiments should be done outside the laminar regime. It is recommended to perform more experiments with higher shear rates than those investigated in this study. A wider range of shear rates can help to confirm and extend the results presented here.

In this study, the aggregate cohesive strength was found to be constant and independent of the aggregate size for aggregates produced through orthokinetic aggregation. However, the experimental results obtained by Harshe et al. [25] suggest that open aggregates produced under diffusion-limited cluster aggregation (DLCA) may have a cohesive strength dependent on the size of the aggregate, because the scaling exponent was found to be -0.35. This is in disagreement with the results obtained here. Breakage experiments to quantify the cohesive strength of DLCA aggregates need to be performed.

Further research is needed on the cohesive force of industrial aggregates, which are different from the aggregates of latex particles used in this study. The primary particles of industrial aggregates are different in terms of size, morphology and composition depending on the type of industrial system. This should be done by performing breakage experiments using industrial samples. The resulting information would allow one to use the cohesive force in the design and optimization of industrial thickeners/settlers.

Some authors [59] suggest that the aggregate cohesive force is a function of the shear rate at which the aggregate was formed. This can be validated with the setup designed in this project, by testing different shear rates during the aggregation step and then performing breakage experiments. In the case where the optimum shear rate for the maximum aggregate cohesive strength is found, this value would be of vital importance in the design of industrial scale flocculators.

The aggregate structure was characterized by the perimeter fractal dimension extracted from the image analysis. The d_{pf} was used to estimate the mass fractal dimension using the Ehrl et al. relation [93], which was developed using simulated aggregates. This equation needs to be validated through settling experiments of aggregates, comparing the values of the perimeter fractal dimension with the mass fractal dimension calculated with the settling velocity. The latter can be done using the method described by Vaezi et al. [49].

References

[1] J. Gregory, & Charles, R.R. O'melia, Fundamentals of flocculation, Critical Reviews in Environmental Science and Technology. 19 (1989) 185–230. https://doi.org/10.1080/10643388909388365.

[2] J.N. Israelachvili, Intermolecular and Surface Forces: Third Edition, Elsevier Inc., 2011. https://doi.org/10.1016/C2011-0-05119-0.

[3] J. Masliyah, Z. Zhou, Z. Xu, J. Czarnecki, H. Hamza, Understanding water-based bitumen extraction from athabasca oil sands, Canadian Journal of Chemical Engineering. 82 (2004) 628–654. https://doi.org/10.1002/cjce.5450820403.

[4] J.H. Masliyah, J. Czarnecki, Z. Xu, Handbook on Theory and Practice of Bitumen Recovery from Athabasca Oil Sands Volume I, Kingsley publishing services: Cochrane, AB, 2011. https://doi.org/10.1017/CBO9781107415324.004.

[5] Z.Xu. P. Gosselin, S. E. Hrudey, M. A. Naeth, A. Plourde, R. Therrien, G. Van Der Kraak, Environmental and health impacts of canada's oil sands industry, (2010). www.rsc-src.ca. (accessed November 25, 2021).

[6] Alberta Energy Regulator, State of Fluid Tailings Management for Mineable Oil Sands, 2019, (2020) 83. www.aer.ca (accessed April 5, 2020).

[7] D.R.L. Vedoy, J.B.P. Soares, Water-soluble polymers for oil sands tailing treatment: A Review, Canadian Journal of Chemical Engineering. 93 (2015) 888–904. https://doi.org/10.1002/cjce.22129.

[8] BGC Engineering Inc., Oil Sands Tailings Technology Review, Oil Sands Research and Information Network. OSRIN Repo (2010) OSRIN Report No. TR-1. 136 pp. https://doi.org/OSRIN Report No. TR-1.

[9] R. Neelakantan, F. Vaezi G., R.S. Sanders, Effect of shear on the yield stress and aggregate structure of flocculant-dosed, concentrated kaolinite suspensions, Minerals Engineering. 123 (2018) 95–103. https://doi.org/10.1016/j.mineng.2018.03.016.

[10] M. Sillanpää, M.C. Ncibi, A. Matilainen, M. Vepsäläinen, Removal of natural organic matter in drinking water treatment by coagulation: A comprehensive review, Chemosphere. 190 (2018) 54–71. https://doi.org/10.1016/j.chemosphere.2017.09.113.

[11] B. Bolto, J. Gregory, Organic polyelectrolytes in water treatment, Water Research. 41 (2007) 2301–2324. https://doi.org/10.1016/j.watres.2007.03.012.

[12] A. Matilainen, M. Vepsäläinen, M. Sillanpää, Natural organic matter removal by coagulation during drinking water treatment: A review, (2010). https://doi.org/10.1016/j.cis.2010.06.007.

[13] J. Zawala, T. Dabros, H.A. Hamza, Settling properties of aggregates in paraffinic froth treatment, Energy and Fuels. 26 (2012) 5775–5781. https://doi.org/10.1021/ef300885t.

[14] Y. Long, T. Dabros, H. Hamza, Structure of water/solids/asphaltenes aggregates and effect of mixing temperature on settling rate in solvent-diluted bitumen, Fuel. 83 (2004) 823–832. https://doi.org/10.1016/j.fuel.2003.10.026.

[15] G. Frappier, B.S. Lartiges, S. Skali-Lami, Floc cohesive force in reversible aggregation: A couette laminar flow investigation, Langmuir. 26 (2010) 10475–10488. https://doi.org/10.1021/la9046947.

[16] M. Kobayashi, Breakup and strength of polystyrene latex flocs subjected to a converging flow, Colloids and Surfaces A: Physicochemical and Engineering Aspects. 235 (2004) 73–78. https://doi.org/10.1016/j.colsurfa.2004.01.008.

[17] M. Kobayashi, Strength of natural soil flocs, Water Research. 39 (2005) 3273–3278. https://doi.org/10.1016/j.watres.2005.05.037.

[18] P. Bubakova, M. Pivokonsky, P. Filip, Effect of shear rate on aggregate size and structure in the process of aggregation and at steady state, Powder Technology. (2013). https://doi.org/10.1016/j.powtec.2012.11.014.

[19] M. Kobayashi, Breakup of fractal floes in a turbulent flow, Langmuir. 15 (1999) 4351–4356. https://doi.org/10.1021/la980763o.

[20] M. Vlieghe, C. Coufort-Saudejaud, C. Frances, A. Liné, In situ characterization of floc morphology by image analysis in a turbulent Taylor-Couette reactor, AIChE Journal. 60 (2014) 2389–2403. https://doi.org/10.1002/aic.14431.

[21] M. Soos, A.S. Moussa, L. Ehrl, J. Sefcik, H. Wu, M. Morbidelli, Effect of shear rate on aggregate size and morphology investigated under turbulent conditions in stirred tank, Journal of Colloid and Interface Science. 319 (2008) 577–589. https://doi.org/10.1016/j.jcis.2007.12.005.

[22] L. Guérin, C. Coufort-Saudejaud, A. Liné, C. Frances, Dynamics of aggregate size and shape properties under sequenced flocculation in a turbulent Taylor-Couette reactor, Journal of Colloid and Interface Science. 491 (2017) 167–178. https://doi.org/10.1016/j.jcis.2016.12.042.

[23] L. Ehrl, M. Soos, M. Morbidelli, Dependence of aggregate strength, structure, and light scattering properties on primary particle size under turbulent conditions in stirred tank, Langmuir. 24 (2008) 3070–3081. https://doi.org/10.1021/la7032302.

[24] PARKER DS, KAUFMAN WJ, JENKINS D, Floc breakup in turbulent flocculation processes, ASCE J Sanit Eng Div. 98 (1972) 79–99. https://doi.org/10.1061/jsedai.0001389.

[25] Y.M. Harshe, M. Lattuada, M. Soos, Experimental and modeling study of breakage and restructuring of open and dense colloidal aggregates, Langmuir. 27 (2011) 5739–5752. https://doi.org/10.1021/la1046589.

[26] M. Soos, L. Ehrl, M.U. Bäbler, M. Morbidelli, Aggregate breakup in a contracting nozzle, Langmuir. 26 (2010) 10–18. https://doi.org/10.1021/la903982n.

[27] D. Saha, M.U. Babler, M. Holzner, M. Soos, B. Lüthi, A. Liberzon, W. Kinzelbach, Breakup of Finite-Size Colloidal Aggregates in Turbulent Flow Investigated by Three-Dimensional (3D) Particle Tracking Velocimetry, Langmuir. 32 (2016) 55–65. https://doi.org/10.1021/acs.langmuir.5b03804.

[28] D. Saha, M. Soos, B. Lüthi, M. Holzner, A. Liberzon, M.U. Babler, W. Kinzelbach, Experimental characterization of breakage rate of colloidal aggregates in

axisymmetric extensional flow, Langmuir. 30 (2014) 14385–14395. https://doi.org/10.1021/la502686b.

[29] R.C. Sonntag, W.B. Russel, Structure and breakup of flocs subjected to fluid stresses. I. Shear experiments, Journal of Colloid And Interface Science. 113 (1986) 399–413. https://doi.org/10.1016/0021-9797(86)90175-X.

[30] S. Blaser, Flocs in shear and strain flows, Journal of Colloid and Interface Science. 225 (2000) 273–284. https://doi.org/10.1006/jcis.1999.6671.

[31] A. Saxena, J.S. Kroll-Rabotin, R.S. Sanders, Numerical investigation of the respective roles of cohesive and hydrodynamic forces in aggregate restructuring under shear flow, Journal of Colloid and Interface Science. 608 (2022) 355–365. https://doi.org/10.1016/j.jcis.2021.08.208.

[32] J. Guam, T.D. Vvaite, R. Amal, Rapid structure characterization of bacterial aggregates, Environmental Science and Technology. 32 (1998) 3735–3742. https://doi.org/10.1021/es980387u.

[33] D.F. Lawler, Particle size distributions in treatment processes: theory and practice, Water Science and Technology. 36 (1997) 15–23. https://doi.org/10.2166/wst.1997.0075.

[34] J. Bratby, Coagulation and flocculation in water and wastewater treatment, Water 21. (2006) 25–27. https://doi.org/10.2166/9781780407500.

[35] D.N. Thomas, S.J. Judd, N. Fawcett, Flocculation modelling: A review, Pergamon, 1999. https://doi.org/10.1016/S0043-1354(98)00392-3.

[36] T. Serra, J. Colomer, X. Casamitjana, Aggregation and breakup of particles in a shear flow, Journal of Colloid and Interface Science. 187 (1997) 466–473. https://doi.org/10.1006/jcis.1996.4710.

[37] S. Lazzari, L. Nicoud, B. Jaquet, M. Lattuada, M. Morbidelli, Fractal-like structures in colloid science, Advances in Colloid and Interface Science. 235 (2016) 1–13. https://doi.org/10.1016/j.cis.2016.05.002.

[38] M.Y. Lin, H.M. Lindsay, D.A. Weitz, R.C. Ball, R. Klein, P. Meakin, Universality in colloid aggregation, Nature. 339 (1989) 360–362. https://doi.org/10.1038/339360a0.

[39] P.J. Lu, D.A. Weitz, Colloidal particles: Crystals, glasses, and gels, Annual Review of Condensed Matter Physics. 4 (2013) 217–233. https://doi.org/10.1146/annurev-conmatphys-030212-184213.

[40] S. Tang, J.M. Preece, C.M. McFarlane, Z. Zhang, Fractal morphology and breakage of DLCA and RLCA aggregates, Journal of Colloid and Interface Science. 221 (2000) 114–123. https://doi.org/10.1006/jcis.1999.6565.

[41] N. Tambo, Y. Watanabe, Physical characteristics of flocs-I. The floc density function and aluminium floc, Water Research. (1979). https://doi.org/10.1016/0043-1354(79)90033-2.

[42] C.P. Johnson, X. Li, B.E. Logan, Settling velocities of fractal aggregates, Environmental Science and Technology. 30 (1996) 1911–1918. https://doi.org/10.1021/es950604g.

[43] C. Selomulya, G. Bushell, R. Amal, T.D. Waite, Understanding the role of restructuring in flocculation: The application of a population balance model, Chemical Engineering Science. (2003). https://doi.org/10.1016/S0009-2509(02)00523-7.

[44] J. Gregory, The density of particle aggregates, Water Science and Technology. 36 (1997) 1–13. https://doi.org/10.2166/wst.1997.0073.

[45] J.C. Berg, An introduction to interfaces and colloids: The bridge to nanoscience, 2009. https://doi.org/10.1142/7579.

[46] M. Elimelech, J. Gregory, X. Jia, R.A. Williams, Surface interaction potentials, in: Particle Deposition & Aggregation, Butterworth-Heinemann, 1995: pp. 33–67. https://doi.org/10.1016/b978-075067024-1/50003-0.

[47] T. Serra, J. Colomer, B.E. Logan, Efficiency of different shear devices on flocculation, Water Research. (2008). https://doi.org/10.1016/j.watres.2007.08.027.

[48] C. Coufort, D. Bouyer, A. Liné, Flocculation related to local hydrodynamics in a Taylor-Couette reactor and in a jar, in: Chemical Engineering Science, 2005: pp. 2179–2192. https://doi.org/10.1016/j.ces.2004.10.038.

[49] F. Vaezi G., R.S. Sanders, J.H. Masliyah, Flocculation kinetics and aggregate structure of kaolinite mixtures in laminar tube flow, Journal of Colloid and Interface Science. 355 (2011) 96–105. https://doi.org/10.1016/j.jcis.2010.11.068.

[50] C. Selomulya, R. Amal, G. Bushell, T.D. Waite, Evidence of shear rate dependence on restructuring and breakup of latex aggregates, Journal of Colloid and Interface Science. (2001). https://doi.org/10.1006/jcis.2000.7372.

[51] T. Serra, X. Casamitjana, Structure of the aggregates during the process of aggregation and breakup under a shear flow, Journal of Colloid and Interface Science. (1998). https://doi.org/10.1006/jcis.1998.5714.

[52] V. Oles, Shear-induced aggregation and breakup of polystyrene latex particles, Journal of Colloid And Interface Science. 154 (1992) 351–358. https://doi.org/10.1016/0021-9797(92)90149-G.

[53] A.A. Potanin, On the computer simulation of the deformation and breakup of colloidal aggregates in shear flow, Journal of Colloid And Interface Science. 157 (1993) 399–410. https://doi.org/10.1006/jcis.1993.1202.

[54] M. Kroupa, M. Vonka, M. Soos, J. Kosek, Size and Structure of Clusters Formed by Shear Induced Coagulation: Modeling by Discrete Element Method, Langmuir. 31 (2015) 7727–7737. https://doi.org/10.1021/acs.langmuir.5b01046.

[55] L. Wang, R.D. Vigil, R.O. Fox, CFD simulation of shear-induced aggregation and breakage in turbulent Taylor-Couette flow, Journal of Colloid and Interface Science. 285 (2005) 167–178. https://doi.org/10.1016/j.jcis.2004.10.075.

[56] N. Tambo, H. Hozumi, Physical characteristics of flocs-II. Strength of floc, Water Research. (1979). https://doi.org/10.1016/0043-1354(79)90034-4.

[57] A.K.C.C. Yeung, R. Pelton, Micromechanics: A new approach to studying the strength and breakup of flocs, Journal of Colloid and Interface Science. 184 (1996) 579–585. https://doi.org/10.1006/jcis.1996.0654.

[58] P.T. Spicer, S.E. Pratsinis, J. Raper, R. Amal, G. Bushell, G. Meesters, Effect of shear schedule on particle size, density, and structure during flocculation in stirred tanks, Powder Technology. (1998). https://doi.org/10.1016/S0032-5910(97)03389-5.

[59] A. Yeung, A. Gibbs, R. Pelton, Effect of Shear on the Strength of Polymer-Induced Flocs, Journal of Colloid and Interface Science. 196 (1997) 113–115. https://doi.org/10.1006/JCIS.1997.5140.

[60] Y. Adachi, C. Di, F. Xiao, M. Kobayashi, Size, orientation, and strength of Na-montmorillonite flocs flowing in a laminar shear flow, Colloid and Polymer Science. 297 (2019) 979–987. https://doi.org/10.1007/s00396-019-04532-3.

[61] P. Jarvis, B. Jefferson, J. Gregory, S.A. Parsons, A review of floc strength and breakage, Water Research. 39 (2005) 3121–3137. https://doi.org/10.1016/j.watres.2005.05.022.

[62] A. Zaccone, M. Soos, M. Lattuada, H. Wu, M.U. Bäbler, M. Morbidelli, Breakup of dense colloidal aggregates under hydrodynamic stresses, Physical Review E - Statistical, Nonlinear, and Soft Matter Physics. 79 (2009). https://doi.org/10.1103/PhysRevE.79.061401.

[63] S. Blaser, Forces on the surface of small ellipsoidal particles immersed in a linear flow field, 2002. https://doi.org/10.1016/S0009-2509(01)00389-X.

[64] M. Boller, S. Blaser, Particles under stress, Water Science and Technology. 37 (1998) 9–29. https://doi.org/10.1016/S0273-1223(98)00303-5.

[65] C. Coufort, A. Liné, Forces on spherical particles in terms of upstream flow characteristics, 2003. https://doi.org/10.1205/026387603770866399.

[66] Y.M. Harshe, M. Lattuada, Universal Breakup of Colloidal Clusters in Simple Shear Flow, Journal of Physical Chemistry B. 120 (2016) 7244–7252. https://doi.org/10.1021/acs.jpcb.6b03220.

[67] K. Horii, R. Yamada, S. Harada, Strength Deterioration of Nonfractal Particle Aggregates in Simple Shear Flow, Langmuir. 31 (2015) 7909–7918. https://doi.org/10.1021/acs.langmuir.5b00197.

[68] B.O. Conchuir, Y.M. Harshe, M. Lattuada, A. Zaccone, Analytical model of fractal aggregate stability and restructuring in shear flows, Industrial and Engineering Chemistry Research. 53 (2014) 9109–9119. https://doi.org/10.1021/ie4032605.

[69] A. Saxena, Aggregate Evolution in Shear Flow: Numerical Investigation of the Role of Cohesive and Hydrodynamic Forces, 2021. https://doi.org/10.7939/R3-8JQ3-HA80.

[70] P.T. Spicer, S.E. Pratsinis, Shear-induced flocculation: The evolution of floc structure and the shape of the size distribution at steady state, Water Research. (1996). https://doi.org/10.1016/0043-1354(95)00253-7.

[71] P.T. Spicer, W. Keller, S.E. Pratsinis, The effect of impeller type on floc size and structure during shear-induced flocculation, 1996. https://doi.org/10.1006/jcis.1996.0601.

[72] A.S. Moussa, M. Soos, J. Sefcik, M. Morbidelli, Effect of solid volume fraction on aggregation and breakage in colloidal suspensions in batch and continuous stirred tanks, Langmuir. 23 (2007) 1664–1673. https://doi.org/10.1021/la062138m.

[73] P.T.L. Koh, J.R.G. Andrews, P.H.T. Uhlherr, Flocculation in stired tanks, Chemical Engineering Science. (1984). https://doi.org/10.1016/0009-2509(84)87005-0.

[74] X. Shen, J.P.Y. Maa, Floc size distributions of suspended kaolinite in an advection transport dominated tank: measurements and modeling, Ocean Dynamics. 67 (2017) 1495–1510. https://doi.org/10.1007/s10236-017-1097-5.

[75] J. Colomer, F. Peters, C. Marrasé, Experimental analysis of coagulation of particles under low-shear flow, Water Research. (2005). https://doi.org/10.1016/j.watres.2005.04.076.

[76] S.M. Kresta, P.E. Wood, The flow field produced by a pitched blade turbine: Characterization of the turbulence and estimation of the dissipation rate, Chemical Engineering Science. 48 (1993) 1761–1774. https://doi.org/10.1016/0009-2509(93)80346-R.

[77] K. Lachin, N. Le Sauze, N. Di Miceli Raimondi, J. Aubin, C. Gourdon, M. Cabassud, Aggregation and breakup of acrylic latex particles inside millimetric scale reactors, Chemical Engineering and Processing - Process Intensification. (2017). https://doi.org/10.1016/j.cep.2016.09.021.

[78] D.S. Oliveira, • E C Teixeira, Hydrodynamic characterization and flocculation process in helically coiled tube flocculators: an evaluation through streamlines, International Journal of Environmental Science and Technology. 14 (n.d.). https://doi.org/10.1007/s13762-017-1341-z.

[79] J. Gregory, Flocculation in laminar tube flow, Chemical Engineering Science. (1981). https://doi.org/10.1016/0009-2509(81)80126-1.

[80] K.J. Ives, Experimental Methods (2), The Scientific Basis of Flocculation. (1978) 165–191. https://doi.org/10.1007/978-94-009-9938-1_8.

[81] C.W. Macosko, Rheology Principles, Measurements and Applications, John Wiley & Sons, Ltd, 1994. https://app.knovel.com/web/toc.v/cid:kpRPMA0004/viewerType:toc//root_slug:rheology-principles-measurements (accessed April 26, 2020).

[82] M. Schrimpf, J. Esteban, H. Warmeling, T. Färber, A. Behr, A.J. Vorholt, Taylor-Couette reactor: Principles, design, and applications, AIChE Journal. 67 (2021). https://doi.org/10.1002/aic.17228.

[83] K. Kataoka, Taylor Vortices and Instabilities in Circular Couette flow, Encyclopedia of Fluid Mechanics, Volume 1 “Flow Phenomena and Measurements.” (1986) 236–274. http://ci.nii.ac.jp/naid/10010462590/en/ (accessed April 26, 2020).

[84] L. Wang, D.L. Marchisio, R.D. Vigil, R.O. Fox, CFD simulation of aggregation and breakage processes in laminar Taylor-Couette flow, Journal of Colloid and Interface Science. 282 (2005) 380–396. https://doi.org/10.1016/j.jcis.2004.08.127.

[85] G.I. Taylor, Stability of a Viscous Liquid Contained between Two Rotating Cylinders, 1923. https://about.jstor.org/terms (accessed January 12, 2021).

[86] S. Chandrasekhar, Hydrodynamic and Hydromagnetic Stability, Dover Publications, New York, UNITED STATES, 1981. http://ebookcentral.proquest.com/lib/ualberta/detail.action?docID=1897279.

[87] C. Selomulya, G. Bushell, R. Amal, T.D. Waite, Aggregate properties in relation to aggregation conditions under various applied shear environments, International Journal of Mineral Processing. (2004). https://doi.org/10.1016/j.minpro.2003.09.003.

[88] P. Jarvis, B. Jefferson, S.A. Parsons, Measuring floc structural characteristics, Reviews in Environmental Science and Biotechnology. 4 (2005) 1–18. https://doi.org/10.1007/s11157-005-7092-1.

[89] M. Saadat, Validation of Floc Size Measurements Made with Flow Particle Image Analyzer (FPIA), 10100730 (2014) 239. http://search.proquest.com/docview/1785357129?accountid=178282.

[90] L. Liang, Y. Peng, J. Tan, G. Xie, A review of the modern characterization techniques for flocs in mineral processing, Minerals Engineering. 84 (2015) 130–144. https://doi.org/10.1016/j.mineng.2015.10.011.

[91] G.C. Bushell, Y.D. Yan, D. Woodfield, J. Raper, R. Amal, On techniques for the measurement of the mass fractal dimension of aggregates, Advances in Colloid and Interface Science. 95 (2002) 1–50. https://doi.org/10.1016/S0001-8686(00)00078-6.

[92] R. Xu, O.A. di Guida, Comparison of sizing small particles using different technologies, Powder Technology. 132 (2003) 145–153. https://doi.org/10.1016/S0032-5910(03)00048-2.

[93] L. Ehrl, M. Soos, M. Lattuada, Generation and geometrical analysis of dense clusters with variable fractal dimension, Journal of Physical Chemistry B. 113 (2009) 10587–10599. https://doi.org/10.1021/jp903557m.

[94] C. Lee, T.A. Kramer, Prediction of three-dimensional fractal dimensions using the two-dimensional properties of fractal aggregates, Advances in Colloid and Interface Science. (2004). https://doi.org/10.1016/j.cis.2004.07.001.

[95] L. Guérin, C. Frances, A. Liné, C. Coufort-Saudejaud, Fractal dimensions and morphological characteristics of aggregates formed in different physico-chemical and mechanical flocculation environments, Colloids and Surfaces A: Physicochemical and Engineering Aspects. (2019). https://doi.org/10.1016/j.colsurfa.2018.10.017.

[96] B.E. Logan, J.R. Kilps, Fractal dimensions of aggregates formed in different fluid mechanical environments, Water Research. 29 (1995) 443–453. https://doi.org/10.1016/0043-1354(94)00186-B.

[97] R.C. Sonntag, W.B. Russel, Structure and breakup of flocs subjected to fluid stresses. III. Converging flow, Journal of Colloid And Interface Science. (1987). https://doi.org/10.1016/0021-9797(87)90054-3.

[98] A.S. Moussa, M. Lattuada, B.Ó. Conchúir, A. Zaccone, M. Morbidelli, M. Soos, Flow-induced aggregation and breakup of particle clusters controlled by surface

nanoroughness, Langmuir. 29 (2013) 14386–14395. https://doi.org/10.1021/la403240k.

[99] M. v Majji, J.F. Morris, Inertial migration of particles in Taylor-Couette flows, PHYSICS OF FLUIDS. 30 (2018) 33303. https://doi.org/10.1063/1.5020220.

[100] D.C. Prieve, W.B. Russel, Simplified predictions of Hamaker constants from Lifshitz theory, Journal of Colloid And Interface Science. 125 (1988) 1–13. https://doi.org/10.1016/0021-9797(88)90048-3.

[101] Particle Size Analysis, Introduction to Particle Technology: Second Edition. (2008) 1–28. https://doi.org/10.1002/9780470727102.CH1.

[102] R. Trottier, S. Dhodapkar, A guide to characterizing particle size and shape, Chemical Engineering Progress. 110 (2014) 36–46.

[103] R. Peck, J.L. Devore, Statistics: The Exploration & Analysis of Data, Cengage Learning, 2011. https://books.google.com/books?id=NsAh3P-WrswC&pgis=1.

[104] Horiba, Technical Note 165 UNDERSTANDING AND INTERPRETING PARTICLE SIZE DISTRIBUTION CALCULATIONS, (n.d.). www.horiba.com/particle.

Appendix A - Python script to analyze images

```
"""
Script to analyze particles aggregates
@author: Gustavo Andres Cifuentes D. 2020
"""
import cv2 as cv
import numpy as np
import os
import pandas as pd
from scipy import stats
import matplotlib.pyplot as plt
from skimage.segmentation import clear_border
from skimage import measure
from scipy import ndimage as ndi
from sklearn.linear_model import LinearRegression
import multiprocessing
from joblib import Parallel, delayed

"""
This is the function that extract the information of the images
The function receives the path of the photos and returns the characteristics of the
particles in a dataframe
"""
def imageanalysis(f):

    foto=fol+'/'+f
    img = cv.imread(foto,0)
    # Check if the image has particles
    if (img.max()<30):

        return
    # Noise reduction
    blur = cv.GaussianBlur(img,(5,5),2)
    #Thresholding to binarize image
    ret,th1 = cv.threshold(blur, 30, 255, cv.THRESH_BINARY)
    #Close the image to reduce the rough edges in the particles
    close= cv.morphologyEx(th1, cv.MORPH_CLOSE, kernel1)
    # Fill the holes in the aggregates
    lleno= ndi.binary_fill_holes(close).astype(int)
    # Remove particle touching the border
    border=clear_border(lleno)

    # Extract the particles' information in pixel units and make a table with the
information
    label_img=measure.label(border)
    props                    =                    measure.regionprops_table(label_img,
properties=('bbox','area','equivalent_diameter','perimeter','centroid',))
    dat = pd.DataFrame(props)
    # Add a column with the name of the file
    dat['file'] = f
    # Eliminate noise (particles below 6 pixel)
    dat=dat[dat.equivalent_diameter > 6]
```

```
    # Add a colum with the name focus
    dat['focus'] = False
    dat.reset_index(drop=True, inplace=True)

    # Check if there are particles left the after the image processing
    if dat.size==0:

        return
   # Apply canny edge detector and check if there are edges on the detected particles
    can1 = cv.Canny(blur,100,220)
    for cel in dat.index:
        foc=can1[dat.loc[cel,  'bbox-0']:dat.loc[cel,  'bbox-2'],dat.loc[cel,  'bbox-
1']:dat.loc[cel, 'bbox-3']]
        dat.at[cel,'focus']=np.any(foc==255)
    dat = dat.loc[dat.focus, :]

    # Check if there are particles left
    if dat.size==0:
        return
    # Calculate the radius of gyration
    for cel in dat.index:
        yc=dat.loc[cel, 'centroid-0']
        xc=dat.loc[cel, 'centroid-1']
        rg=0
        for yi in range(dat.loc[cel, 'bbox-0'],dat.loc[cel, 'bbox-2']):
            for xi in range(dat.loc[cel, 'bbox-1'],dat.loc[cel, 'bbox-3']):
                if border[yi,xi]==True:
                    rg=rg+(((xi-xc)**2.0)+((yi-yc)**2.0))

        dat.at[cel,'Rg']=(rg/dat.loc[cel,'area'])**0.5

    dat.reset_index(drop=True, inplace=True)

    return dat

#Calibration 2.25um/pxl
pixel=2.25

# Folder to analyze
D='Folder to analyze'
#Matrix needed in the image analysis
kernel1 = cv.getStructuringElement(cv.MORPH_ELLIPSE,(5,5))
fol = D+'/TIFF'
print(fol)

try:
    os.mkdir(fol+' Results')
except:
    pass

# Parallelize processing
n_jobs = multiprocessing.cpu_count()
retorn_paralel=Parallel(n_jobs=n_jobs)(delayed(imageanalysis)(i)     for     i     in
os.listdir(fol))
```

```
# Concatenate data and save it as csv file
data=pd.concat(retorn_paralel,ignore_index=True, sort=False)
data.to_csv(fol+' Results/data.csv', index=False)

### calculation of the statistical descriptors
diam=pixel*data['equivalent_diameter'].values
rg=pixel*data['Rg'].values
diam=pixel*data['equivalent_diameter'].values
rg=pixel*data['Rg'].values
d32=sum(diam**3)/sum(diam**2)
stdD=np.std(diam)
MeanD=np.mean(diam)
mode= stats.mode(diam)
mode=mode[0][0]
d10=np.percentile(diam, 10)
d50=np.percentile(diam, 50)
d90=np.percentile(diam, 90)
Rg32=sum(rg**3)/sum(rg**2)

#### Fractal Dimension Calculation
Y= np.log(data['area']).values.reshape(-1, 1)
X= np.log(data['perimeter']).values.reshape(-1, 1)
reg = LinearRegression().fit(X,Y)#fit_intercept=False
Y_pred = reg.predict(X)  # make predictions
plt.scatter(X, Y)
plt.plot(X, Y_pred, color='red')
plt.xlabel('log(P)')
plt.ylabel('log(A)')
plt.title('Relation between area and perimeter')
plt.savefig(fol+' Results/01_PerimeterVsArea.png')
plt.grid(True)
plt.show()
#Perimeter fractal dimension
df2=2/reg.coef_[0,0]
# Estimated mass fractal dimension using Ehrl equation
df3=-1.5*df2+4.4

#### Create a Txt File with the results
txt= open(fol+' Results/Test_Results.txt',"w+")
txt.write("################### RESULTS ################### \n" )
txt.write('# particles analized:\t'+str(data.shape[0])+"\n")
txt.write('d32:\t'+str(d32)+"\n")
txt.write('STD d:\t'+str(stdD)+"\n")
txt.write('mean d:\t'+str(MeanD)+"\n")
txt.write('mode d:\t'+str(mode)+"\n")
txt.write('df2:\t'+str(df2)+"\n")
txt.write('df3:\t'+str(df3)+"\n")
txt.write('d10:\t'+str(d10)+"\n")
txt.write('d50:\t'+str(d50)+"\n")
txt.write('d90:\t'+str(d90)+"\n")
txt.write('Rg32:\t'+str(Rg32)+"\n")
txt.close()

print('\n\a')
print('\a')
```

Appendix B - Safe work procedures

Safe work procedure (SWP) Pipeline Transport Processes Research Group

Location: LAB2-156 CME building.

Job title: NaCl Solution Preparation	**Date:** March 15, 2021
Written by: Gustavo A. Cifuentes D	**Conducted by:** Gustavo A. Cifuentes D

Required personal protective equipment (PPE): Lab coat, closed-toe shoes, full-length pants, full coverage safety glasses, nitrile gloves, face mask.
First Aid Measures: **Skin contact** Rinse immediately with plenty of water. If symptoms arise, call a physician. **Eye contact** Rinse immediately with plenty of water, including under the eyelids, for at least 15 minutes. If symptoms persist, call a physician. **Ingestion** Do not induce vomiting without medical advice. **Inhalation** Move to fresh air. If symptoms persist, call a physician. If not breathing, give artificial respiration.

Materials:

- 1000 ml volumetric flask.
- 200 ml volumetric flask.
- 2000 ml beaker.
- Overhead stirrer.
- 3 blades marine impeller.
- Grade 5 Whatman filter paper 0.2 um.
- Glass funnel.
- 50 ml Pycnometer.
- Labels.

Equipment:

- Analytical balance.

- Micropipette.
- pH-meter.

Reagents:

- Dry Sodium Chloride.
- Dry Sodium Hydroxide
- Deionized water

Procedure

Number	Sequence of safe work procedure steps	Potential hazards
1	Covid-19 Measures: • Walk/Bike to the university and back home. • Mark the attendance (entry and leaving time) located on the lab door. • Wash hands with soap and apply sanitizer every time entering and leaving the labs. • Make sure to flush the sink and eyewash upon entering the labs for 3 minutes. • Wear gloves, lab coat, goggles. • Make sure to wipe the instruments, computers, doorknobs, and benches with disinfectant wipes. • If someone else is in the lab, wear a mask and maintain a distance of 2 meters. In the case of leaving momentaneous the lab, use tissue paper to open and close the doors, and use a mask in the hallways/ common areas.	Covid 19 contagion /spread
2	0.1M Sodium Hydroxide Solution Preparation (100ml) • Weigh 0.4 g of NaOH using an analytical balance. • Add the weighted NaOH to a 100ml volumetric flask and add deionized water to fill the 100ml • Mix thoroughly until crystals are fully dissolved. • Label and store using a plastic bottle in the corrosive storage cabinet.	Splash, spills, the use of full PPE is mandatory, in the case of contact with Sodium Hydroxide area needs to be rinsed for 15 minutes,
3	1.4M Sodium Chloride Brine Preparation (1000ml) • Weigh 82 g of NaCl using an analytical balance. • Add the weighted NaCl to a 1000ml volumetric flask and add 500 ml of deionized water.	Splash, spills, the use of full PPE is mandatory, in the case of contact with Sodium Hydroxide

Number	Sequence of safe work procedure steps	Potential hazards
	• Mix thoroughly until sodium chloride crystals are fully dissolved. • Fill the volumetric flask the mark to reach 1000ml • Transfer the solution to a 2000 ml beaker. • Attach a 3-blade marine propeller impeller with a 3cm diameter to the IKA RW 20 digital overhead stirrer. • Place the beaker with the overhead stirrer and ensure to place the impeller 5cm above the bottom of the beaker. • Stop the overhead stirrer and measure pH using the pH meter. • Adjust the solution pH to 7.0 using 0.1M NaOH and one drop of the NaOH. • Start the overhead stirrer to mix the NaOH for 1 minute, then stop the overhead stirrer and measure the pH • Repeat the process of addition of drops of NaOH until reach pH 7.0 • Filter the brine using a funnel and a 0.2um filter paper. • Check the density, using a pycnometer which must be 1.055kg/m3 $\rho_{Brine} = \rho_{water} * weight_{brine}/weight_{water}$ • If the brine density is lower than required (particles will float), add the calculated amount of NaCl and repeat steps from the beginning. If the brine density is higher than required, (particles will settle) add the calculated amount of water and repeat steps from the beginning.	affected area needs to be rinsed for 15 minutes
4	Cleaning • Organize the work area. • Wipe the surfaces with disinfectant wipes. • Wash all equipment and hang on a drying rack • Ensure all waste is properly labelled and placed in the appropriate waste disposal area • Make sure to mark the leaving time in the attendance sheet. Wash the hands using soap and apply sanitizer before leaving any lab.	

Number	Sequence of safe work procedure steps	Potential hazards
5	Contact Terry Runyon 780-248-1554 or trunyon@ualberta.ca to inform her of the waste that needs to be disposed of.	

Safe work procedure (SWP) Pipeline Transport Processes Research Group

Location: LAB2-156 CME building.

Job title: Latex Particles Aggregation and breakage	**Date:** August 25, 2020
Written by: Gustavo A. Cifuentes D	**Conducted by**: Gustavo A. Cifuentes D

Required personal protective equipment (PPE): Lab coat, closed-toe shoes, full-length pants, full coverage safety glasses, nitrile gloves, face mask.
First Aid Measures: **Skin contact** Rinse immediately with plenty of water. If symptoms arise, call a physician. **Eye contact** Rinse immediately with plenty of water, including under the eyelids, for at least 15 minutes. If symptoms persist, call a physician. **Ingestion** Do not induce vomiting without medical advice. **Inhalation** Move to fresh air. If symptoms persist, call a physician. If not breathing, give artificial respiration.

Materials:

- 100 ml volumetric flask.
- 200 ml volumetric flask.
- Filter paper 0.2 um.
- Glass funnel.
- 10 ml Pycnometer.

Equipment:

- Analytical balance.
- Micropipette.
- pH-meter.
- Lab 2-156 Couette Cell

Reagents:

- Sodium Chloride.
- 2um latex beads.
- Sodium Hydroxide

Procedure

Number	Sequence of safe work procedure steps	Potential hazards
1	Covid-19 Measures: • Walk/Bike to the university and back home. • Mark the attendance (entry and leaving time) located on the lab door. • Wash hands with soap and apply sanitizer every time entering and leaving the labs. • Make sure to flush the sink and eyewash upon entering the labs for 3 minutes. • Wear gloves, lab coat, goggles. • Make sure to wipe the instruments, computers, doorknobs, and benches with disinfectant wipes. • If someone else is there in the lab, wear a mask and maintain a distance of 2 meters. • In the case of leaving momentaneous the lab, use tissue paper to open and close the doors, and use a mask in the hallways/ common areas.	Covid-19 contagion /spread
2	Suspension • Measure 50 ml of sodium chloride solution using a 50ml graduate cylinder and place the solution in the Couette cell chamber (outer cylinder). • Measure 66 µl of sulphate latex beads using a 100ul micropipette and add the latex solution drop b drop to the Couette cell chamber. • Gently mix the solution until obtaining a turbid homogeneous mixture.	Splash, spills, the use of full PPE is mandatory
3	Couette cell setup • Attach the outer cylinder with the initial suspension to the Couette cell structure, tighten the screws until the Couette cell is sealed. • Mix the suspension at 2000RPM (overhead stirrer) for 5min.	Splash, spills, use of inappropriate tools, the use of full PPE is mandatory,
4	Aggregation and Breakage • Change the rotational speed of the overhead stirrer to 30RPM (shear rate of 17.6 s^{-1}).	Splash, spills, use of inappropriate tools, the use of full PPE is mandatory

Number	Sequence of safe work procedure steps	Potential hazards
	• Place the camera in front of the Couette cell, use the translation stage to adjust the distance until the aggregates are in focus. • After 2.5h of shearing at 17.6 s^{-1} measure the aggregate size distribution taking 2000 pictures at 10 fps and save the pictures on PC. • Run the image analysis script to obtain the aggregate size distribution. • Quantify the aggregate size distribution every 15 minutes, until the aggregate size distribution is constant. • Once the aggregate has reached a constant size distribution, the aggregates are in a steady state, • Increase the shear rate to observe the breakage of the aggregates according to table B1. • Measure the aggregate size distribution immediately and as often as possible (times will vary depending on the time required to save and to analyze the images) until the aggregate size distribution is constant. • Stop the Couette Cell overhead stirrer and turn off.	
5	Disassembly and cleaning • Remove the screws from the Couette cell and uncouple the outer cylinder. • Dispose of the suspension in a labelled container. • Wash the outer and inner cylinder with soap and water. Using a microfiber cloth to avoid scratches on the outer transparent cylinder • Rinse the Couette cell with tap water followed by deionized water. • Dry the Couette cell.	Splash, spills, the use of full PPE is mandatory
6	Cleaning • Clean the work area. • Wipe the surfaces with disinfectant wipes. • Wash all equipment and hang it on a drying rack • Ensure all waste is properly labelled and placed in the appropriate waste disposal area • Make sure to mark the leaving time in the attendance sheet.	

Number	Sequence of safe work procedure steps	Potential hazards
	• Wash the hands using soap and apply sanitizer before leaving any lab.	
	Contact Terry Runyon 780-248- 1554 or trunyon@ualberta.ca to inform her of the waste that needs to be disposed of.	

Table B1 Rotational velocities in the aggregation and breakage experiments

Experiment	Breakage		
	Overhead Stirrer (RPM)	Inner Cylinder (RPM)	Shear Rate(s^{-1})
1	50	11.0	28.9
2	60	13.3	34.7
3	100	22.1	57.9
4	130	28.8	75.3
5	150	33.2	86.8

Appendix C - Describing population of particles

When particles are present in a population there are different sizes. The different particle sizes are represented using a particle size distribution, which can be a frequency distribution or a cumulative distribution. The size data are sorted into intervals or bins covering the entire size range of the population. Then, the proportion (number fraction or percentage) of particles in each bin is calculated and plotted, this is called a number frequency distribution. The cumulative distribution (denoted as F) shows for each bin the proportion of particles with a size lower and equal than the bin mean value. Differential frequency dF/dx can be obtained by dividing the frequency data by the bin width. Using a differential frequency distribution becomes particularly important when comparing particles that are classified in different bins or size ranges, or when comparing data collected using different measurement techniques [101].

Often, it is necessary to describe a population of particles using a single number. In this thesis the arithmetic mean and the Sauter mean diameter are used to describe the particle population. The arithmetic mean is the sum of all the diameters in the population divided by the total number of particles [102]:

$$d_{1,0} = \frac{\sum n_i d_i}{\sum n_i}.$$

where n_i is the number of particles in bin i and d_i is the midpoint diameter of bin i. The Sauter mean diameter is defined as the diameter of a sphere that has the same surface to volume ratio as the entire population, it can be calculated as [102]:

$$d_{3,2} = \frac{\sum n_i d_i^3}{\sum n_i d_i^2}.$$

A sample calculation of the differential frequency distribution and the calculation of the Sauter mean diameter is presented in Table C1.

The spread of the size distribution can be represented by its standard deviation which is the measure of the amount of variation in a sample of particles, it is calculated as [103]:

$$\sigma = \sqrt{\frac{\sum (d - d_{1,0})^2}{n - 1}}$$

Where *n* is the total number of particles in the sample. The spread of the particle size distribution is also expressed with the values of *d10*, *d50*, and *d90* [104].

- *d50* is the median, which is the diameter in which half of the population lies below this value.
- *d90* is the value in which 90% of the population lies below this value.
- *d10* is the value in which 10% of the population lies below this value.

Table C1 Calculation example of the number based differential frequency distribution, arithmetic and Sauter mean diameter

Diameter (µm)			Bin size, dx	Particle count, ni	Number fraction	F	dF/dx	ni*di	ni*(di)^2	ni*(di)^3
Min	Max	Midpoint, di								
10.0	12.6	11.3	2.6	0	0	0	0	0	0	0
12.6	15.8	14.2	3.3	0	0	0	0	0	0	0
15.8	20.0	17.9	4.1	0	0	0	0	0	0	0
20.0	25.1	22.5	5.2	0	0	0	0	0	0	0
25.1	31.6	28.4	6.5	0	0	0	0	0	0	0
31.6	39.8	35.7	8.2	2	0.0002	0.0002	2.39E-05	7.14E+01	2.55E+03	9.11E+04
39.8	50.1	45.0	10.3	6	0.0006	0.0008	5.70E-05	2.70E+02	1.21E+04	5.45E+05
50.1	63.1	56.6	13.0	4	0.0004	0.0012	3.02E-05	2.26E+02	1.28E+04	7.26E+05
63.1	79.4	71.3	16.3	9	0.0009	0.0021	5.40E-05	6.41E+02	4.57E+04	3.26E+06
79.4	100.0	89.7	20.6	33	0.0032	0.0053	1.57E-04	2.96E+03	2.66E+05	2.38E+07
100.0	125.9	112.9	25.9	84	0.0082	0.0135	3.18E-04	9.49E+03	1.07E+06	1.21E+08
125.9	158.5	142.2	32.6	147	0.0144	0.0279	4.42E-04	2.09E+04	2.97E+06	4.23E+08
158.5	199.5	179.0	41.0	1098	0.1076	0.1355	2.62E-03	1.97E+05	3.52E+07	6.30E+09
199.5	251.2	225.4	51.7	4239	0.4153	0.5507	8.04E-03	9.55E+05	2.15E+08	4.85E+10
251.2	316.2	283.7	65.0	3568	0.3495	0.9003	5.37E-03	1.01E+06	2.87E+08	8.15E+10
316.2	398.1	357.2	81.9	967	0.0947	0.9950	1.16E-03	3.45E+05	1.23E+08	4.41E+10
398.1	501.2	449.6	103.1	51	0.0050	1	4.85E-05	2.29E+04	1.03E+07	4.64E+09
501.2	631.0	566.1	129.8	0	0	1	0	0	0	0
631.0	794.3	712.6	163.4	0	0	1	0	0	0	0
794.3	1000.0	897.2	205.7	0	0	1	0	0	0	0
			Sum	10208			Sum	2566985	6.76E+08	1.86E+11

$d_{1,0} = 251.5$

$d_{3,2} = 274.6$

Appendix D - Microphotographs of validation particles

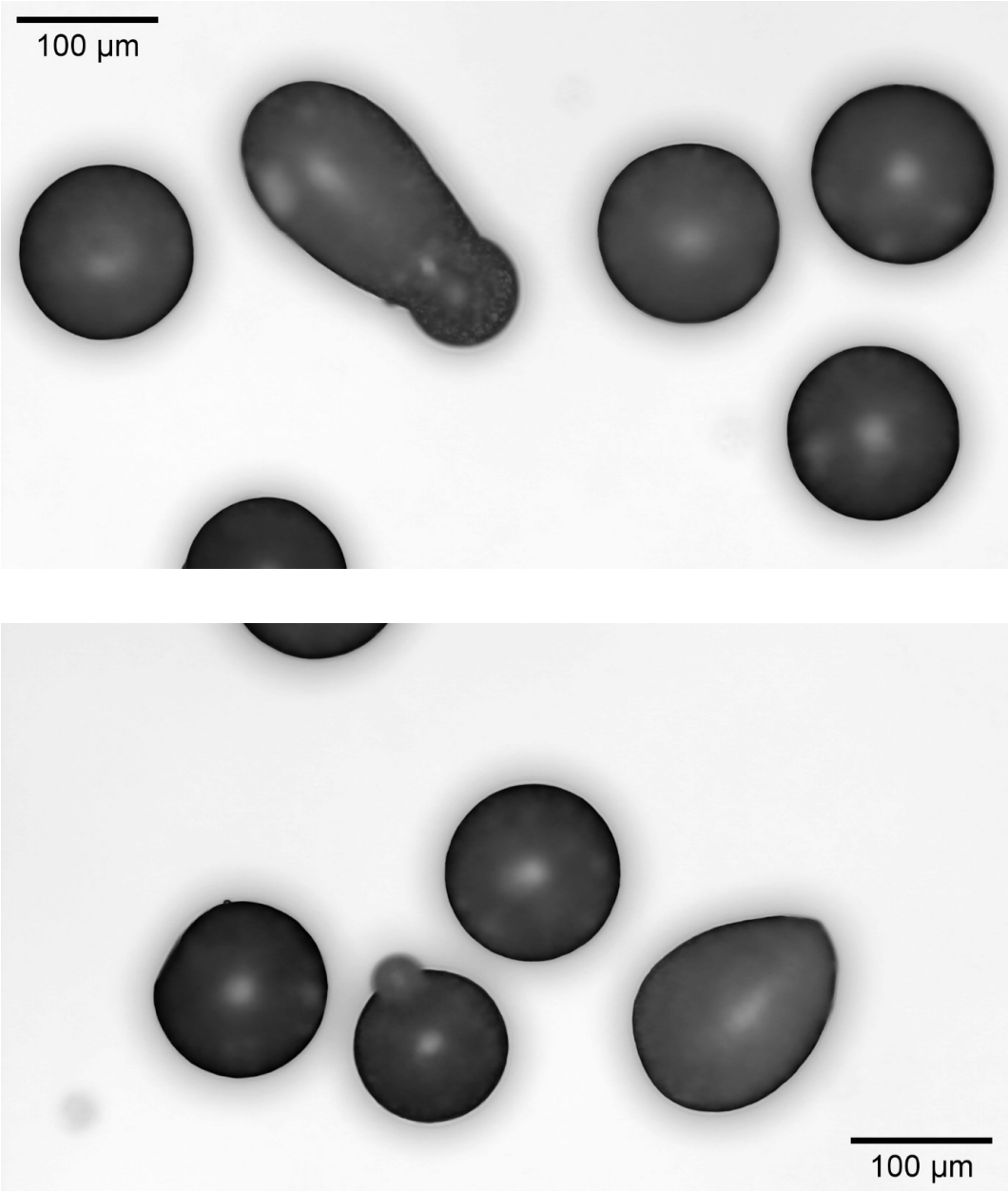

Figure D1 Microphotographs of the particles "WPMS 106-125um" at 10X.

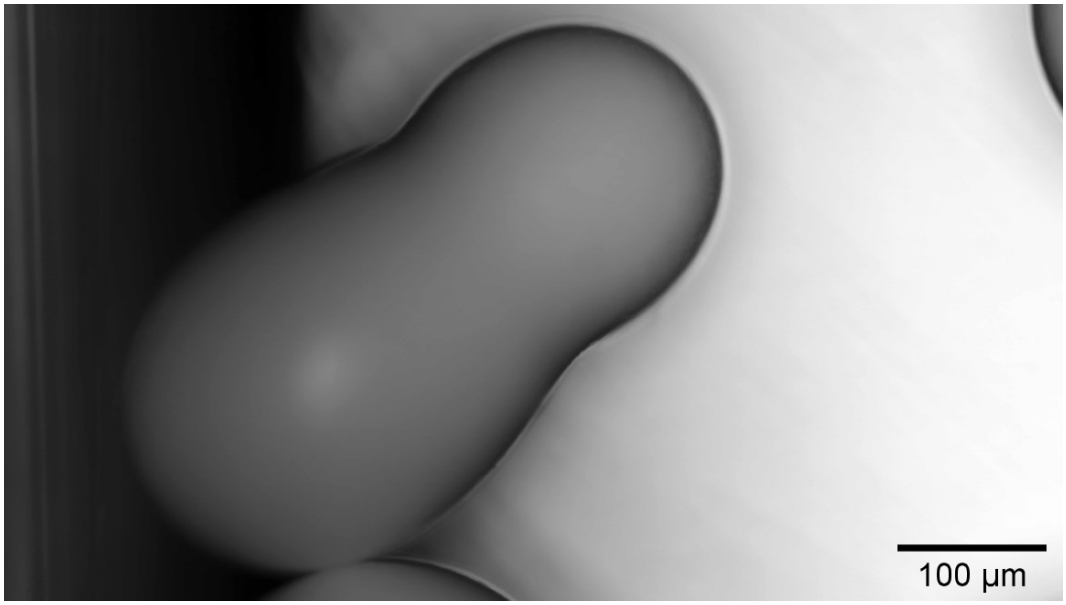

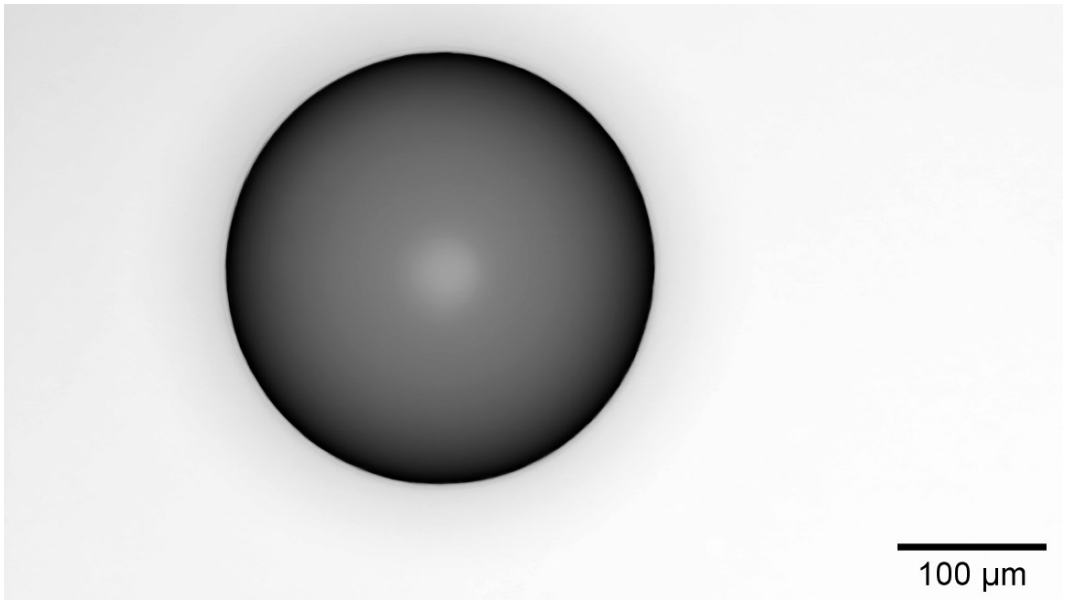

Figure D2 Microphotographs of the particles "WPMS-250-300um" at 10X.